THERMAL PROPERTIES OF DISORDERED ORGANIC SOLIDS AND INTERFACES INVOLVING ORGANICS

by

Yansha Jin

A dissertation submitted in partial fulfillment
of the requirements for the degree of
Doctor of Philosophy
(Materials Science and Engineering)
in The University of Michigan
2013

Doctoral Committee:

Associate Professor Max Shtein, Co-Chair
Associate Professor Kevin P. Pipe, Co-Chair
Professor Jay L. Guo
Associate Professor Anton Van der Ven

ACKNOWLEDGEMENTS

First and foremost, I would like to express my profound gratitude to my committee members: to the Chairs, Professor Max Shtein and Professor Kevin P. Pipe for their support through my doctoral study and their wise guidance in research and invaluable suggestions in life; to Professor Anton van der Ven and Professor L. Jay Guo, who has for many years helped and encouraged me, their advice has helped substantially to my study. Especially, I am deeply grateful to Professor Max Shtein. He has been a role model in creativity thinking, work ethics and family values, and his encouragements and suggestions during some frustrating periods in these five years were eminently helpful to me. I am also very thankful to Professor Pramod Reddy and Professor John Kieffer for their valuable input to my research.

I am pleased to acknowledge the financial support from United States Air Force Office of Scientific Research under Grant No. FA9550-080-1-0340 throughout the Multidisciplinary University Research Initiative Program. The gratitude also extended to Rackham graduate school - Barbour scholarship program and University of Michigan, Materials Sciences and Engineering department.

I owe a great deal to many fellow students in my research lab and other labs I have worked and collaborated at various stages of my doctoral study: Kanika Agrawal, Kwang Hyup An, Adam Barito, Andrea Bianchini, Shaurjo Biswas, Victor Chan, Susan Gentry, Chelsea Haughn, Mark Hendryx, Lei Jiang, Jongdoo Ju, Myungkoo Kang, Gunho Kim, Jingjing Li, Steven Morris, Denis Northern, Olga Shalev, Chen Shao, Huarui Sun, Matt Sykes, Abhishek Yadav, Kejia Zhang, Yiying Zhao and many

others. I would like to offer my sincere thanks to Abhishek Yadav for unselfishly teaching and helping me in the starting stage of my project with endless patience, also for buying me my first beer in Ann Arbor; To Yiying Zhao for being my best friend in the lab and I am constantly amazed by her personality and her wisdom in life; To my lovely peers Steven Morris and Shaurjo Biswas who has always been there for me, it has been a real pleasure to have my the most pessimistic and most optimistic friends' accompany.

My heartfelt appreciation also goes out to all my friends. Especially, to my dearest Emmy Lei who has been my best friend for 8 years, from the Beijing days to the Ann Arbor era; To Yilu Wang for sharing the unexpected challenges in life with me; To Diana Sykes for being the best hostess and making my life in Ann Arbor more colorful.

Special gratitude to Deborah Des Jardins. Without her help, this thesis would have contain thousands more grammar mistakes and even more unfriendly to the readers. Moreover, she has not only helped me in academic English writing, but also offered guidances in many other aspects in my life. Her intelligence and integrity have always been an inspiration.

I am enormously grateful to have my parents Ming Jin and Jun Wang supporting me throughout my life, words are not enough to express my love and gratefulness. Finally, this thesis is dedicated to my husband, Weiran Li.

TABLE OF CONTENTS

LIST OF FIGURES

Figure

LIST OF TABLES

Table

LIST OF APPENDICES

Appendix

LIST OF ABBREVIATIONS

TBC Thermal Boundary Conductance

CuPc Copper Phthalocyanine

Ag Silver

DOS Density of States

OLED Organic Light Emitting Diodes

NPD N,N'-di-1-naphthyl-N, N'- diphenyl-1, 1'-biphenyl-4, 4'diamine

Alq_3 aluminum hydroxiquinoline

AFM Atomic Force Microscopy

F.C.C. Face-Centered Cubic

TE Thermoelectric

ZT Figure of Merit

TDTR Time-Domain Thermo-Reflectance

TEM Transmission Electron Microscopy

RMS Root Mean Square

SEM Scanning Electron Microscopy

RT Room Temperature

CT Cryogenic Temperature

MDS Molecular Dynamics Simulations

LDS Lattice Dynamics Simulations

XRD X-ray Diffraction

FEM Finite Element Modeling

PEDOT:PSS poly(3,4-ethylenedioxythiophene) poly(styrenesulfonate)

DMM Diffuse Mismatch Model

BOE Buffered Oxide Etch

SEM Scanning Electron Microscopy

ITO Indium Tin Oxide

XPS X-ray Photoelectron Spectroscopy

SAM Self-Assembled Monolayers

SubPc chloro-subphtalocyaninato boron(III)

ABSTRACT

Thermal Properties of Disordered Organic Solids and Interfaces involving Organics

by

Yansha Jin

Co-Chair: Professor Max Shtein and Professor Kevin P. Pipe

Research interest in energy conversion in organic materials has been growing steadily, driven in part by the potential advantages of light weight, mechanical flexibility, scalability and low-cost manufacturing capability. Among the unique properties of these materials is the strong coupling between charge carriers and phonons. Under this strong coupling, the organic molecules deform and rearrange in the presence of the charge carrier; the resulting carrier accompanied by local polarization of the solid is termed "Polaron". The detailed physics of the polaronic behavior in organic materials is still relatively poorly understood, particularly at the interfaces between the organic semiconductor and the inorganic phase in energy conversion devices. Thus, there remain vast possibilities for future leaps in the development of new materials and device architectures.

This thesis is aimed to generate some of this needed knowledge, focusing on phonon dynamics and heat transport in van der Waals bonded organic thin films, especially at organic-inorganic interfaces.

Thermal Boundary Conductance (TBC) values are reported here for interfaces between several metals and small molecule organic semiconductors. Both experimen-

tal and simulation results suggest that for interfaces with large acoustic mismatch, the TBC is closely correlated to the bonding strength at the interface. Interfacial bonding between Copper Phthalocyanine (CuPc) and Silver (Ag) is van der Waals in nature, and the TBC value at this interface is 1$\sim$2 orders of magnitude lower than that of metal-inorganic dielectric interfaces. Therefore, the boundary effects cannot be neglected in the systematic thermal analysis of nanostructured organic optoelectronic/thermoelectric devices, and must be elucidated during material selection and design for these applications. One exceptional example demonstrated through simulations in this thesis is the 10-fold increase of thermoelectric figure of merit in organic-metal nanocomposites due to low values of TBC in the hybrid systems under consideration. The fundamentals of this low-conductance phenomenon are discussed in detail in this dissertation, with simulation results suggesting that it is the anharmonic nature of phonon transmission at weakly bonded interfaces, as well as a unique spatially non-uniform interfacial vibration at some (e.g. CuPc-Al) interfaces that can be at the root of the observed thermal transport behavior.

CHAPTER I

Introduction

The organic semiconductor industry has grown at a tremendous rate since the discovery of highly conductive organic materials in 1977. In the past decade, organic semiconductors have become a functional class of materials in the electronics industry because of their promising properties such as low cost, light weight, scalability and flexibility. The science discussed in this thesis is aimed at elucidating the thermal properties of organic semiconductors and organic semiconductor/inorganic interfaces. No study has adequately explored these properties to date.

This chapter aims to demonstrate the importance of exploring the thermal properties of the organic semiconductors. Starting with the physics of charge transport in organics, **Section 1.1** focuses on the temperature dependence and its relation to the phonon transport. **Section 1.2** discusses the thermal issues on a macroscopic scale: the overheating in nanodevices and the thermal management at device and packaging levels. **Section 1.3** introduces the Thermoelectric (TE) devices, and covers the basic principles and efficiency calculation of the general TE devices along with the recent advances in the organic based ones. The last section (**Section 1.4**) gives an overview and the organization of this thesis.

1.1 Transport Properties of Disordered Organics

Let us start with a recap of the history of transport theories (*Ashcroft and Mermin* (1976), *Fox* (2001), *Huang* (1997)). Drude was the first to come up with a widely accepted theory of the transport properties of metals. This theory, also referred to as the Drude model, applied the kinetic theory of gases to transport of charge in metals. In the Drude model of electrical conductivity, electrons are supposed to move in a straight line until they collide with the ions. Following this idea, conductivity is written as

$$\sigma_e = n_e e \mu_e = \frac{n_e e^2 \tau_e}{m_e} \tag{1.1}$$

where n_e is the electron density, μ_e is the electron mobility, m_e is the electron mass, e is the unit charge and τ_e is the relaxation time that represents the average time before an electron hits an ion. τ_e can be estimated as $\tau_e = l_e/v_e$. However, Drude assumed the velocity of an electron v_e from the classical equipartition of energy $\frac{1}{2}mv_e^2 = \frac{3}{2}k_BT$ and the electron mean free path l_e as the ions' separation – these two assumptions cause a cancellation of errors that result in a model that fits observations for many metals.

The discovery of quantum mechanics led to the realization that v_e in Drude's classical estimation was an order of magnitude smaller than the real Fermi velocity of electron v_F. At the same time, the electrons are not bumping off the ions which makes the mean free path l_e one order of magnitude larger. Two wrongs did make a right for Drude. Though people like me sometimes mentioned Drude in this mocking tone to make the story more dramatic, his significant contribution cannot be overstated. It turns out **Eq 1.1** is the most frequent used equation throughout my research because of its accurate depiction of the physical picture under semiclassical approximation: The electrons do hit something, though not the ions; they "hit" the defects and impurities, and they "hit" the phonons. Scientifically speaking, this "hit" is referred

to as scattering and this scattering concept can be generalized to all kinds of transport mechanisms.

Another leap in the transport theory was the development of band theory. Band theory is based on the periodic potential produced by the crystal lattice. This periodic potential is the keystone for the modern solid state physics. One approach towards the band theory is to assume the variation of the periodic potential is small enough that can be treated as a perturbation. This perturbation only affects the degenerate states at the edge of the Brillouin zone. The degeneracy is broken as a result of the perturbation and the energy level splits to form an energy gap, which is usually referred to as the "bandgap." Metals, semiconductors and insulators can be distinguished by the width of the bandgap and the fillings of the energy levels.

A direct consequence of the band model and, for semiconductors, the most important concept in understanding charge transport is the effective mass. The electrons are no longer free as they are in metals; the periodic lattice potential has a bigger impact on the electrons in semiconductors. The effective mass is written as,

$$m^* = \hbar(\frac{d^2E}{dk^2})^{-1} \tag{1.2}$$

The above equation shows that the value of the effective mass is proportional to the inverse to the curvature the energy dispersion. Many interactions, such as electron-electron, electron-phonon, have to be considered in the calculation of this curvature. m^* directly correlates with the μ_e mobility, as shown in **Eq 1.1**.

Here, the result of $\vec{k} \cdot \vec{p}$ theorem on effective mass is presented. The theory purely considers the periodic potential and treats each electron separately. While **Eq 1.2** still holds, using the degenerate perturbation theory yields,

$$\frac{1}{m^*} = \frac{1}{m} + \frac{2}{mk^2} \sum_{l \neq n} \frac{\langle u_{n0}|\vec{k} \cdot \vec{p}|u_{l0}\rangle}{E_{n0} - E_{l0}} \tag{1.3}$$

Eq 1.3 indicates a well-known conclusion, the larger the bandgap, $(E_{n0} - E_{l0})$, the larger the effective mass and less mobile the charge carriers are.

The scattering and the effective mass concepts can both be generalized to the transport of organic semiconductors. However, more in-depth discussion of band theory does not apply to disordered organic materials because of some special characteristics of the organics charge transport:

1. The existence of the tightly bonded electron-hole pairs;

2. Disordered structure which yields no periodic potential.

The electron-hole pair is called **exciton**; The disordered structure results in charge transport assisted by the **phonons**; Electron-phonon interaction produces another type of quasi-particles, **polarons**, which all leads to the complications of transport theory of organics. The transport mechanisms of the three quasi-particles above are discussed separately in the following subsections.

1.1.1 Excitons

Electron-hole pair generation is an important process in semiconductor devices. An electron and a hole bounded by the Coulomb attraction is called an exciton. The energy of the bonding categorizes the excitons. **Figure 1.1** shows a free exciton with a large radius (Wannier-Mott excitons) and a tightly-bonded one with a small radius (Frenkel excitons). Take a typical inorganic semiconductor, GaAs as an example (*Fox* (2001)), the largest exciton binding energy is 4.2 meV, which equals to the thermal energy, k_BT, at 49 K. Therefore, these Wannier-Mott excitons in GaAs can only be observed at cryogenic temperature. For organic semiconductors, on the other hand, the molecules/polymers are held together by weak van der Waals forces. As a result, the excitons in these materials are highly localized and coupled strongly with the phonons.

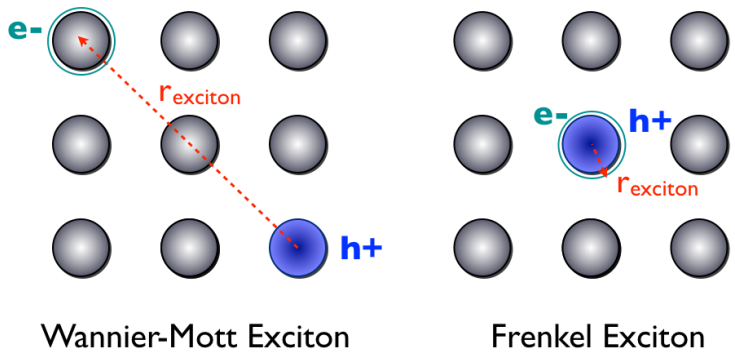

Figure 1.1: Wannier-Mott exciton (Left) is referred to as free exciton with large radius; the electrons and holes are weakly bonded in Wannier-Mott exciton; Frenkel exciton (Right) is referred to as tight-bonded exciton, these excitons are much less mobile than Wannier-Mott excitons. (Figure by Yansha Jin)

To better understand the above statement, one can use a dimer system of a two-level molecule as an example. The detailed mathematical derivation is shown in **Appendix A**, which is adapted from *Agranovich and Bassani* (2003).

The resulting energy diagram for the dimer system, shown in **Figure 1.2**, indicates the degenerated states split into two with the separation of $2|J_{12}|$. Thus, the smaller the intermolecular overlap $|J_{12}|$, the smaller the energy level separation.

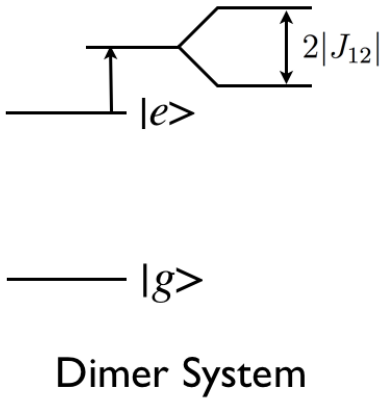

Figure 1.2: A 2-level molecule is presented as a ground state, $|g\rangle$ and an excited states, $|e\rangle$. For a dimer system of this molecule, the interaction between the two atoms split the excited states by the width of $2|J_{12}|$ (Figure by Yansha Jin)

N-molecule system can be generalized from the above dimer case: N degenerated states split into N levels, where the span of these N energy levels is the band width. Similarly, the width of the band will be narrow if the intermolecular overlap is small.

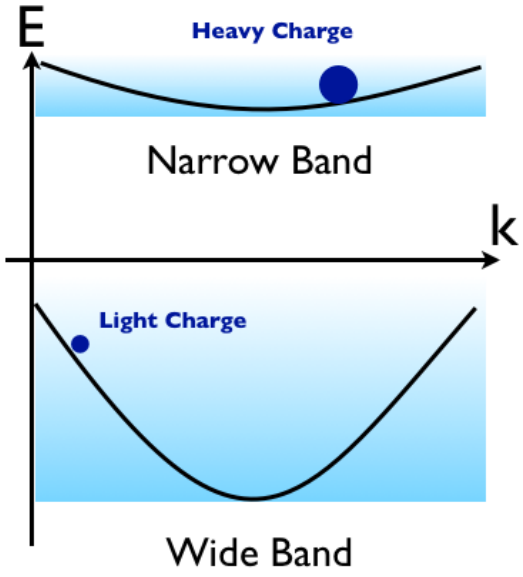

Figure 1.3: Effective mass theory suggests that if the band width is narrow (upper image), the curvature of the band diagram is very small, indicating a large effective mass; vice versa. (Figure by Yansha Jin)

Under the assumption of a narrow band, the curvature of the energy diagram should be very small, resulting in a huge effective mass m^* (**Eq 1.2**). By applying the Bohr model to the excitons, the exciton radius (quantum number $n = 1$) yields,

$$r_{\text{exciton}} = \frac{m_e}{m^*} \cdot \epsilon_r a_{\text{H}} \tag{1.4}$$

where ϵ_r is the dielectric constant and a_{H} is the Bohr radius for Hydrogen atom. **Eq 1.4** shows that large m^* leads to small exciton radius.

In organics, the interactions among molecules are weak - in another words, the intermolecular overlap is small. As a result, the band is narrow, m^* is large and the exciton radius calculated by **Eq 1.4** is often less than the size of the molecule,

indicating the excitons in organics are tightly-bonded. This conclusion can also be derived from an equivalent tight-bonding model, details can be find in *Baldo* (2001).

The narrow band and the large effective mass also lead to many other crucial facts: the large exciton-phonon coupling strength and the lack of coherent transport under room temperature. These effects will be discussed in **Subsection 1.1.3** with more details.

1.1.2 Phonons

This subsection presents the basics of phonons. The concepts introduced here will be encountered later in the thesis (**Ch. II** and **Ch. III**); Many theoretical models on the thermal transport are based on the fundamental ideas presented here, such as Lattice Dynamics Simulations (LDS) and Scatter Boundary model in **Ch. V**.

Phonons are defined as the quantizations of vibrations modes of interacting particles. Both *Huang* (1997) and *Ashcroft and Mermin* (1976) have comprehensive chapters on the phonon theory. Both of these book chapters begin with solving normal vibrational modes of 1D monatomic lattice, assuming nearest-neighbor interactions and a harmonic interacting potential written as

$$V_{\text{1D-M}} = \frac{1}{2} K_{\text{sp}} \sum_{n} (u_n - u_{n+1})^2 \tag{1.5}$$

where K_{sp} is the spring constant between the nearest neighbors and u_i is the displacement of i-th atom in the 1-D chain. The dispersion relation of frequency ω versus wave vector k is shown in **Figure 1.4 (a)**. If the 1D lattice is not monatomic but diatomic, another curve appears in dispersion in addition (shown in **Figure 1.4 (b)**): the lower branch, which is similar to the monatomic, is the acoustic branch; the upper branch is called the optical branch. Generalizing to 3-D cases: for 3D monoatomic lattice, there are no optical branches but 3 acoustic branches; for 3D lat-

tice with p atoms on each site, the dispersion should contain 3 acoustic and $3(p-1)$ optical branches. Here, I perform a simplified calculation of dispersion relation of

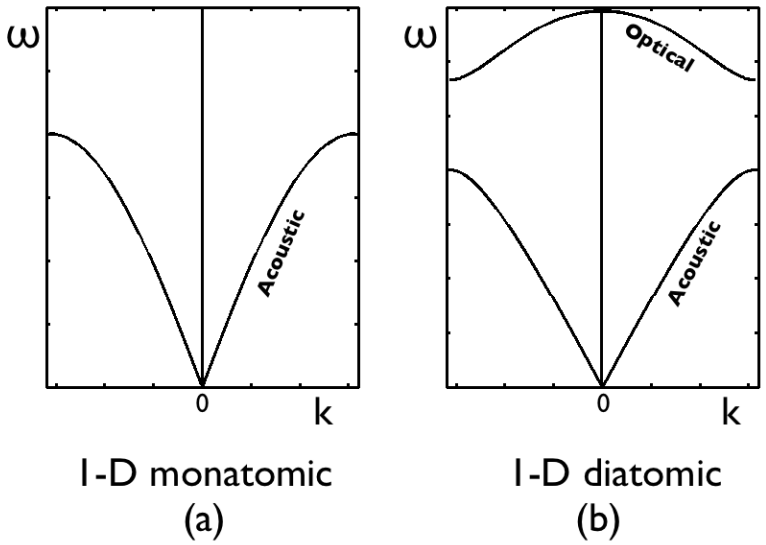

Figure 1.4: Dispersion relation of monatomic (left) and diatomic (right) 1-D chain. Dispersion of monatomic 1-D chain has a single acoustic branch, while that of the diatomic chain has one acoustic and one optical branch. (Figure by Yansha Jin)

Face-Centered Cubic (F.C.C.) monoatomic lattice. Based on this example many important concepts will be introduced, e.g. Density of States (DOS), sound velocity, thermal conductivity.

The assumptions made for F.C.C monoatomic lattice are similar to 1D, only nearest neighbors are considered. Instead of **Eq 1.5**, the interacting potential is written as,

$$V_{3\,\mathrm{D,M}} = \frac{1}{2}\sum_{i,j} \vec{u}_i \mathbf{D}(\vec{R}_i - \vec{R}_j)\vec{u}_j \tag{1.6}$$

where $\vec{R}_i$ is the Bravais lattice position for atom i and $\mathbf{D}$ is the interaction matrix.

To solve the equation of motion is to find the eigenvalues for $\mathbf{D}$,

$$\omega^2 = \mathrm{eig}(\mathbf{D}(\vec{k}))\ \text{, where}\ \mathbf{D}(\vec{k}) = -2\sum_i \mathbf{D}(\vec{R}_i)\sin(\frac{1}{2}\vec{k}\cdot\vec{R}_i) \tag{1.7}$$

The summation is over the nearest neighbors in F.C.C. Because the six nearest neighbors are equivalent, $\mathbf{D}(\vec{R}_i)$ can be simplified as $\mathbf{D}(\vec{R}_i) = \mathbf{I} \cdot K_{\text{sp}}$. The dispersion curves along [100] and [110] are shown in **Figure 1.5**. No optical branches are observed, which is expected for monoatomic lattice. Important concepts can be introduced starting with these dispersion curves.

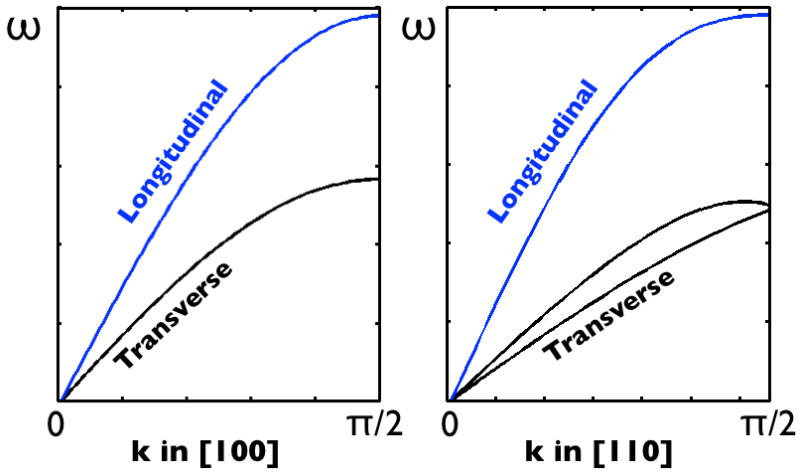

Figure 1.5: Dispersion relations of monoatomic F.C.C. lattice along [100]-left and [110]-right direction. A F.C.C. monoatomic lattice has 3 acoustic branches: two transverse and one longitudinal. The acoustic branches can be degenerate due to symmetry of the lattice, e.g. [100] direction of F.C.C. (Figure by Yansha Jin)

Longitudinal and transverse acoustic waves: Along direction [110], there are three curves corresponding to one longitudinal waves and two transverse waves; Along direction [100], the two transverse waves are degenerated due to the symmetry of the lattice.

Sound velocity: When $\vec{k}$ is small, the wavelength is much larger than the lattice constant and the solid can be seen as continuous. In this regime, the dispersion relation is linear. The slope of this line by definition is the velocity of the vibrational wave, often referred to as the sound velocity, v_{s}. In 1D monoatomic case, the sound velocity is calculated to be,

$$v_{\text{s}} = d_0 \sqrt{\frac{K_{\text{sp}}}{m_a}} \tag{1.8}$$

where d_0 is the lattice constant, m_a is the mass of the atom. **Eq 1.8** leads to the general sound velocity formula.

$$v_{\mathrm{s}} = \sqrt{\frac{E_{\mathrm{BM}}}{\rho}} \tag{1.9}$$

where E_{BM} is the bulk modulus of the material and ρ is the material's density. The sound velocity is directly related to the materials' thermal conductivity,

$$k_{\mathrm{th}} = \frac{1}{3} C_v \tau_p v_{\mathrm{s}}^2 \tag{1.10}$$

where C_v is the volume heat capacity, and τ_p is the phonon relaxation time. This relaxation time is affected by several phonon-scattering mechanism, including phonon-impurity scattering, phonon-electron scattering, phonon-boundary scattering and phonon-phonon scattering. τ_p follows the Matthiessen's rule, $1/\tau_p = \sum_i 1/\tau_i$, where τ_i is the relaxation time of each scattering mechanism.

The above expression, (**Eq 1.10**) is for the phonon's contribution in thermal transport, the total k_{th} is also affected by the charge transport,

$$k_{\mathrm{th}} = k_{\mathrm{th,e}} + k_{\mathrm{th,p}} \tag{1.11}$$

where $k_{\mathrm{th,e}}$ is the charge contribution to the thermal transport which will be discussed in **Section 1.3**.

Density of States (DOS): Under the assumption that the dispersion is linear $\omega_{\mathrm{p}} = v_{\mathrm{s}} k$, where ω_p is the phonon frequency, v_s is sound velocity and k is the wave vector, the phonon density states for 3D is in form of,

$$g(\omega_{\mathrm{p}}) = \frac{V_{\mathrm{vol}}}{2\pi^2 v_{\mathrm{s}}^3} \omega_{\mathrm{p}}^2 \tag{1.12}$$

This is the Debye density of states, which is widely used in thermal property modeling discussed in **Ch. V**. The key assumption for this Debye model is the frequency is

capped by a cut-off frequency, $\omega_{\mathrm{p,max}}$, because no mode with wavelength smaller than the lattice spacing can exist. The definition of the Debye temperature,

$$T_{\mathrm{Debye}} = \frac{\hbar\omega_{\mathrm{p,max}}}{k_B} \tag{1.13}$$

The more realistic phonon DOS (**Figure 1.6**) can be obtained using a more realistic dispersion relation, such as **Figure 1.5**.

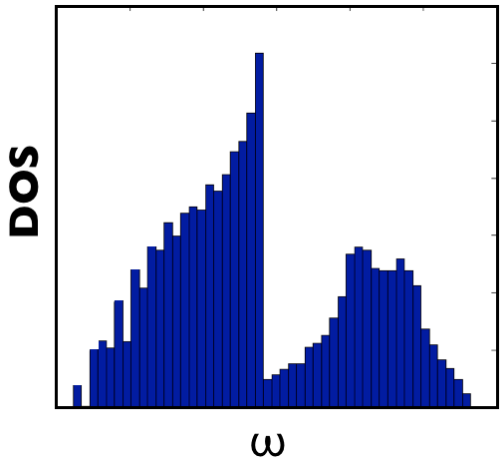

Figure 1.6: Phonon DOS of F.C.C. monoatomic lattice calculated by lattice dynamics - **Eq 1.7**. (Figure by Yansha Jin)

Lastly, the phonon quanta are introduced in the language of second quantization. Back to 1D monatomic lattice, the harmonic potential contains cross terms (**Eq 1.5**). Transformation using a set of orthonormal basis $\{Q_n\}$ can get rid of these terms,

$$H_{\mathrm{ph}} = \frac{1}{2}\sum_n m\dot{u}_n^2 + \frac{1}{2}K_{\mathrm{sp}}\sum_n (u_n - u_{n+1})^2 = \frac{1}{2}\sum_n m\dot{Q}_n^2 + \frac{1}{2}\sum_n \omega_{\mathrm{p}}^2 Q_n^2 \tag{1.14}$$

After introducing the basic creation and annihilation operators for the Bosons, the Hamiltonian yields,

$$H_{\mathrm{ph}} = \sum_Q \hbar\omega_{\mathrm{p}}(b_Q^\dagger b_Q + \frac{1}{2}) \tag{1.15}$$

where b_n and $b_n^\dagger$ are the annihilation and creation operators for the phonons, the

$N_Q = b_Q^\dagger b_Q$ is the phonon number operator. The energy is discrete and can only increase in a quantum of $\hbar\omega_{\mathrm{p}}$.

Applying the second quantization formalism to the excitons (**Eq A.3**), the Hamiltonian of the dimer can be expressed as:

$$H_{\mathrm{dim}} = \sum_{M=1,2} (E_g + V_{eg,eg} - V_{gg,gg}) a_M^\dagger a_M + J_{12}(a_1^\dagger a_2 + a_2^\dagger a_1) + U_{12} a_2^\dagger a_1^\dagger a_2 a_1 \quad (1.16)$$

where a_n and $a_n^\dagger$ are the annihilation and creation operators for the excitons. The third term in **Eq 1.16** represents the energy for bi-excitons that are often ignored (*Agranovich and Bassani* (2003)).

Combining **Eq 1.15** and **Eq 1.16** while including the charge-phonon interactions, the Hamiltonian for the "Polaron" is obtained in the next subsection (**Subsection 1.1.3**).

1.1.3 Polarons

In organics solids, the localized charge carriers are surrounded by a cloud of virtual phonons, called "polarons". The atoms will deviate from their equilibrium positions in the presence of a charge carrier, and how far these distortion extend is referred to as the polaron radius, r_{pol}. Group III-V semiconductors usually have $r_{\mathrm{pol}} > 100$ Å; for weakly bonded materials like organics, r_{pol} is often less than the lattice constant (~ 10 Å). The small polaron radius in organic solids is due to the large effective mass of the excitons. (*Ranninger* (2006))

The charge-phonon coupling constant defines the strength of the interaction between the charge and the lattice vibrations; and the larger the effective mass, the smaller the polaron radius and the larger the charge-phonon coupling constant will

be. The Fröhlich charge-phonon coupling constant, g, is written as,

$$g = \frac{e^2}{\epsilon_{\text{pol}}} \sqrt{\frac{m^*}{2\hbar^3 \omega_{\text{LO}}}} \tag{1.17}$$

where ϵ_{pol} is the dielectric constant of polaron and m^* is it effective mass, ω_{LO} is the longitudinal optical phonon frequency.

Once the exciton, phonon and charge-phonon coupling are all well-defined, the Hamiltonian of the polaron yields,

$$H_{\text{pol}} = \sum_{MN} J_{MN} a_M^\dagger a_N + \sum_Q \hbar\omega_Q (b_Q^\dagger b_Q + \frac{1}{2}) + \sum_{MQ} \hbar\omega_Q g_{MM}^Q (b_Q^\dagger + b_Q) a_M^\dagger a_M \tag{1.18}$$

where the first term in **Eq 1.18** is the dipole interaction, generalized from the second term in **Eq 1.16**; the second term in **Eq 1.18** is the Hamiltonian for the phonons (**Eq 1.15**); the last term is the charge-phonon interaction, where $(b_Q^\dagger + b_Q)$ is the phonon displacement operator and g_{MM}^Q is the charge-phonon coupling constant between M-th exicton and Q-th phonon (**Eq 1.17**). Starting with this complicated Hamiltonian, "thermal" factors in organic charge transport are discussed.

1.1.4 "Thermal" Factors

The experimental explorations on the organic charge mobility showed different temperature dependence for crystalline and disordered organics. In *Warta and Karl* (1985), a decrease in mobility with temperature in crystalline ultrapure naphthalene was observed. In contrast, the temperature dependence was the opposite in *Veres et al.* (2003): the hole mobility decreased with the inverse of the temperature in PTAA1 and fluorene-thiophene copolymer. (See **Figure 1.7**).

The differences and the corresponding theories were discussed in the review of *Coropceanu et al.* (2007). For crystalline organics, the temperature dependence of mobility follows the empirical power law $\mu \propto T^{-\alpha}$ where α ranges from -0.5 to 3. This

dependence can be understood as that the relaxation time τ_e (in **Eq 1.1**) decreases due to increasing phonon scattering at high T. Another approach to explain the inverse relation starts with the narrow band nature of the organics: since the band width is comparable to the thermal energy, k_BT at 300K, the coherent charge transport is disrupted by the thermal energy under room temperature. The coherent part of the mobility can be written following the Boltzmann transport equation:

$$\mu_{\text{coh}} = \frac{\sqrt{\pi}e\tau_e}{2N_c k_B T} \int_{\mathbf{k}} n_{\mathbf{k}}(1 - n_{\mathbf{k}})(v^*)^2 d\mathbf{k} \tag{1.19}$$

where N_c is the number of the charge carriers, $n_{\mathbf{k}}$ is the Fermi-Dirac or Bose-Einstein distribution depending on the charge of the particles. v^* is the group velocity derived from m^*.

Strong charge-phonon coupling and the impurities in the crystals both create "traps". If the depth of these traps is larger than k_BT, the coherent transport will be hindered. Therefore, in highly disordered systems, charge transport is phonon-assisted and proceeds via hopping. The temperature dependence of the hopping transport follows Arrhenius-like law:

$$\mu_{\text{hop}} \propto \exp(-\Delta/k_BT) \tag{1.20}$$

where Δ is the activation energy that increases with the disorder level. Other methods like Monte-Carlo simulation (*Bassler* (1993)) produce different temperature dependence, such as

$$\mu_{\text{hop,MC}} \propto \exp(-T_{\text{dis}}/T)^2 \tag{1.21}$$

$\mu_{\text{hop,MC}}$ is the Monte-Carlo simulated mobility, where T_{dis} represents the disorder.

An extensive discussion of the polaron model is presented in **Appendix B**, adapted from *Ortmann et al.* (2009). The modeling results are shown in **Figure**

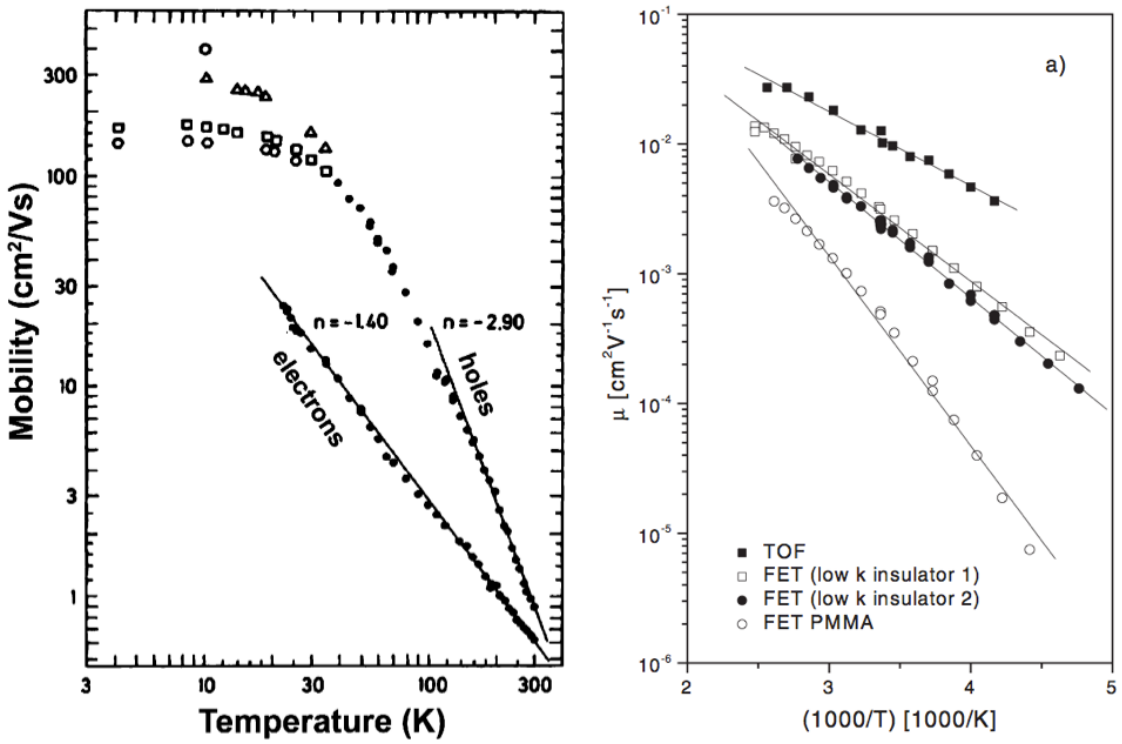

Figure 1.7: Organic materials' charge mobility versus temperature. (Left) *Warta and Karl* (1985)) showed that the mobility decreases with temperature. (Right) *Veres et al.* (2003) presented a contradicting trend: mobility decreases with the inverse of the temperature. The differences between these two works are the crystallinity of the organic materials. Crystallized(Left) and disordered(right) organics lead to different temperature dependence of charge mobility.

1.8. The total mobility of the organic materials in this theoretical analysis is the sum of the coherent and incoherent contribution,

$$\mu = \mu_{coh} + \mu_{inc} \tag{1.22}$$

Incoherent transport (dashed) dominates in high temperature regime, while coherent transport (dotted) is more important at low temperature. But at high T, the coherent mobility approaches zero due to the $1/T$ dependence and the polaron effective mass $m^*_{\rm pol} = m^* \exp(\sum_{\mathbf{Q}} g^2_{\mathbf{Q}})$ becomes larger as temperature increases.

The incoherent mobility at low T is negligible, because,

$$\mu_{\text{inc,low}} \sim \frac{g_{\mathbf{Q}}^2}{T} e^{-\hbar\omega_{\mathbf{Q}}/k_B T} \tag{1.23}$$

and at high T, the incoherent mobility yields,

$$\mu_{\text{inc,high}} \propto T^{-3/2} e^{-E_{\text{pol}}/k_B T} \tag{1.24}$$

this effect is also referred to as self-trapping and the polaron energy is the reorganization energy of the molecules which can be written as

$$E_{\text{pol}} = \frac{1}{2} g_{\mathbf{Q}}^2 \hbar\omega_{\mathbf{Q}} \tag{1.25}$$

where $g_{\mathbf{Q}}$ is the charge-phonon coupling constant of phonon mode $\mathbf{Q}$; $\hbar\omega_{\mathbf{Q}}$ is the energy of the phonon in this mode.

Note that, the charge-phonon coupling is a crucial parameter for organic charge transport (See **Figure 1.8**) and the phonon energy can affect the charge transport as well. However, there were no adequate study on the thermal properties and the phonon dynamics for organic materials, and this missing knowledge will be discussed in **Ch. III** and **Ch. V**.

In conclusion, charge and heat transport are interconnected. Thus, it is vital to characterize the thermal properties of thin-film phase organics in order to better understand the performance of organic-based devices at the molecular level.

1.2 Systematic Thermal Analysis

Thus far, the discussion has been confined to the thermal effects at microscopic level. In this section, the heating effects are considered macroscopically.

The great demand for smaller, faster and more efficient electronic devices has led

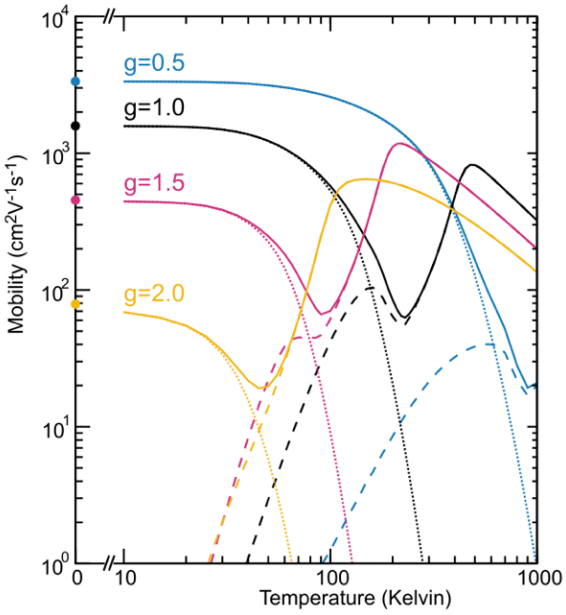

Figure 1.8: Theoretical calculation of charge mobility of organics from *Ortmann et al.* (2009). The solid lines represent the total charge mobility. The coherent (dotted lines) and incoherent (dashed lines) contributions are also plotted. The mobility strongly depends on the electron-phonon coupling constant g, which is referred to as $g_{\mathbf{Q}}$ in this thesis.

to a higher power consumption density. For example, the power density P_{mp} of a microprocessor is written as

$$P_{\mathrm{mp}} = NCV^2 f \tag{1.26}$$

where N is the number density of the devices, f is the operating frequency and C and V are the capacitance and the voltage of the operating device. Higher N and f result in a higher power dissipation and higher heat generation.

Figure 1.9 (left) is a picture of the Google data center in North Carolina. The servers in the room are operating year-around and producing a huge amount of waste heat and considerable effort has been made to redirect and utilize this waste energy. In this Google data center, a massive water cooling system (**Figure 1.9** (right)) is driving the excess heat away, which prevents the overheating of the crucial components in the servers. Similar data centers have been reported to redirect heat to the nearby households, offices, swimming pools and greenhouse. Considerable research efforts

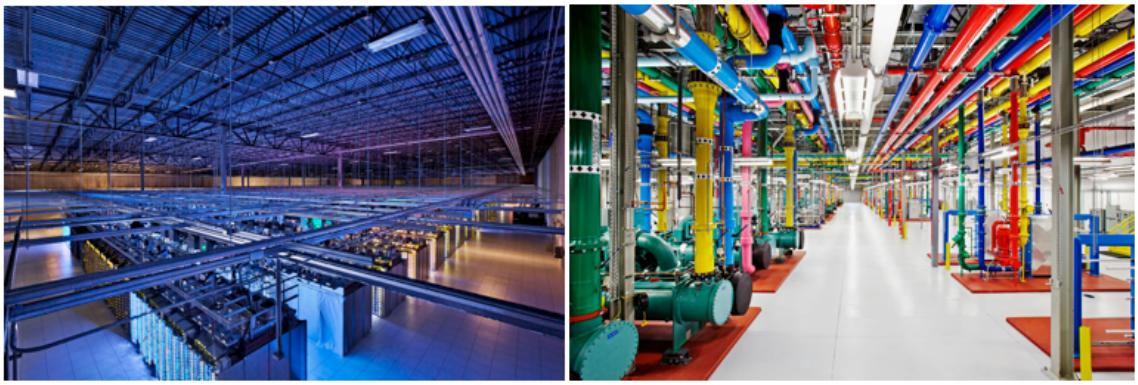

Figure 1.9: Data centers consume huge amounts of electricity, estimated to be up to 1.5 percent of all the world's electricity. The left image shows the google data center at North Carolina. However, prodigious amount of the electricity is dumped as heat. If it is not for the water cooling plants (Right), the temperature accumulations can cause overheating problems to the crucial components. (Figure from the web: http://mpictcenter.blogspot.com/2012/10/google-throws-open-doors-to-its-top.html.)

focus on heat management at the environmental level, but their overview is beyond the scope of this thesis. The focus of my work is the thermal management and analysis at device and packing levels.

Analysis at the device level includes the estimation of how much heat is generated inside the device and how long the device can operate. Increasing power density and current levels, as mentioned before, generates more heat and this overheating can be catastrophic to the electronic devices. The device temperature has to be maintained at a reasonable level to prevent thermal failure and to extent the operation lifetime. Therefore, the heat is directed out of the device and handled at the packaging level: advanced packaging materials must have enough thermal dissipation power and micro-cooling devices are often integrated into the electronic packaging. One of the micro-cooling device, TE device, will be introduced in **Section 1.3**.

1.2.1 Heating in Organic Light-Emitting Diodes

The rest of **Section 1.2** discusses the thermal analysis of Organic Light Emitting Diodes (OLED). The amount of the temperature increase in a conventional LED is written as (*Efremov et al.* (2006))

$$\Delta T = (1 - \eta_{\text{eff}}) W k_{\text{th}} d_{\text{LED}} / A_{\text{LED}} \tag{1.27}$$

where ΔT is the amount of the temperature increase, η_{eff} is the efficiency of the LED, W is the driving power, k_{th} is the effective thermal conductivity and d_{LED}, A_{LED} are the device thickness and active area, respectively. In the case of organic LEDs, whose sample structure is shown in **Figure 1.10** (*Agrawal et al.* (2013)), the total thickness of the active layers is less than 200 nm while the substrate thickness is a thousand times larger. Therefore, it is the thermal properties of the substrate and packaging materials that most affect the temperature build-up in the device. *Chung et al.* (2009) demonstrated the substrate's effect on heat dissipation in OLED, see **Figure 1.11**. Heat dissipation is more efficient for OLED on silicon substrate than the same device on other low thermal conductivity substrates, such as glass and stainless steel. However, glass is the most common substrate for OLEDs due to its transparency. The temperature increase of OLED on glass is significant: T rises to 65 °C after a 3-minute operation. Further increase of the device temperature can cause degradation of the thin-film organics and result in the device failure. *Adamovich et al.* (2005) showed the critical temperature of operation (120 °C) for two specific types of OLED (Red RD61 and Green GD33).

As mentioned above, **Eq 1.27** indicates that the organic layers in OLED are so thin that they barely contribute to the temperature increase. Here, I present a simple simulation of the heat dissipation in OLED active layers, showing the speed of the thermalization process inside these organic layers. The simulation follows transient

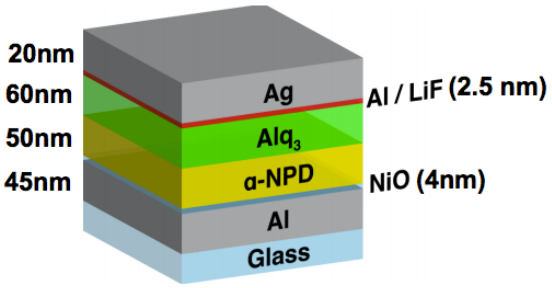

Figure 1.10: Materials was deposited onto glass substrate using VTE. From bottom to top: Al (40 nm)/ NiO (4 nm)/$\alpha-NPD$ (50 nm)/Alq_3 (60 nm)/Al:LiF (2.5 nm)/Ag (20 nm). (Figure from *Agrawal et al.* (2013))

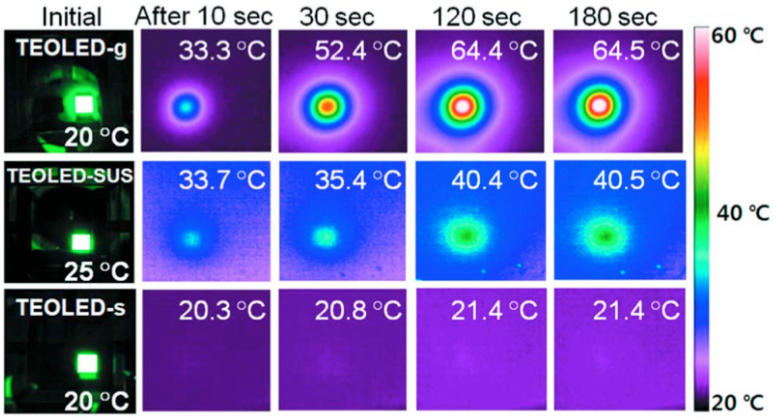

Figure 1.11: IR images of the temperature profile of the operating OLEDs on different substrates. Substrate: Glass (Top); Substrate: Stainless Steel (Middle); Substrate: Silicon (Bottom). (Figure from *Chung et al.* (2009))

heat conduction equation

$$k_{\text{th}}\nabla^2 T + q_{\text{th}} = C_{\text{p}}\frac{dT}{dt} \tag{1.28}$$

where C_{p} is the heat capacity at constant pressure and q_{th} is the heat flux related to the current density and the device efficiency. Applying **Eq 1.28** to the OLED structure in **Figure 1.10** while assuming the heat generation is confined in organic active layer (aluminum hydroxiquinoline (Alq_3)) with rate of 1 W/cm^2, the temperature profile is calculated and the results are shown in **Figure 1.12**. The temperature at the top surface, which is exposed to the ambient, rises quickly to match the temperature of the active layer within 1 ns; due to the low thermal conductivity of the organic hole

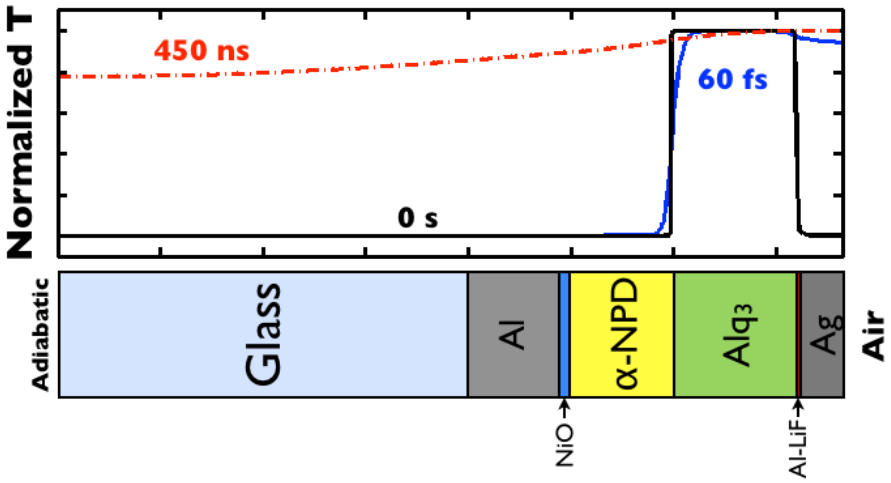

Figure 1.12: Transient temperature profile of the OLED in **Figure** 1.10 modeled at 0s, 60fs, 450 ns. Thermalization within the organic layers is less than 60 fs. (Figure by Yansha Jin)

transport layer N,N'-di-1-naphthyl-N, N'- diphenyl-1, 1'-biphenyl-4, 4'diamine (NPD) and the glass substrate, the thermalization process at the bottom side is comparably slower. In less than 1 μs, the temperature distribution in the organic layers becomes nearly uniform. Thus, if one is interested in investigating the microscopic "heating" processes in the organics, the time resolution should be several nano-seconds.

However, the thermal conductivity of organic layers is still crucial for OLEDs, especially when analyzing nano-scaled features. One major advantages of organic materials lies in the large-area lighting applications. However, as the size of the OLED increases, the "hot spots" become unavoidable. The hot spots originate from the rough surface of the substrate, even a tiny spike can cause current crowding and local heat generation (*Park et al.* (2011)). The localized current injection was also observed in nanoscale light sources (*Zhao et al.* (2007)), where OLED was deposited onto an Atomic Force Microscopy (AFM) tip. Shown in **Figure 1.13**, heat accumulates at the tip due to the high local current density, and the organic materials melted after the standard operation.

The breakdown mechanism of nanoscale features such as hot spots, edges and

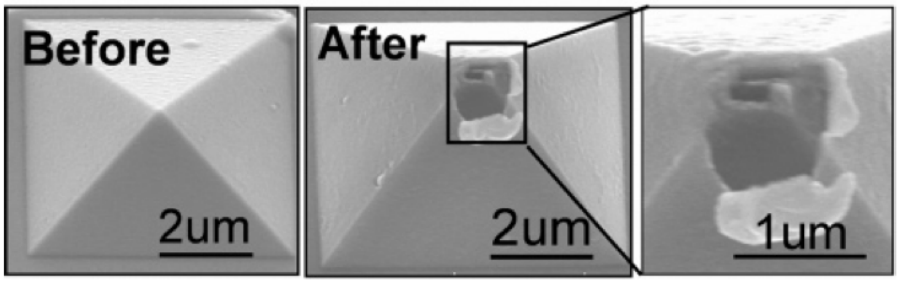

Figure 1.13: Thermal failure of non-planar OLED causing by local joule heating. SEM images of the organic heterostructure device on AFM probe tip before and after normal operation; The region at the center of the tip melted and imaged at 2× magnifications; The intense joule heating at this region is due to the tip geometry. (Figure from *Zhao et al.* (2007))

tips is closely related to the thermal conductivities of the organic layers. Thus, the characterization of thermal conductivity of these organic semiconductors in thin-film phase is crucial for analyzing the device performances.

1.3 Thermoelectrics

Two problems originated from the excessive heating in electronic devices have been briefly discussed in the previous section (**Section 1.2**) : how to cool down the devices and how to manage the waste heat. The use of TE devices can be the solution to both because of their ability to convert temperature gradients into voltage, and can also realize the conversion in a reverse direction.

1.3.1 Thermoelectric Effects

To cool down a hot component using a thermoelectric device, one can apply a voltage to create a temperature difference. This phenomena is called thermoelectric cooling effect, also known as Peltier effect. The image of a commercial Peltier cooler is shown in **Figure 1.14**. A temperature difference can be generated between the top and the bottom side of the device with the applied voltage, causing heat extraction from the cold side to the hot side. Attaching the electronic device to the cold side,

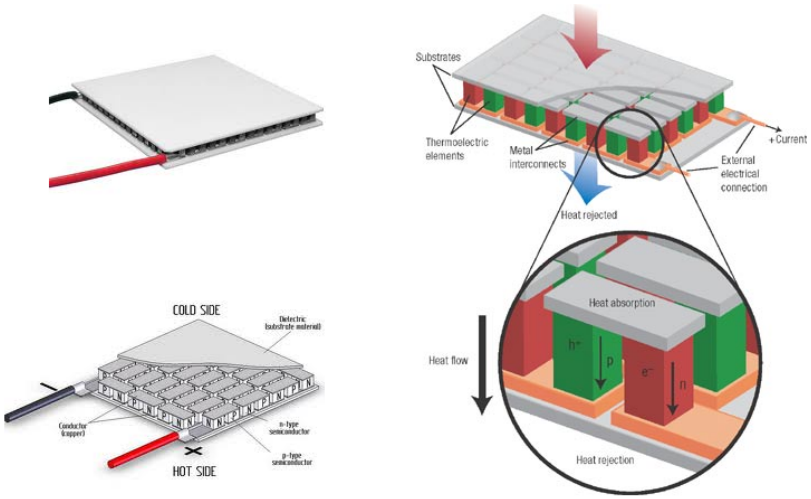

Figure 1.14: The working principle and the schematic drawing of the Peltier cooler. The image on the left shows the real design of a Peltier cooler. The right image shows the working principle by drawing the Seebeck circuit. "The Peltier effect is the presence of heating or cooling at an electrified junction of two different conductor" - defined by Wikipedia. (Left image from the web: http://www.kryotherm.ru/?tid=23 and Right image from *Snyder and Toberer* (2008))

the heat generated in the device can be directed out. In this way, the device can be maintained at its normal operating temperature.

To manage the waste heat, one can scavenge the unused heat to create a "hot side": the temperature difference converts to electricity within the TE device. This conversion is the well-known Seebeck effect and the corresponding devices are often referred to as the thermoelectric generators.

Despite how promising the principle seems to be, challenges remain in making the thermoelectric devices more efficient and cost-effective.

1.3.2 Efficiency of Thermoelectric Devices

The relation between the temperature difference, $\Delta T = T_h - T_c$, (T_h, hot side temperature and T_c, cold side temperature), and the electric voltage, ΔV, is written as

$$\Delta V = -S\Delta T \tag{1.29}$$

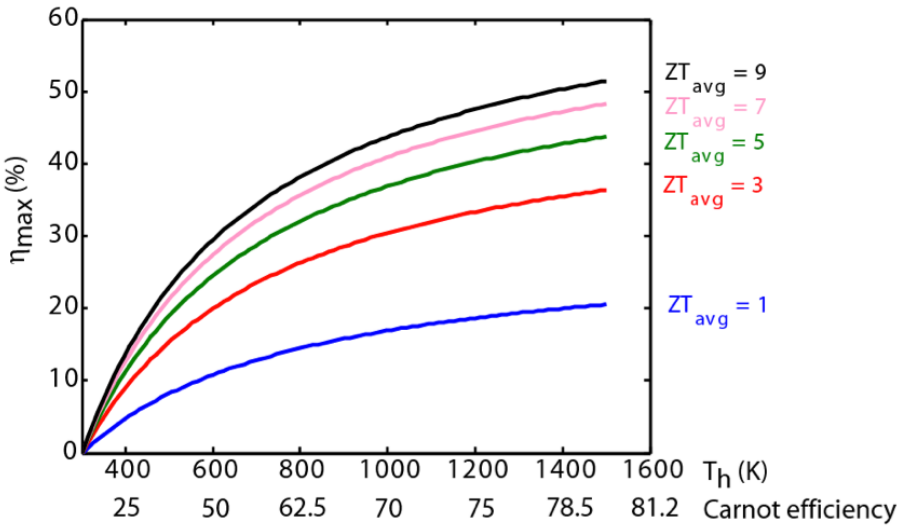

Figure 1.15: TE efficiency versus temperature with various of ZT. The maximum efficiency of thermoelectric device increases with ZT. (Figure from *Yadav* (2010))

where S is the thermopower, also known as Seebeck coefficient. The maximum efficiency for a thermoelectric generator is

$$\eta_{\max} = (1 - \frac{T_h}{T_c}) \frac{\sqrt{1 + ZT_{\text{avg}}} - 1}{\sqrt{1 + ZT_{\text{avg}}} + \frac{T_c}{T_h}} \tag{1.30}$$

where Figure of Merit (ZT) is

$$Z = \frac{\sigma_e S^2}{k_{\text{th}}} \tag{1.31}$$

and $T_{\text{avg}} = \frac{1}{2}(T_c + T_h)$. The relation between $\eta_{\max}$ and T_h at different ZT_{avg} is plotted in **Figure 1.15** (*Yadav* (2010)) while setting T_c to be room temperature. It is evident that material with a larger ZT_{avg} can make better TE devices at the same operating temperature T_h. Usually, a material that exhibits $ZT_{\text{avg}} \sim 1$ is considered as a promising candidate for TE.

To obtain a larger ZT_{avg}, a larger S, a smaller k_{th} and a large σ_e are desired. However, this is a conflicting combination of material properties (*Snyder and Toberer* (2008)).

The Seebeck coefficient S for metals or degenerate semiconductors is given by: (*Cutler et al.* (1964))

$$S = \frac{8\pi^2 k_B^2}{3eh^2} m^* T (\frac{\pi}{3n})^{2/3} \tag{1.32}$$

where m^* is the effective mass of the carrier and n is the carrier concentration. Small n benefits the thermopower, S. A large electrical conductivity, however (See **Eq 1.1**), requires a large n. Moreover, k_{th} often increases with σ. The electron (charge) contribution to thermal transport $k_{\text{th,e}}$ in **Eq 1.11** is directly related to σ,

$$k_{\text{th,e}} = \sigma L_{\text{wf}} T \tag{1.33}$$

where L_{wf} is the Lorenz factor. L_{wf} is 2.4×10^{-8} $\text{J}^2\text{K}^{-2}\text{C}^{-2}$ for the free electron (*Snyder and Toberer* (2008)). Achieving the combination of the desired material properties seems to be a mission impossible for conventional materials, but the nanoscale manipulation of materials' structure provides many novel pathways to overcome this difficulty. Moreover, ZT will not remain constant while temperature changes, **Figure 1.15** is just an unrealistic illustration. ZT's relation versus the temperature of several materials is shown in More details on the nanostructure manipulation to increase ZT will be discussed in **Ch. IV**.

1.3.3 Organic Thermoelectrics

Organic materials have low thermal conductivity k_{th} and large effective mass m^* intrinsically that are both desired for TE materials. One of the major problematic properties is its low electrical conductivity, σ_e. Highly conductive polymers and organic semiconductors with higher σ_e were investigated for the potential in making TE devices. With the scalability and the affordable price of the organics, cost-effective TE devices for the large-scale heat harvesting can be realized potentially.

k_{th} plays an important role in the efficiency of thermoelectric materials, as can

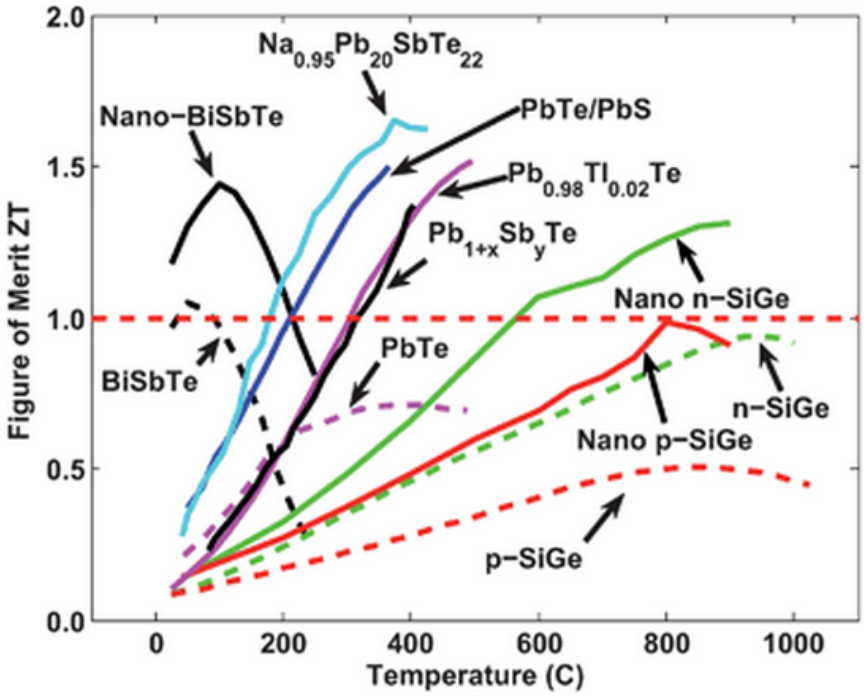

Figure 1.16: ZT versus temperature for several materials. (Figure from *Minnich et al.* (2009))

be seen in **Eq 1.31**. But no adequate study has explored the thermal properties of organic semiconductors and research on organic thermoelectrics is not mature. Recently, many interesting studies have presented some promising results for organic TE (*Kim et al.* (2011); *Wang et al.* (2009)) and proposed ways to optimize ZT_{avg} in organics (*Bubnova et al.* (2011); *Aïch et al.* (2009)).

In this thesis, the measurements and discussions on the thermal conductivity of organic semiconductors and organic/inorganic hybrids, along with novel ideas for the next generation organic thermoelectric devices are presented. (Refer to **Ch. III**, **Ch. V** and **Ch. IV**)

1.4 Organization of the Thesis

Thermal properties of the disordered organic solids are crucial for researching the charge transport and the mobility characterization of the organic semiconductor;

also crucial for the thermal analysis of the thin-film organic electronic devices and the performance of organic thermoelectric devices. Despite the importance of the research, there has yet to be a complete study on the thermal properties of organics and its hybrids with the inorganics. In this thesis, organic thermal conductivities are measured and interesting facts of the interfacial contribution at organic/metal interfaces are discovered. The boundary/interfacial contribution to the thermal transport cannot be neglected in thermal analysis of nanostructured organic optoelectronic/thermoelectric devices. Especially for thermoelectric devices, the boundary effect can assist in enhancing the figure of merit in organic/metal nanocomposites. The fundamental physics of this boundary effect is also discussed.

The organization of the thesis is as follows,

Chapter II gives a review on the thin-film thermal properties measurement techniques, focusing on the technique used for this work, the 3-ω method.

Chapter III reports the results of the thermal conductivity measurements on organics and organic/metal hybrids. The concept, thermal boundary conductance, is introduced and its significance in organic/metal systems is presented.

Chapter IV continues the discussions on the boundary effect with a focus on the impact to the thermoelectric material design.

Chapter V and **Chapter VI** focuses on the fundamentals of the thermal boundary conductance at the interfaces involving organics, along with an extensive discussion on the existing analytical and computational modeling techniques.

The final chapter, **Chapter VII** presents the summary for the present work and further research directions.

CHAPTER II

Methods for Thin-Film Thermal Property Measurements

The unit of thermal conductivity k_{th} is W/mK, suggesting that k_{th} is the transmitted power under a temperature gradient per unit thickness,

$$k_{\text{th}} = \frac{d}{A}\frac{q}{\Delta T} \tag{2.1}$$

Eq. 2.1 is the governing equation for the thermal conductivity measurement: for a sample with a known dimension, its thermal conductivity can be calculated from the measured quantities: the driven power q and the temperature difference ΔT.

Figure 2.1 shows the giant apparatus for thermal conductivity measurement in 1967. This early apparatus was based on steady-state method, with the sample is at the equilibrium state. The main disadvantages of the steady-state method are the long time to reach equilibrium and the radiative energy loss at room temperature.

These disadvantages can be avoid in the transient measurements. Well-known transient measurements include the 3-ω method and the Time-Domain Thermoreflectance (TDTR) method. 3-ω method is simpler to operate and cost-effective; TDTR is a non-contact method based on the pump-probe technique. Both these methods are discussed in detail in the following sections (**Section 2.1** and **Section**

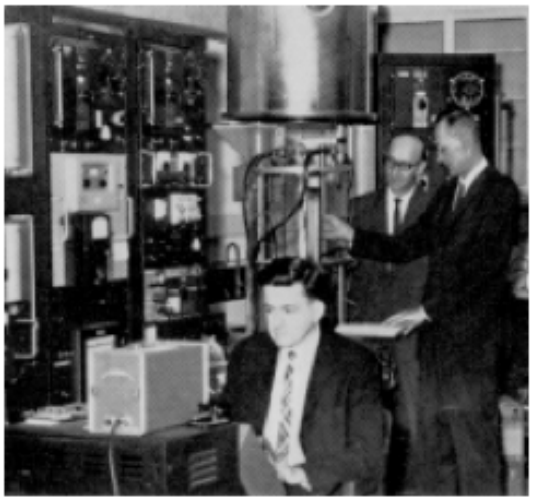

Figure 2.1: Thermal measurement apparatus in the 1960s. Scientist Robison and Powell discussing the operation of the giant apparatus. (Figure from nist.gov)

2.2). 3-ω is the main technique used in this thesis work, and this chapter contains an extra section describing the experimental set-up and the data reductions of the 3-ω method for organic thin films.

2.1 Three-Omega Method

3-ω method was developed by *Cahill* (1990), which not only overcame the difficulty in radiative heat loss and also enabled the thermal conductivity measurements for nano-scaled thin films.

The principle of the 3-ω method is shown in **Figure 2.2**. A metal wire with four contact pads is deposited onto the thin-film of interest, acting both as a heater and a thermometer. An periodic current at a frequency, ω, is passed through the two outer pads of the metal wire , $I = I_0 \cos(\omega t)$; the electric power, as a results, oscillates at 2ω, $P = I_0^2 R_0(1 + cos(2\omega t))$. The temperature change of the metal wire yields,

$$T = T_0 + T_{2\omega} \cos(2\omega t + \phi) \tag{2.2}$$

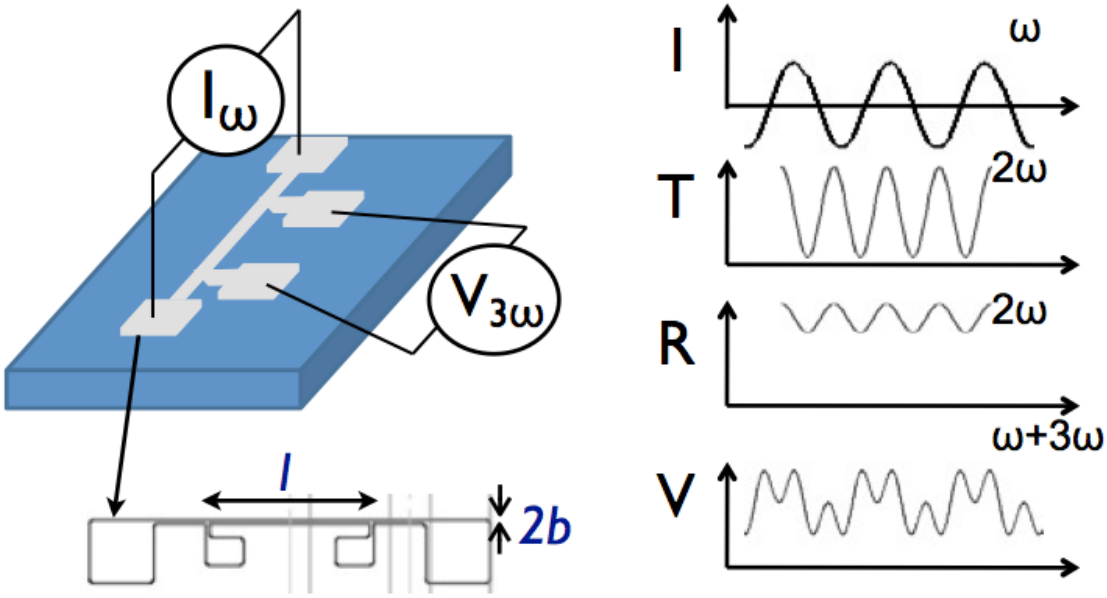

Figure 2.2: Schematic Illustration of 3-ω method for thermal conductivity measurements. (Left) The thin film is deposited onto a planar substrate and a metal wire with four contact pads is deposited atop of the thin film. The exact design of the metal wire is $l = 4mm$ and $2b = 80\mu m$; Simply illustration of the principle of the 3-ω method for thermal conductivity measurements is presented in the right image: A periodic current with frequency ω is passed through the two outer contact pads, the electric power is oscillating at double the frequency. The temperature rise in the wire correlates to the power and k_{th} of the film of interest and also owns a frequency of 2ω. However, the temperaure rise ($T_{2\,\omega}$) is too small to detect accurately; so instead probing the temperature signal, 3-ω method measure the voltage signal between the two inner pads which contains the information of $T_{2\omega}$. Voltage signal can be amplified by lock-in amplifier and measured at higher frequency. (Figure by Yansha Jin and Dr. Abhishek Yadav)

where ϕ is the phase shift. This temperature fluctuation correlates to the thermal conductivity of the thin film underneath the metal wire. With a small temperature fluctuation, $T_{2\omega} \sim 5K$, the resistance of metal reacts linearly to the temperature,

$$R = R_0 + R_0 C_{rt} T_{2\omega} \cos(2\omega t + \phi) \tag{2.3}$$

where R is the resistance, R_0 is the initial resistance; and C_{rt} is the resistance temperature coefficient, which is written as,

$$C_{rt} = \frac{\Delta R}{R_0 \Delta T} \tag{2.4}$$

As a result, the voltage probed from the two inner pads yields,

$$\begin{aligned} V &= IR = I_0 \cos(\omega t)(R_0 + R_0 C_{rt} T_{2\omega} \cos(2\omega t + \phi)) \\ &= I_0 R_0 \cos(\omega t) + I_0 R_0 C_{rt} T_{2\omega} \frac{1}{2}(\cos(3\omega t + \phi) - \cos(\omega t + \phi)) \\ &= V_\omega \cos(\omega t + \phi') + V_{3\omega} \cos(3\omega t + \phi) \end{aligned} \tag{2.5}$$

For nanoscaled thin films, the temperature fluctuation $T_{2\omega}$ is too small for direct measurements. 3-ω method provides a way to transfer this temperature signal to a voltage signal, $V_{3\omega}$, which can be amplified using a lock-in and detected at a higher accuracy.

The temperature fluctuation can be extracted from the experiment using the measured quantities,

$$T_{2\omega} = \frac{2V_{3\omega}}{I_0 R_0 C_{rt}} \tag{2.6}$$

However, this fluctuation's relation to the thermal conductivity is much more complicated than **Eq 2.1** considering a 3 -D film with a line heater. Following the Fick's

law and the Fourier's law, $T_{2\omega}$ yields (*Cahill* (1990)),

$$T_{2\omega} = \frac{P}{l\pi k_{\text{th}}} \int_0^\infty \frac{\sin^2(kb)}{(kb)^2(k^2+q^2)^{1/2}} dk \tag{2.7}$$

where $2b$ is the width of the metal line heater; q is the penetration depth, defined as,

$$q = (\kappa/2i\omega)^{1/2} \tag{2.8}$$

where κ is the thermal diffusivity,

$$\kappa = \frac{k_{\text{th}}}{\rho C_v} \tag{2.9}$$

Under the condition $|qb| \ll 1$, the temperature fluctuation calculated from the heat conduction model **Eq 2.7** can be approximated as,

$$T_{2\omega} = \frac{P}{2\pi l k_{\text{th}}}[\ln(\frac{\kappa}{b^2}) - \ln(2\omega)] - i\frac{P}{4lk_{\text{th}}} = T_{\text{in-phase}} + T_{\text{out-phase}} \tag{2.10}$$

Comparing **Eq 2.7** and **Eq 2.6**, the temperature fluctuation from a periodic current load can be measured and calculated. The calculation has only one sensible parameter, the thermal conductivity of the film, k_{th}. **Figure 2.3** shows the in-phase $T_{2\omega}$ for a 45 nm SiO_2 film deposited on Si substrate (*Lee and Cahill* (1997)). The markers are the experimental values while the curves represent the $T_{\text{in-phase}}$ calculated using SiO_2's thermal conductivity. The agreement between experimental and calculation confirms the validity of the 3-ω method for k_{th} measurements.

Recall that steady-state methods are not applicable at room temperature due to

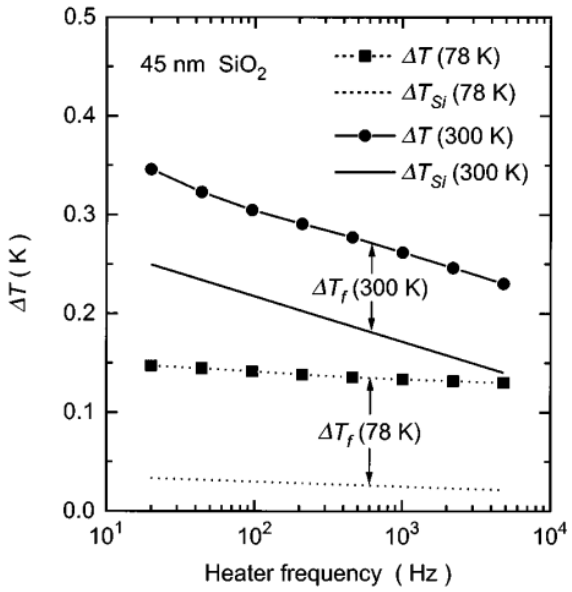

Figure 2.3: An example data analysis of 3-ω measurement. In-phase $T_{2\omega}$ calculated from $V_{3\omega}$ for a 45 nm SiO_2 film on Si substrate. (Figure from *Lee and Cahill* (1997))

the large radiative loss. In 3-ω method, the radiation heat loss is,

$$G_{\text{rad}} \simeq 2\sigma\epsilon T^3(2A) = 2\sigma\epsilon T^3(2l|1/q|) \tag{2.11}$$

the total heat generation rate is $G \simeq lk_{\text{th}}$ and the radiation error of 3-ω method yields,

$$G_{\text{rad}}/G \sim |1/q|T^3 \tag{2.12}$$

Generally, if $|1/q| < 100\mu m$, the radiation error is negligible.

3-ω method has been shown to be accurate for many inorganic dielectric materials and some organic semiconductors (*Kim et al.* (2005)). In this thesis, I will discuss in-depth how to apply this method to more organic semiconductors and extend the study to organic/inorganic hybrids. A detailed discussion of the 3-ω method for organics is presented in the last section (**Section 2.3**) of this chapter .

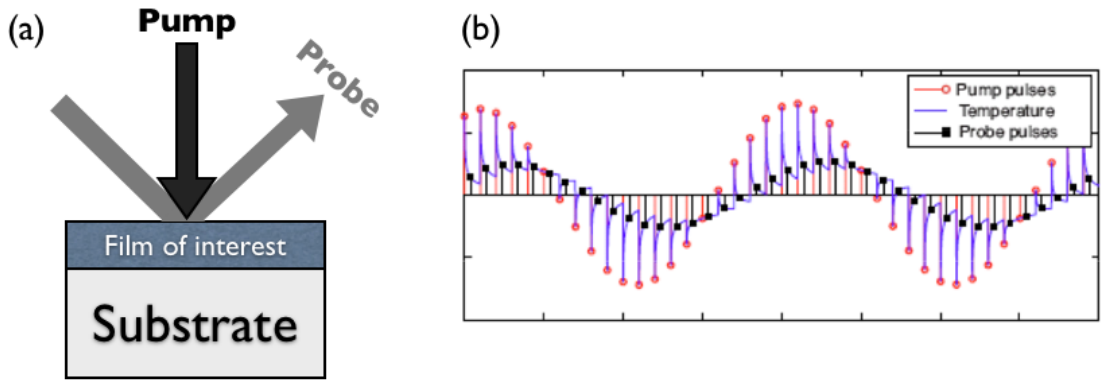

Figure 2.4: Principle of TDTR thermal conductivity measurement. A pump pulse introduces local heating and temperature rises suddenly then exponentially decay during the interval of the pump pulses. The probe pulse follows to detect the instant change in reflectance caused by this local heating. (Figure from *Schmidt et al.* (2008) and adapted by Yansha Jin)

2.2 Time-Domain Thermo-Reflectance Method

Besides introducing temperature gradient using electrical heating like the 3-ω method, supplying heat by laser beam is another promising alternative in thermo-property measurements.

Time-domain Thermoreflectance (TDTR) is the method based on laser heating. Picosecond or nanosecond laser pulses introduce the thermal energy to the thin films, and the changes in the reflectance are then detected by time-delayed probe pulses.

The TDTR principle is shown in **Figure 2.4 (a)**. A pump pulse causes the local heating in the thin film structure, followed by a probe pulse to detect the instant reflectance changes caused by the local heating. In **Figure 2.4 (b)** (*Daly et al.* (2002)), the temperature profile of the film is presented (the blue line), T rises instantaneously with the pump pulses and decays exponentially during the intervals,

$$\Delta T(t) \propto \exp(-t/\tau_d), \text{ where } \tau_d = \frac{d_f d_s C_v}{k_{\text{th}}} \tag{2.13}$$

in which d_f and d_s are the thickness of the film and the substrate, respectively. The

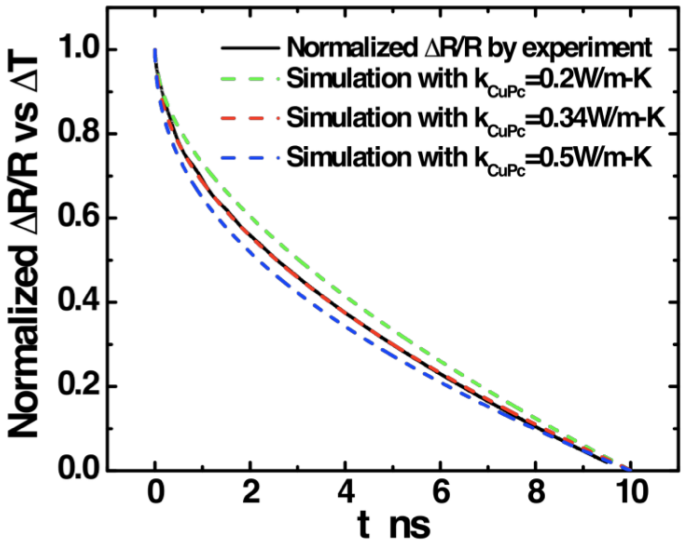

Figure 2.5: CuPc thermal conductivity measurement by TDTR. The change reflectance represents the temperature fluctuation; the best fitting yields to $k_{\text{th,CuPc}} = 0.34$ W/mK. (Figure from *Sun* (2013))

signals probed are plotted in the black line, the change in the reflectance is directly correlated to ΔT. Thermal conductivity can be extracted by fitting the calculated ΔT by 3-D heat conduction model (*Cahill* (2004)) to the measured temporal temperature profile.

Details on TDTR measurements of organic k_{th} can be found in *Sun* (2013). Measurement result for CuPc is presented in **Figure 2.5**, k_{th} is 0.34 W/mK. The fitting is very sensitive to the value of k_{th} and the error-bar is smaller than 10%.

Compared with the 3-ω method, TDTR is more versatile. For example, the strain-echoes contains information of materials' sound velocity; besides, using GHz pulses in this pump and probe techniques can excite coherent acoustic modes in the samples which enables the study on other interesting physics and applications, such as acoustic cavity (*Sun et al.* (2013)).

However, the experimental apparatus for TDTR is more complicated and expensive compared to that of the 3-ω method. If the work is only confined to thermal conductivity measurements for organics, like in this thesis, 3-ω method is preferred

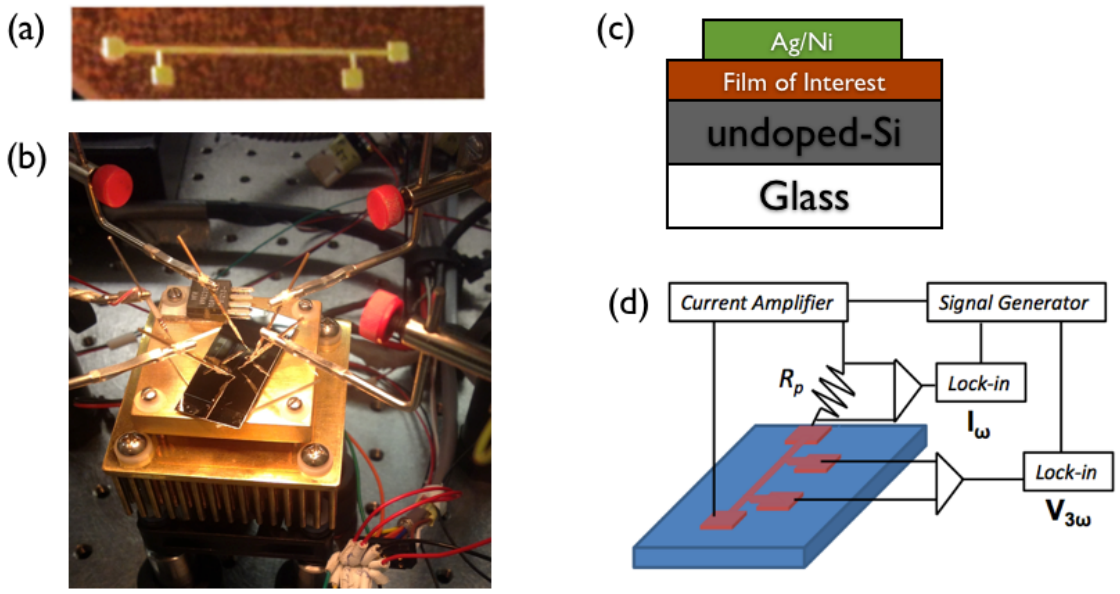

Figure 2.6: Experimental set-up for 3-ω method for the work in this thesis. (a) Top view of the heating wire on top of the film imaged by optical microscopy. (b) Sample was put on a glass slide as adiabatic bottom with a copper block and a Peltier cooler underneath. A heat sink and a fan are attached at the bottom. (c) Schematic cross-section view of the sample structure. Film is deposited on the undoped silicon substrate and placed on a glass slide. (d) Circuit design. (Figure adapted from *Jin et al.* (2012))

due to its simplicity and the satisfactory accuracy of the measurements.

2.3 Three-Omega on Organic Thin Film

In this section, the details on 3-ω measurements of organics are presented, including its limitations and technical difficulties, experimental set-up, sample preparation and data reduction details.

Borca-Tasciuc et al. (2001); *Tong and Majumdar* (2006) are excellent review papers for the 3-ω method. Effects of anisotropy, substrate-film thermal conductivity ratio, heater capacitance and substrate-film interface conductance have been discussed. The paper also compared differential and slope methods and the data reduction for the multilayer film structure.

For organic thin films, the thermal conductivity is 100 times smaller than that of the Si substrate; and the heater capacitance and the substrate-film interfacial conductance effect is negligible. Besides, there is no anisotropy to consider in the disordered organic films. Thus, the major limitation in testing organic semiconductor thin films and their hybrids with metals is the high electrical conductance of the film which might cause the parasitic current.

In order to minimize the parasitic current, highly resistive Si substrate ($\rho_s >$ 10000 Ω cm) is used. Moreover, for conductive thin films, such as CuPc/Ag hybrids, an electrically insulating capping layer is essential to be on the top of the film stack, in order to eliminate the unwanted leakage current.

The experimental set-up is shown in **Figure 2.6**. **Figure 2.6 (a)** shows the film with the metal heating wire; **Figure 2.6 (b)** is the photo of the probe station; **Figure 2.6 (c)** shows the schematic sample structure, the whole sample was placed on glass slide which is treated as an adiabatic bottom boundary; **Figure 2.6 (d)** is the drawing of the experimental circuit design by Dr. Abhishek Yadav.

If the thin-film entity contains multiple layers, the heat conduction modeling for such film is slightly modified from **Eq 2.7** (*Borca-Tasciuc et al.* (2001)),

$$\Delta T = -\frac{P}{\pi l k_{\mathrm{th},1}} \int_0^\infty \frac{1}{A_1 B_1} \frac{\sin^2(bk)}{b^2 k^2} dk \tag{2.14}$$

where

$$A_{i-1} = \frac{A_i \frac{k_{\mathrm{th},i} B_i}{k_{\mathrm{th},i-1} B_{i-1}} - \tanh(B_{i-1} d_{i-1})}{1 - A_i \frac{k_{\mathrm{th},i} B_i}{k_{\mathrm{th},i-1} B_{i-1}} \tanh(B_{i-1} d_{i-1})} \ , \ i = 2 \ldots n, \tag{2.15}$$

$$B_i = (k^2 + \frac{i2\omega}{\kappa_i})^{1/2} \tag{2.16}$$

In the above expressions, subscript i represents the i-th layer starting from the top surface. Following these relations, the temperature change can be calculated by different k_{th} input, then compared with the experiment to extract the most accurate

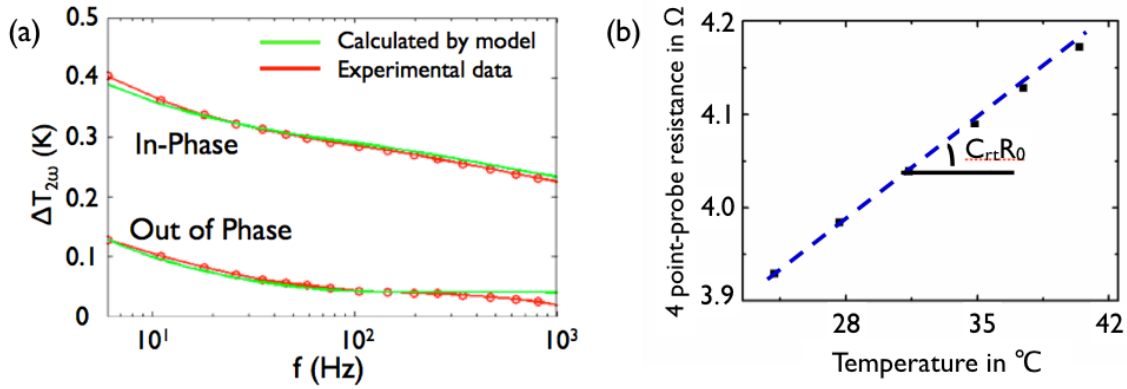

Figure 2.7: Data reduction of 3-ω thermal conductivity measurement of CuPc film on undoped Si. (a) In-phase and out-of-phase $T_{2\omega}$ calculated from **Eq 2.14** and measured by lock-in amplifier; the transformation of the measured voltage signal to the temperature signals follows **Eq 2.6** (b) Measurement of temperature coefficient of resistance. The four point-probe resistance of the wire changes linearly with the temperature near room temperature. (Figure adapted from *Jin et al.* (2011))

k_{th}.

In the measurements, the $V_{3\omega}$ is recorded by a lock-in amplifier; the resistance R_0 is measured using a multimeter; I_0 is the known and adjustable current source. C_{rt} value is obtained by measuring the wire resistance under a series of temperatures near the room temperature. **Figure 2.7** presents a typical fitting of k_{th} and an example of C_{rt} data reduction.

The experimental values of the thermal conductivity in following chapters are obtained by the 3-ω technique. Further discussion on measurements on conductive samples, such as organic/metal multilayers will be discussed in **Section** 3.6.

CHAPTER III

Thermal Boundary Conductance at Organic-Metal Interfaces

3.1 Introduction: a Significant Boundary Contribution

Research interest in the thermal properties of organics was discussed in **Ch. I**. With the ability to measure the thermal conductivity, k_{th} (See **Ch. II**), k_{th} values of several organic semiconductors in the thin-film phase were measured using the 3-ω method. *Jin et al.* (2011); *Kim et al.* (2005). The room temperature k_{th} of these materials are listed in **Table 3.1**.

Organic Semiconductor	k_{th} in $\text{W}\cdot\text{m}^{-1}\text{K}^{-1}$
CuPc	0.39
SubPc	0.11
C_{60}	0.13
Pentacene*	0.51
TPD*	0.24
Alq_3*	0.48

Table 3.1: Thermal conductivity of organic semiconductor thin film at room temperature. *Kim et al.* (2005)*, *Jin et al.* (2011) and unpublished data from Yansha Jin

Among these materials, Copper Phthalocyanine (CuPc), an archetypal organic semiconductor used in organic electronic devices, is also measured by TDTR techniques (See **Figure 2.5**). The reported value is slightly less than 3-ω. This slight

reduction is due to the interfacial thermal resistance at the film-substrate interface. Interfacial contribution to the thermal transport in nanostructures have proved to be significant and very useful in various of applications, such as data storage elements and thermal barrier coating (*Peng et al.* (1997); *Kim et al.* (2000)). Recently, ultralow thermal conductivity for the thermal barrier coating was achieved in metal/dielectric multilayer films because of the large interfacial thermal resistance. Likewise, thermal transport across dissimilar (i.e., organic/metal) interfaces can play a role in the understanding and the operation of organic optoelectronic devices, where organic/metal junction widely existed. While packaging often dominates heat dissipation in such devices, as mentioned in **Subsection 1.2.1**, the nanoscale heat transfer can be important in analyzing smaller features, such as hot spot, edges and tips. Moreover, the charge transport is closely related to thermal transport **Section 1.1**. Thus, exploring the interfacial thermal transport can be beneficial to the understanding of the charge injections from metal electrodes to organic active layers.

The next logical question to ask is "Is the interfacial resistance at organic/metal interfaces significant enough to make a difference?". and the answer is "Yes".

The thermal conductivities of three nanostructured films were measured. The first sample was a single CuPc film; the second sample was a co-deposited CuPc and Ag film with a 50% volume fraction of each; the third sample was an alternating multilayer structure consisting CuPc and Ag, with layer thickness, $t_{\mathrm{CuPc}} = t_{\mathrm{Ag}}$. Thus the volume fraction of Ag was also 50% in the third sample, same as the second sample.

k_{th} of the Vacuum Thermal Evaporated (VTE) CuPc film is 0.39 $\pm$ 0.04 W/mK and its surface morphology is shown in **Figure 3.1 (a)**. This Transmission Electron Microscopic (TEM) image was taken by JEOL 2010, imaging the CuPc film deposited on a copper TEM grid covered by holy carbon film.

Metals like silver are thermally conductive. k_{th} of silver is 439 W/mK, thus the

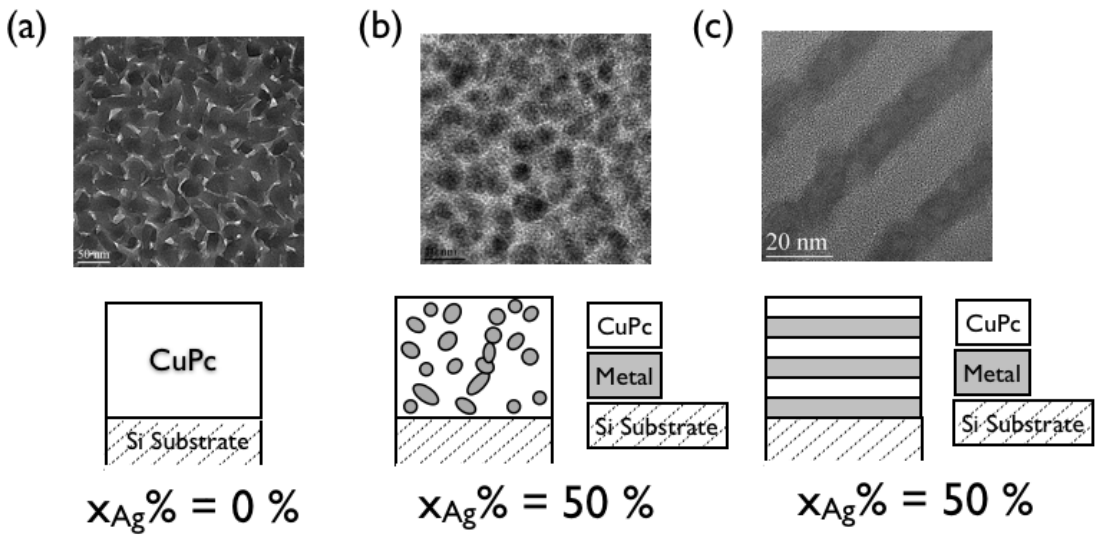

Figure 3.1: TEM images and schematic drawings of (a) Single layer of CuPc film on Si (b) Film of the mixture of CuPc and Ag on Si, with Ag volume fraction 50%; (c) Three-period multilayers of CuPc/Ag, with identical Ag and CuPc layer thickness, thus the silver volume fraction is also 50%). (Figure from Yansha Jin)

second sample, the mixture of Ag and CuPc, was measured to possess a k_{th} of 1.3 $\pm$ 0.28 W/mK by the 3-ω method. This structure was also deposited onto the TEM grid and imaged by TEM, see **Figure 3.1 (b)**. Silver formed nanoparticles that are dispersed in the CuPc matrix.

However, the alternating multilayers with the same Ag volume fraction didn't give the rise to k_{th}. Instead, a three-period CuPc/Ag multilayer structure with $t_{\text{CuPc}} = t_{\text{Ag}} = 10$ nm is measured to have $k_{\text{th}} = 0.19 \pm 0.03$ W/mK. Surprisingly, this value is significantly less than the thermal conductivity of the single CuPc films. Such multilayer systems containing interfaces between dissimilar materials exhibit lower thermal conductivity than their pure constituents, indicating the significance of the interfacial contribution to the thermal transport in nanoscale films.

The purpose of this chapter is to quantify the organic/metal interfacial contribution to the thermal transport, known as Thermal Boundary Conductance (TBC).

Several sets of controlled experiments were conducted on the alternating layered film structure in order to obtain the interfacial contribution.

3.2 Thermal Conductivity of Organic/Metal Multilayer

Effective thermal conductivity, k_{eff}, is measured for a number of multilayer samples in which the thickness of each CuPc/Ag period varies, while maintaining $t = t_{\text{CuPc}} = t_{\text{Ag}}$. **Figure 3.2** shows a data set obtained for a series of room temperature deposited, three-period CuPc/Ag multilayers with t varying from 6 to 20 nm. For individual layer thicknesses in excess of 8 nm (red regime in **Figure 3.2**), k_{eff} appears to scale inversely with the interface density, in agreement with prior results for inorganic systems (*Costescu et al.* (2004)). However, if the individual layer is thinner than 8 nm, k_{eff} sharply increases to 0.7 W/mK, which is attributed to the material mixing as evidenced by cross-sectional TEM (See **Figure 3.2**). This mixing likely enables a percolating path for heat through the high thermal conductivity silver regions.

Another evidence of the interfacial density and thermal conductivity relation is the unchanged k_{th} among the samples with the same interfacial density, see **Figure 3.3**. Individual layer thickness is identical ($t = 10$ nm) among the samples, while the number of layers varies. k_{eff} of these samples are within each other's error bar. This result supports the argument that the interfacial density change is the reason for the varying of k_{eff} in these multilayer structures.

To conclude, the interfaces between organic/metal introduces a thermal impedance that is not negligible for nanoscale film structure. These impedance will be quantified in the next section (**Section 3.3**).

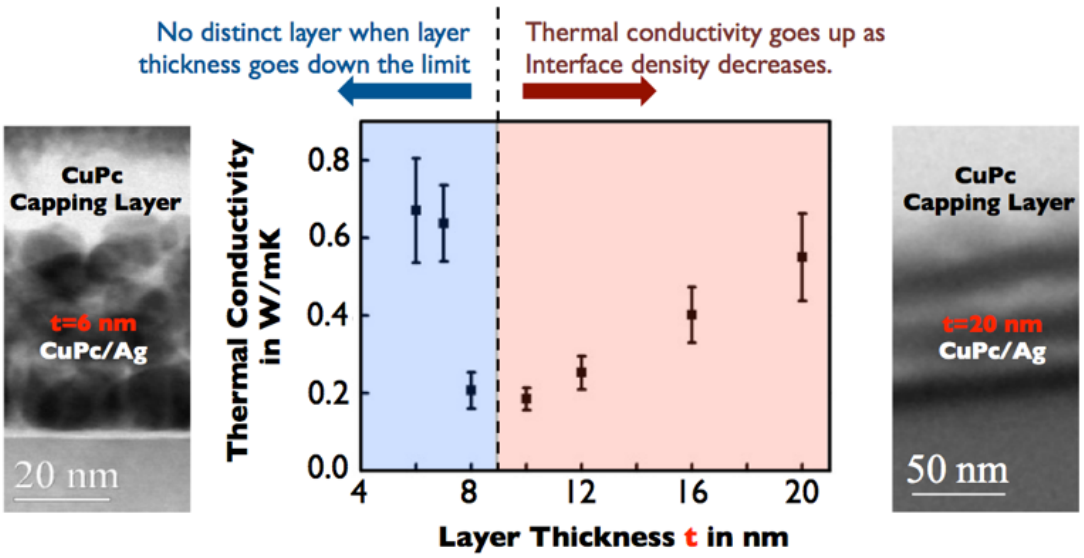

Figure 3.2: Thermal conductivity versus layer thickness of the three-period multilayers CuPc/Ag. Above 8 nm per layer, k_{th} increases with layer thickness while the volume fraction is kept the same, strongly suggesting the interfacial contribution to the thermal transport; Below 8 nm per layer, k_{th} rapidly increases with decreasing layer thickness due to the mixing of CuPc and Ag. No layered structure is observed for 6 nm per layer film, shown in the cross-sectional TEM image at left; while the right image shows a CuPc/Ag multilayer with 20 nm per layered with distinct interfaces between CuPc/Ag. (Figure adapted from *Jin et al.* (2011))

3.3 Thermal Boundary Conductance at Organic/Metal Interfaces

The impedance introduced by the interfaces leads to a temperature discontinuity ΔT in the presence of heat flux. The thermal boundary conductance (TBC) (*Kapitza* (1941); *Pollack* (1969)) is defined as

$$G_b = q/\Delta T \tag{3.1}$$

where ΔT is the temperature discontinuity and q (W/m^2) is the applied heat flux.

To extract the numerical value of the organic/metal thermal boundary conduc-

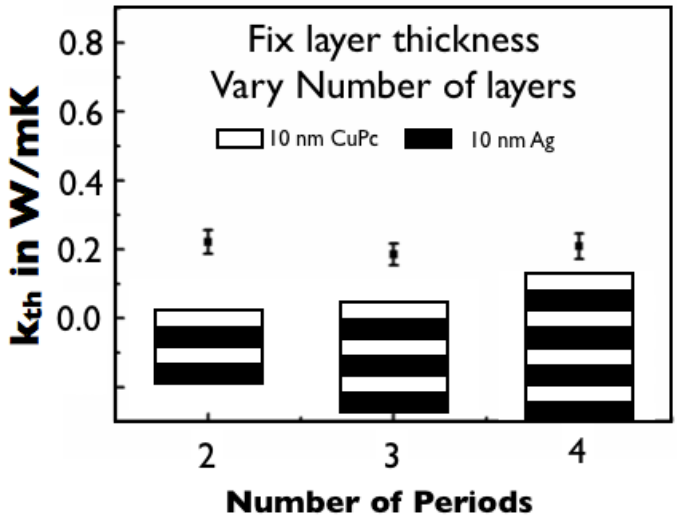

Figure 3.3: Thermal conductivity of CuPc/Ag multilayer versus number of layers while keeping the layer thickness constant. The thermal conductivity slightly fluctuates because the interface densities are the same among this series of samples. (Figure from Yansha Jin)

tance G_b, a series of thermal resistances corresponding to the organic film, metal film, and interface is presented:

$$\frac{Nt_{\mathrm{CuPc}}}{Ak_{\mathrm{th,CuPc}}} + \frac{Nt_{\mathrm{th,M}}}{Ak_{\mathrm{th,M}}} + \frac{n}{A_s G_b} + \frac{1}{AG_{\mathrm{bottom}}} = \frac{N(t_{\mathrm{CuPc}} + t_{\mathrm{M}})}{Ak_{\mathrm{eff}}} \tag{3.2}$$

where k_{eff} is the cross-sectional effective thermal conductivity of the whole multilayer structure, $k_{\mathrm{th,CuPc}}$ and $k_{\mathrm{th,M}}$ are the thermal conductivities of CuPc and the metal, t_{CuPc} and t_{M} are the layer thicknesses; G_b is the TBC of CuPc/metal interface and G_{bottom} is the TBC at the bottom metal/Si interface, n is the number of the CuPc/metal interfaces, N is the number of periods of the alternating multilayers, A is the cross-sectional area and A_s is the effective interface area measured by AFM. A quartz crystal microbalance monitor with a system error of approximately 2% was used during the deposition to keep the layers' equal $t = t_{\mathrm{CuPc}} = t_{\mathrm{M}}$; AFM measurements confirmed the film's Root Mean Square (RMS) roughness to be approximately 2$\sim$4 nm for a 15 nm thick film. For a three-period multilayer structure used in this

study, $n = 5$ and $N = 3$. Thus, **Eq 3.2** yields:

$$\frac{A}{A_s t} = 0.6 \cdot G_b\left(\frac{2}{k_{\text{eff}}} - \frac{1}{k_{\text{th,CuPc}}} - \frac{1}{k_{\text{th,M}}} - \frac{1}{3tG_{\text{bottom}}}\right) \tag{3.3}$$

A linear fit of the LHS versus the RHS of **Eq 3.3** was used to derive G_b: the TBC of CuPc/metal interfaces. Note that for the alternating layered systems, the phonon interference generally needs to be considered (*Hu et al.* (2010)). However, because the short phonon mean free path in CuPc films (1∼2 nm) is comparable to the RMS roughness of CuPc/metal interfaces and much smaller than the layer thickness (∼10 nm), the phonons are no longer coherent. This suggests that the phonon interference effects can be neglected in this study.

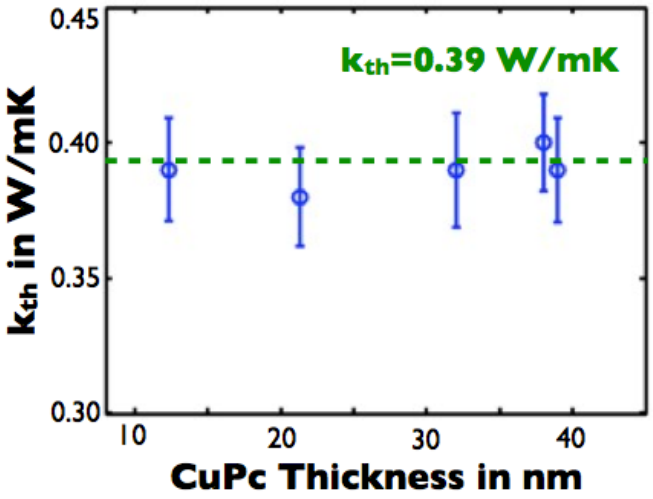

Figure 3.4: Thermal conductivity of CuPc thin film stays at 0.39 W/mK as film thickness increases from 10 to 40 nm. (Figure from *Jin et al.* (2012))

Because my approach relies on varying the individual layer thickness, it is important to understand whether the thermal conductivity of a given layer can change significantly with the variations in thickness. Experimental show that $k_{\text{th,CuPc}}$ does not vary appreciably (only about 5% fluctuation) for films ranging between 10∼40 nm in thickness (See **Figure 3.4**), and consequently, the error introduced by possible variations in $k_{\text{th,CuPc}}$ into the calculation of TBC is less than 5%. Moreover, $k_{\text{th,M}}$ is

1000 times larger than k_{th} for the organic films, thus a physically realistic variation in this term with thickness make little difference in the value of TBC extracted via **Eq 3.3**.

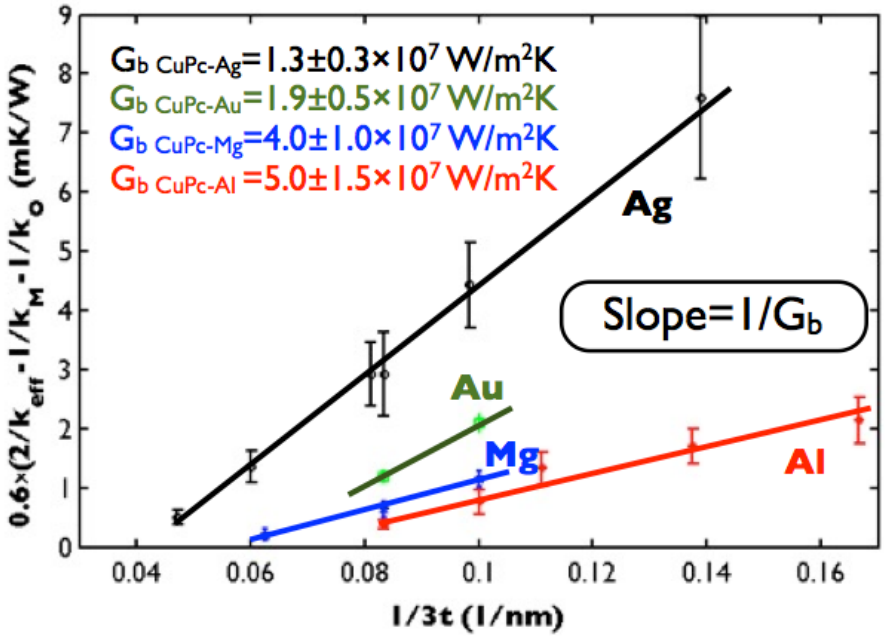

Figure 3.5: Thermal boundary conductance values of CuPc/metal interfaces. Using an equivalent circuit model for thermal conduction through the multilayer stack. TBC values are extracted from the slopes of the linear plot (the LHS and RHS of **Eq 3.3**). (Figure adapted from *Jin et al.* (2012))

Results of 3-ω measurements of thermal boundary conductance of CuPc/gold, CuPc/magnesium, CuPc/aluminum and CuPc/silver interfaces are presented. Using the modified Fourier's law (**Eq 3.3**) with TBC as the additional term, the slope of the linear fit of a series of samples with different interface densities is $1/G_b$ this specific material system. **Figure 3.5** shows the linear fits for all four CuPc/metal combinations; the TBC values for the different interfaces were calculated from these fits and listed in **Figure 3.5** as indicated.

These values are lower compared to other metal dielectric interfaces, whose TBC values are also listed in **Table 3.2** along with the TBC of CuPc/metal interfaces.

Materials System	G_b in $\mathrm{MW{\cdot}m^{-2}K^{-1}}$
CuPc : Ag	13 ± 3 †
CuPc : Al	50 ± 15 †
CuPc : Mg	40 ± 10 †
CuPc : Au	19 ± 5 †
Au : Si	145 ◇
Pt : Si	140 ◇
Cr : Si	180 ◇
Cr : sapphire	190 ◇
Cr : GaN	230 ◇
Cr : AlN	200 ◇
Al : Si	120 ◇
Al : sapphire	200, ◇ 105 *
Al : GaN	190 ◇
Al : AlN	230 ◇
Al : Si	120 ◇
Al : sapphire	200 ◇
Pb: sapphire	55 *
Au: sapphire	45 *

Table 3.2: Thermal boundary conductance of various of materials system. *Stevens et al.* (2005)◇, *Stoner and Maris* (1993)*, *Jin et al.* (2012)†

3.4 Effect of Morphology and Growth Conditions on Thermal Properties of Organic Thin Films

Growth conditions influence the thermal properties of the film and the interfaces. CuPc films were deposited onto Si substrates at different substrate temperature. Scanning Electron Microscopy (SEM) images show the surface morphology of these films (See **Figure 3.6**). Thermal conductivities, k_{th}, of the corresponding films are presented along with the SEM images, and a drop in k_{th} with decreasing deposition temperature is observed. Another interesting phenomenon observed was the cracking of the CuPc film below -60°C due to the large mismatch of the thermal expansion coefficient of the substrate and the CuPc film.

Beyond the critical temperature for film cracking, the low temperature deposition can create smoother films. AFM images revealed that films deposited at -60 °C are

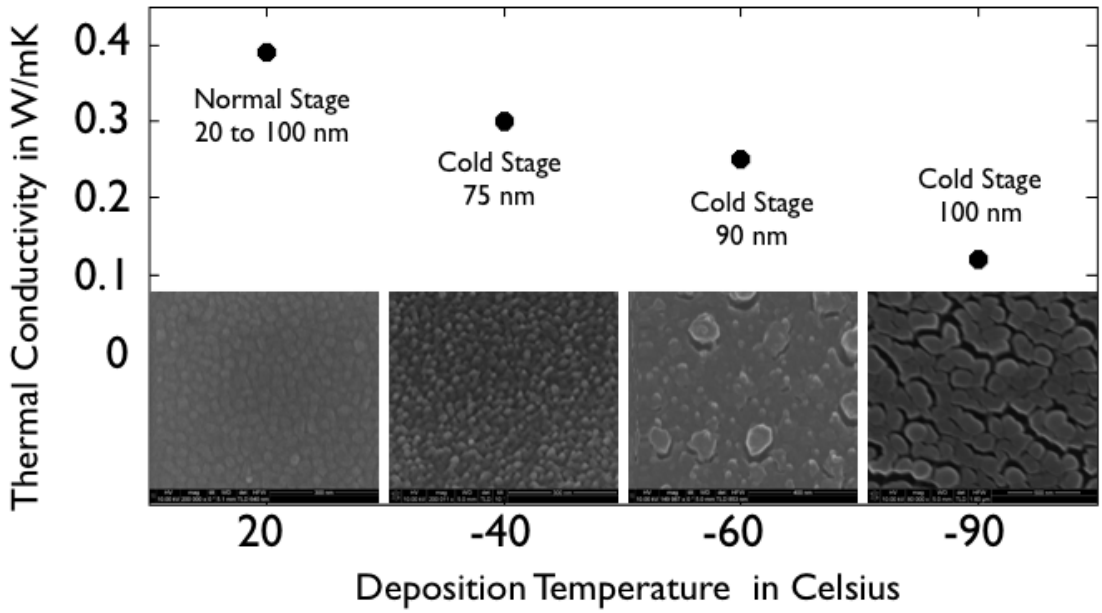

Figure 3.6: Thermal conductivities and the surface morphology of CuPc thin films on Si substrates, with the deposition temperature varying. (Figure from Yansha Jin)

smoother, with root-mean-square roughness values and grain sizes four times smaller than those of the RT-deposited films (See **Figure 3.7**). The influence on interface mixing on TBC can be further assessed by comparing the RT results to those for samples deposited onto colder substrates, since these latter samples have interfaces which are more distinct. As shown in **Figure 3.8**, we measure lower effective thermal conductivities for CuPc/Ag multilayers deposited at -60 °C than for pure CuPc films deposited at -60 °C (0.32 W/mK), implying that the TBR of CuPc/Ag interfaces remains a major contributor to the overall thermal resistance. Because the interfaces in the -60 °C samples are sharper than those in the 20 °C samples at the same layer thickness, the thermal conductivities of the former samples are generally lower than those of the latter samples. Similar trends in k_{eff} with layer thickness were observed for three-period CuPc/Al multilayers as shown in **Figure 3.8**.

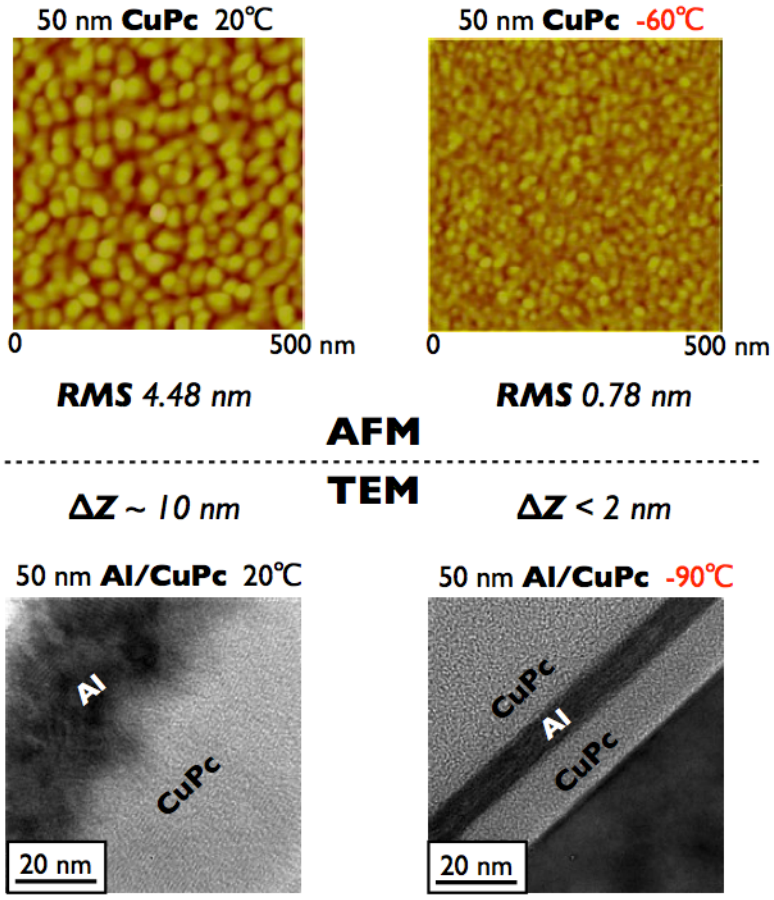

Figure 3.7: Surface and interface morphology of RT and CT CuPc and CuPc/Al thin films. Upper images are taken by AFM: 50 nm CuPc are deposited at 20 °C and -60 °C; the RMS roughnesses for RT deposited sample is 4.48 nm, and CT deposited sample is 0.78 nm; Bottom images are taken by TEM: these cross-sectional images of CuPc/Al layers show that RT deposited Al on CuPc has larger interfacial regime, ∼ 10 nm. (Figure from *Jin et al.* (2011))

3.5 Confirmation of Thermal Conductivity Measurements by Molecular Dynamics Simulations

Thermal conductivities of Room Temperature (RT) and Cryogenic Temperature (CT) deposited CuPc are verified by Molecular Dynamics Simulations (MDS) by my collaborator Chen Shao.*Shao et al.* (2013)

In recent years, Molecular Dynamics Simulations (MDS) have emerged as a powerful tool for calculating of thermal properties including organic involved systems. MD

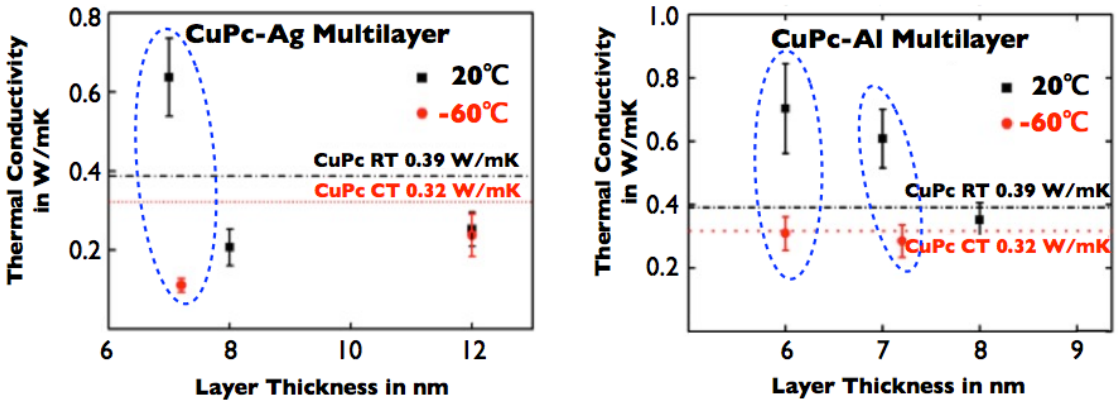

Figure 3.8: Lower thermal conductivity can be achieved by deposition onto cold substrates. Less interface roughness lead to thinner layered structure with lower k_{th}. (Left), Thermal conductivity of CuPc/Ag multilayers deposited at RT and CT; (Right), Thermal conductivity of CuPc/Al multilayers deposited at RT and CT. (Figure adapted from *Jin et al.* (2011))

simulation involving complicated organic molecules like CuPc, however, has seldom been reported before. Chen has built a force-field for CuPc solids and the thermal conductivity of the crystalline CuPc and the amorphous CuPc are calculated using the Green-Kubo formalism. Integral of heat flux autocorrelation represents the equilibrium process of MD simulation, see **Figure 3.9**. The converged values are the thermal conductivities of the corresponding simulation collections: k_{th} of amorphous CuPc is 0.32 W/mK; k_{th} of amorphous CuPc is 0.39 W/mK.

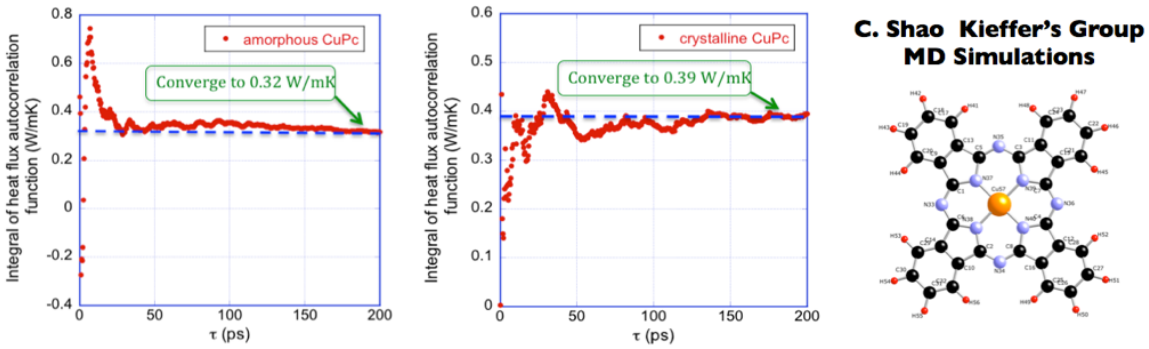

Figure 3.9: MDS on k_{th} of crystalline and amorphous CuPc films, along with a drawing of CuPc molecule. (Figure from *Shao et al.* (2013))

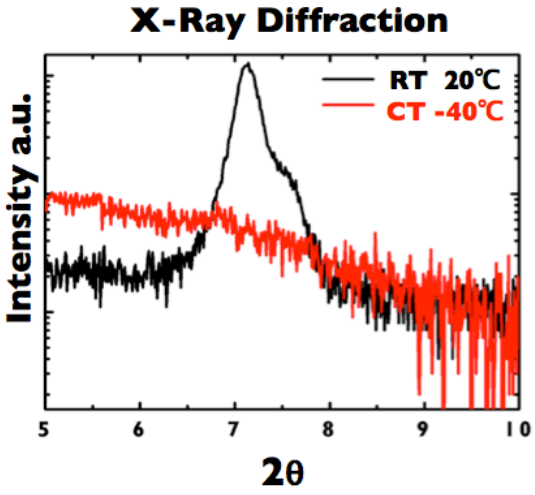

Figure 3.10: X-ray diffraction pattern of CuPc films deposited onto RT and CT Si substrates. RT deposited CuPc films show crystallinity and partial stacking order while the CT deposited ones are amorphous. (Figure from Yansha Jin)

The experimental values have been presented in **Section 3.4**. k_{th} of Room Temperature deposited CuPc (RT CuPc) was 0.39 ± 0.04 W/mK. k_{th} of CuPc deposited at -60 °C (CT CuPc) was 0.32 ± 0.04 W/mK. These samples' crystallinity was examined by X-ray Diffraction (XRD) was shown in **Figure 3.10**. (100) peaks was observed in RT CuPc, but CT CuPc below -40 °C appeared to be totally amorphous. Though the measurement and the MD simulation values seem to have a perfect agreement, the crystallinity level assumed in MD simulated crystalline film is much higher than the RT CuPc films. Thus, MD simulated k_{th} for RT CuPc in experiment should range from 0.32 to 0.39 W/mK. MD simulation and experiments are still in fairly good agreement.

3.6 Further Details on Experimental Methods

The interfaces investigated in the previous sections are CuPc and the common electrode materials, such as Ag and Al. The sample structure, illustrated in **Figure 3.11**, consists of alternating CuPc (99.9% pure) and metal (Al or Ag, 99.99% pure)

layers of identical thickness, deposited by vacuum thermal evaporation at 1 Å/s and 10^{-7} Torr onto 0.5 mm thick, [100] silicon substrates (resistivity $>$ 10 000 Ω cm). An electrically insulating 30 nm thick film of CuPc was deposited on top of the multilayer stack to eliminate parasitic cross-plane leakage current (*Koh et al.* (2009)), followed by a 50 μm wide wire of 40 nm nickel/400 nm silver. This top metal strip acts as both a heater and a thermometer, with heating accomplished by applying a low harmonic distortion current. Since the heater width is much greater than the multilayer thickness, the measurement is primarily sensitive to cross-plane rather than in-plane heat transfer. (*Borca-Tasciuc et al.* (2001))

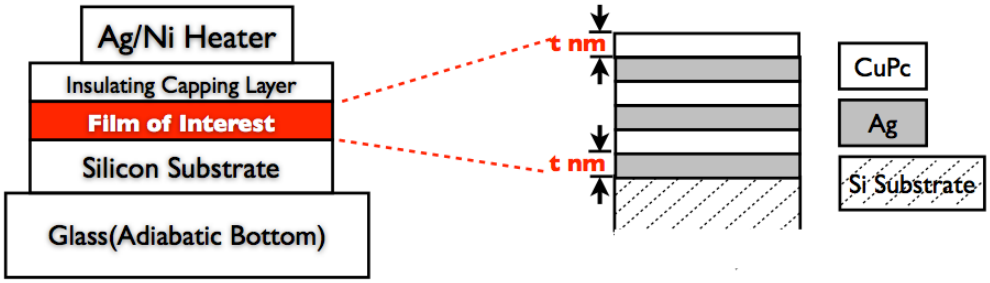

Figure 3.11: Schematic illustration (not scaled) of the 3-ω sample on glass slides. The multilayer CuPc/metal films request insulating capping layers to prevent parasitic current. (Figure from Yansha Jin)

Recall the requirements for 3-ω method in **Section 2.3** :

Firstly, $k_{\mathrm{th,s}} \ll k_{\mathrm{th,f}}$, substrate thermal conductivity has to be much larger than that of the film.

For the specific experiments in the previous section, the substrate used is Si whose $k_{\mathrm{th,s}}$ is 150 $\mathrm{W/m^{-1}K^{-1}}$. The films' thermal conductivity ranges from 0.2 $\sim$ 1 $\mathrm{W/m^{-1}K^{-1}}$, which satisfies $k_{\mathrm{th,s}} \ll k_{\mathrm{th,f}}$.

Secondly, for conductive samples, an insulating layer has to be inserted to prevent parasitic current. A 30 nm CuPc layer acts as an effective insulating layer for multilayer CuPc/Ag films. Proof is shown in **Figure 3.12**: the resistance between point A and B in is 3.2 Ω, while between point C and D is 4.5 MΩ. The resistance values

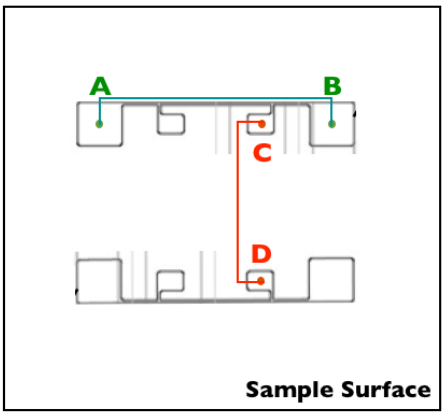

Figure 3.12: Illustration of parasitic current test probing points. Resistance between A and B is the the wire resistance, Resistance between C and D represents the resistance on the parasitic path. Figure from Yansha Jin

indicate the parasitic current is 10^6 times less than the applied current through the metal wire heater. The 3-ω measurements for the CuPc/metal multilayer systems is valid.

3.7 Summary

In summary, thermal conductivities of several organic semiconductors were reported in this Chapter. Multilayers of organics and metals can exhibit lower thermal conductivity than their pure constituents. The thermal conductivities of CuPc/Ag multilayers were found to decrease significantly with increasing interface density, indicating the presence of a low thermal boundary conductance. Thermal conductivity reached a minimum for a certain layer thickness, below which interface mixing caused it to increase. Deposition conditions affect the thermal conductivity of organic materials, such as CuPc. Lower temperature deposition makes amorphous organic thin films and the thermal conductivity is thus lower compared with room-temperature deposited films. Moreover, the values of the thermal conductivity of CuPc, both room temperature and cryogenic temperature deposited, are verified by molecular dynamics simulations.

CHAPTER IV

Boundary Effects on Thermal and Electrical Transport of Organic/Metal Nanocomposite

4.1 Introduction: Organic Thermoelectrics

Thermoelectric devices can be an effective in scavenging waste heat and generating electricity, for solid-state cooling, for temperature sensing and for other applications. Since the discovery of Bi_2Te_3 alloy's thermopower in 1960s, the ZT of inorganic materials have exceeded unity. (*Venkatasubramanian et al.* (2001); *Majumdar* (2004), see **Figure** 4.1). However, these materials are high cost and not environmental friendly. Unlike Bi_2Te_3 and its inorganic counterparts, the synthesis of organic materials is cheaper and less toxic, and offers other advantages, such as mechanical flexibility. However, in terms of the ZT, organic materials are still in deficiency. One of the best experimental demonstrations of ZT in organic semiconductors is the conducting polymer PEDOT-Tos with oxidation level of 23% with a reported ZT $\sim$0.25.(*Bubnova et al.* (2011), *Leclerc and Ahmed* (2011), *Kwok* (2012) see **Figure** 4.2) The bottleneck for increase ZT in bulk semiconductors is the conflicting traits that favors ZT (**Section** 1.3). Nanostructured materials, such as polymer nanocomposites, can lead to enhanced thermoelectric power factors ($S^2\sigma$).(*Zhang et al.* (2010); *Kim et al.* (2010); *See et al.* (2010)) In these cases, the electrical conductivities of the nanos-

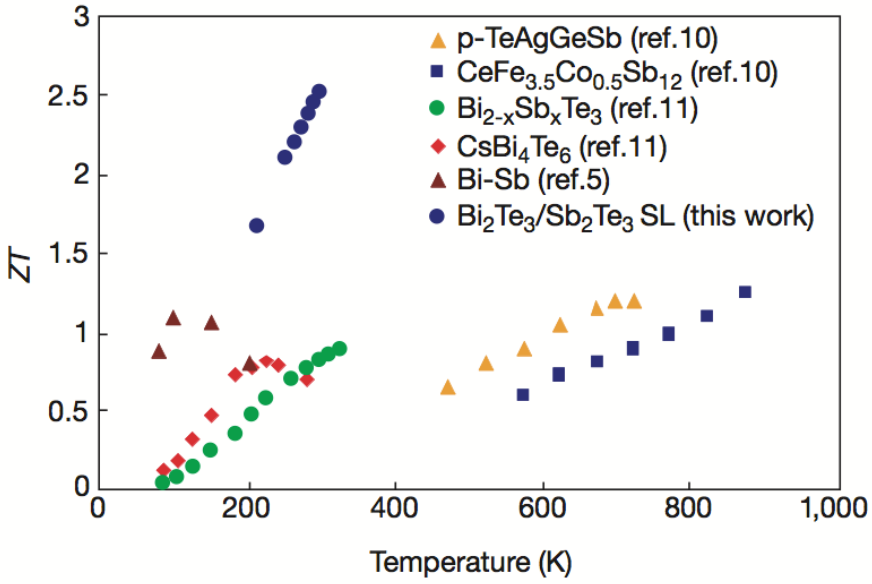

Figure 4.1: ZT's temperature dependence of inorganic thermoelectric materials. p-Bi_2Te_3 (10Å)/Sb_2Te_3 (50Å) superlattice owns the best ZT . Figure from *Venkatasubramanian et al.* (2001)

tructure were increased significantly without affecting the thermopower S. Though slightly increases in thermal conductivities were reported in some nanocomposites (*Zhang et al.* (2010)), the variation in thermal conductivities of these nanostructures were not discussed extensively, which will be addressed in this work. Inspired by the phonon blocking and electron transmitting superlattice such as Bi_2Te_3 alloy, I demonstrate the idea of using organic/metal nanocomposites with low thermal boundary resistance between the comprising materials. The measured thermal conductivity decreases with increasing volume fraction of the conductive fillers, while the FEM simulation shows an ZT enhancement 10 fold around the concentration that reaches the lowest thermal conductivity.(*Jin et al.* (2013)) It is anticipated that the combination of chemical modifications, power factor optimization and thermal boundary engineering can amount the maximum ZT of organics close to 1.

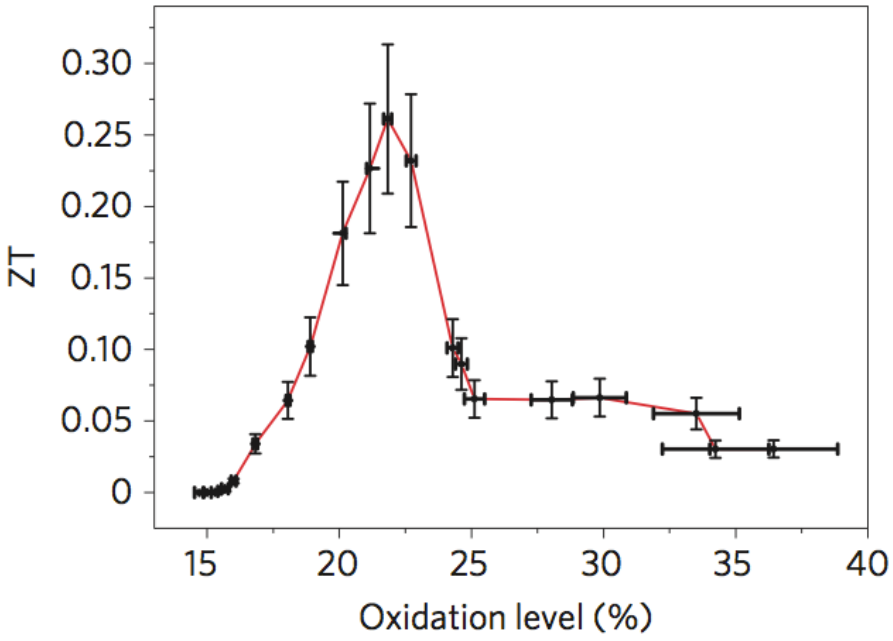

Figure 4.2: ZT optimization of PEDOT:Tos. By controlling the oxidation level of the polymer, the maximum $ZT = 0.25$ is reached. Figure from *Bubnova et al.* (2011)

4.2 Characterization of Co-Deposited Organic/Metal Films

The composites in this work were fabricated using vacuum thermal evaporation, and CuPc and Ag were co-deposited in the vacuum chamber. I first characterized these co-deposit films.

TEM images is shown in **Figure** 4.3, on samples with various of thickness, growth rate and filler concentrations. The images prove that co-deposition of CuPc and silver produced films of CuPc with dispersed Ag nanoparticles. The average radius of particle of shown in **Table** 4.1, ranging from 1.8 nm to 2.9 nm.

$x_{\mathbf{Ag}}$	**Thickness in nm**	**Nanoparticle radius in nm**
10%	50	1.9±0.2
10%	50	1.8±0.4
10%	150	2.2±0.8
20%	150	2.9±0.6

Table 4.1: *Jin et al.* (2013)

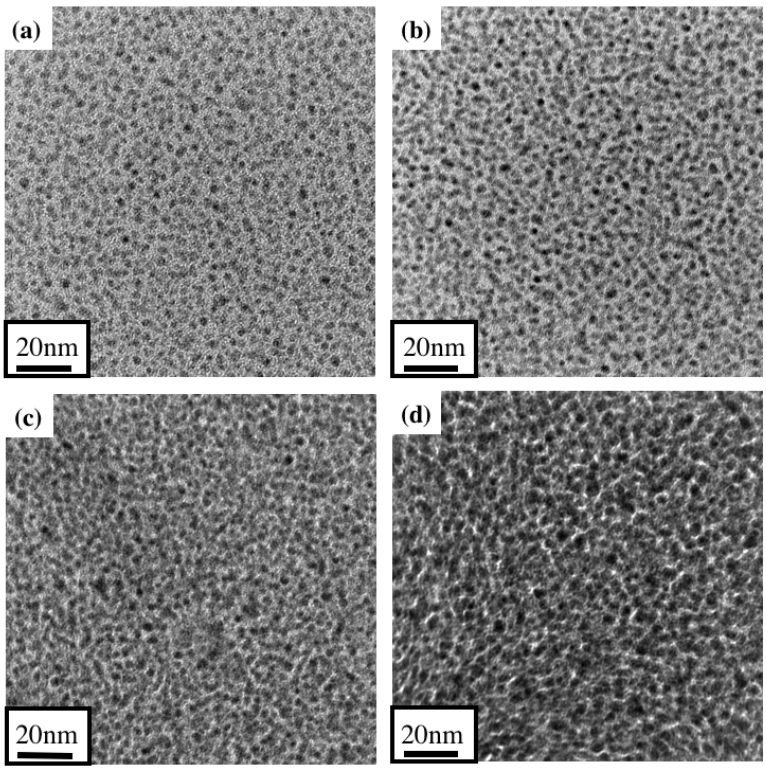

Figure 4.3: TEM images of CuPc/Ag nanocomposites with various thickness, silver concentrations and growth rates. (a) 50 nm $x_{\mathrm{Ag}} = 10\%$, growth rate $\sim$ 0.1 Å/s, particle radius 1.9 $\pm$ 0.2 nm; (b) 50 nm $x_{\mathrm{Ag}} = 10\%$, growth rate $\sim$ 0.5 Å/s, particle radius 1.8 $\pm$ 0.4 nm; (c) 150 nm $x_{\mathrm{Ag}} = 10\%$, growth rate $\sim$ 0.5 Å/s, particle radius 2.2 $\pm$ 0.8 nm; (d) 150 nm $x_{\mathrm{Ag}} = 20\%$, growth rate $\sim$ 0.5 Å/s, particle radius 2.9 $\pm$ 0.6 nm. Figure from *Jin et al.* (2013)

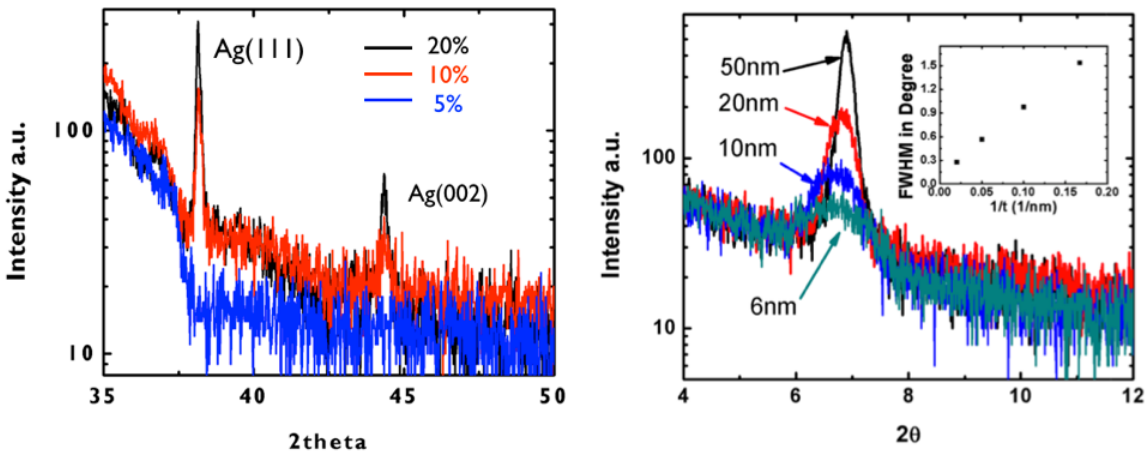

Figure 4.4: (Left) X-ray diffraction pattern of CuPc/Ag nanocomposites with different concentrations. Silver peaks (111) and (002) were observed. (Right) X-ray diffraction of single CuPc film with various of thickness. Full-Width Half Maximum (FWHM) is directly related to level of crystallinity. The inset indicates the crystallinity is proportional to the thickness. Figure from yansha.

The X-ray diffraction patterns of these samples are shown in **Figure** 4.4 (Left). Comparing to single CuPc films in **Figure** 4.4 (Right), the peak at 6 degree (CuPc (100)) was not observed in the mixed films; the only peak that can be seen is the silver (100). These suggested the short ranged order in organic matrix(CuPc) was broken by the filler (Ag), and Ag formed smaller crystalline particles inside the matrix.

4.3 Electrical/Thermal Conductivity of Organic/Metal Nanocomposites

The work in this section is collaborated with Sam Nola and the experimental data on electrical and thermal measurements was collected by her.

4.3.1 Electrical Conductivity: Percolation and Charge Trapping

Results from electrical measurement on organic-metal nanocomposite films are presented in **Figure 4.5**. The electrical conductivity (σ_e) showed a percolation-

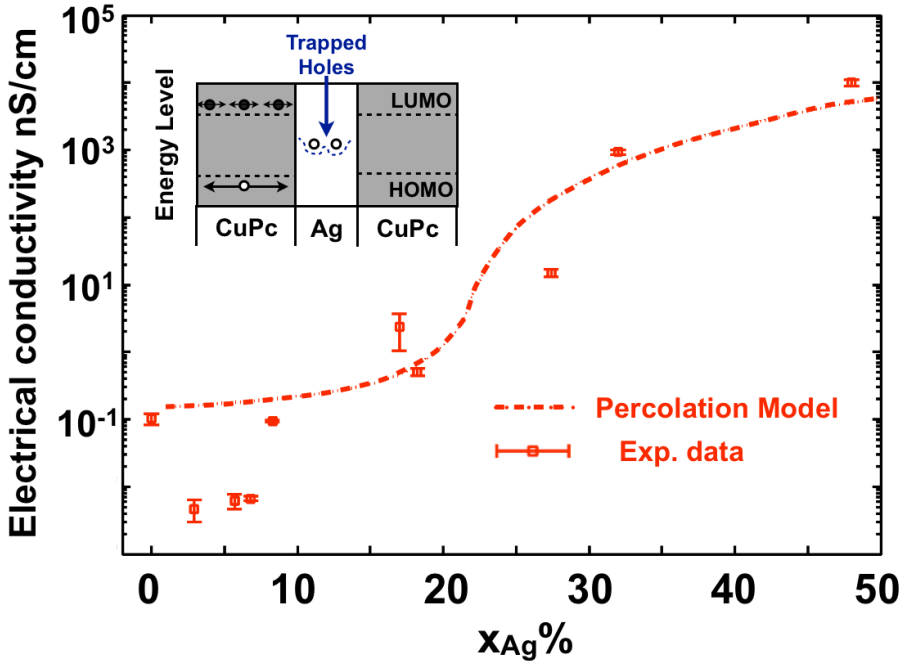

Figure 4.5: Electrical conductivity measurements on CuPc/Ag nanocomposites with various $x_{\mathrm{Ag}}\%$. Dotted line is the fitting from the percolation model. Figure from *Jin et al.* (2013)

like behavior above $x_{\mathrm{Ag}}\% = 10\%$, with critical fraction of silver by volume $x_{\mathrm{c,e}}\% = 20\%$. Also observed was an abrupt dip of σ_e in the ultra dilute regime ($x_{\mathrm{Ag}} \sim 5\%$). This is potentially due to the mismatch between organic and metal in charge carrier mobility and in Fermi levels. The work function of silver and the nature of metal/organic semiconductor interfaces is such that the injection barrier for holes, which have a comparatively high mobility in CuPc, is greater than the injection barrier for electrons, (*Kahn et al.* (2003); *Antohe et al.* (1991)) see inset of **Figure 4.5**. Isolated silver particles act as traps, and the barrier for re-injection would likely decrease electrical conductivity. Similar phenomena have been reported in pentacene films with gold nanoparticles embedded (*Tseng and Tao* (2009)), where the gold nanoparticles acted as a floating gate by trapping carrier charges.

In conclusion, the electrical conductivity follows the percolation trend in general, with abrupt dip at lower concentrations due to charge trapping.

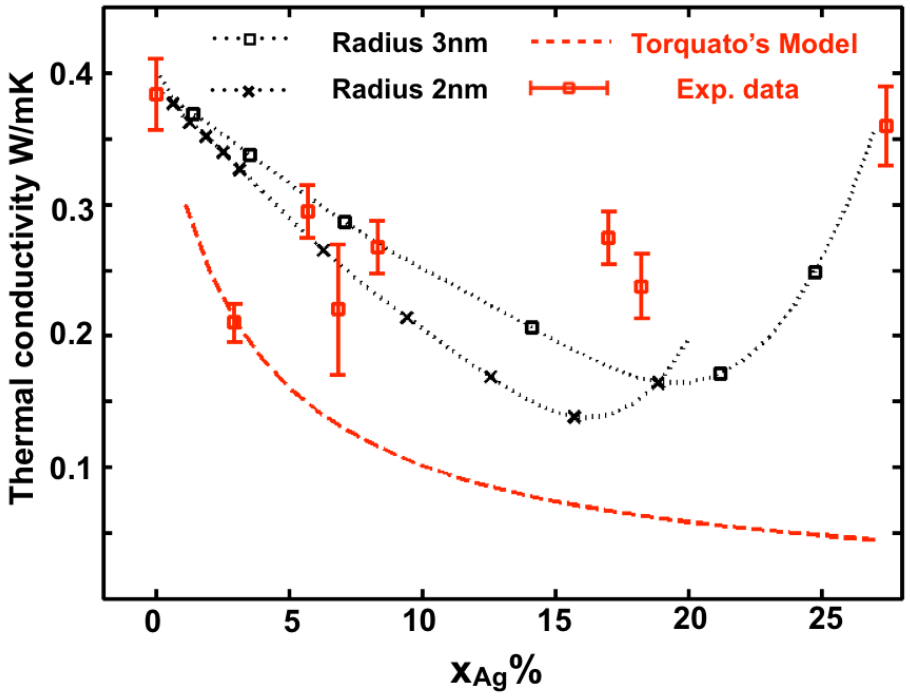

Figure 4.6: Thermal conductivities of CuPc/Ag nanocomposites with various $x_{\mathrm{Ag}}\%$ are plotted with error bars. The dashed line are the Hybrid model developed by Sam Nola (Macromolecular Engineering, University of Michigan, Ann Arbor). Figure from *Jin et al.* (2013)

4.3.2 Thermal Conductivity of Organic/Metal Nanocomposites

Both σ_e and k_{th} scale similarly with charge carrier concentration in most materials, however, in CuPc-Ag nanocomposites, they appeared to be decoupled in the dilute regime. No percolation threshold was observed for thermal conductivity (k_{th}) below $x_{\mathrm{Ag}}\% = 30\%$. Moreover, shown in **Figure 4.6**, k_{th} first decreased at low $x_{\mathrm{Ag}}\%$ and reached a minimum value before increasing again. Effective medium theory considering the boundary effects had predicted similar trend for general conductivity of composites. *Torquato and Rintoul* (1995) introduced a resistive interfacial media between the two phases and rigorously modeled the composites as a 3-phase system. The model suggested the initial drop in conductivity can only be achieved in systems with extra low thermal boundary conductance, of which CuPc-Ag nanocomposites happened to be an example. For thermal conductivity, a simplification of the Torquato

model can be written as

$$k_{\text{th}} = k_{\text{m}}[1 + x(1 - \alpha + 3R)/\alpha]^{-1} \tag{4.1}$$

where α is the conductivity ratio between filler and matrix $\alpha = k_{\text{CuPc}}/k_{\text{Ag}}$ and $R = k_{\text{CuPc}}/rG_b$ in which r is particle radius.

Figure 4.7 shows an illustration of 3rd phase modeling and Torquato's results following **Eq.** 4.1, it is clear that the model is only valid at the low concentration regime. The limitation is due to the assumption from *Torquato and Rintoul* (1995) that the particles are not overlapping with each other.

4.4 Finite Element Simulation on Transport Properties of Nanocomposites

To quantitatively evaluate the thermal conductivity k_{th} of organic/metal nanocomposite at the entire range of filler concentration, the corresponding 2D composite structure was generated and its thermal conductivity was solved using the finite element modeling package in `COMSOL MULTIPHYSICS` with `MATLAB v4.2`.

4.4.1 Conductivity Simulation Set-up

The simulation collection consists of a Copper Phthalocyanine (CuPc) matrix with randomly distributed Silver (Ag) particles confined in a 2D/3D box. A 2D example and the general principles of the simulation is shown in **Figure** 4.8. The Ag particles were assumed to be round(2D)/spherical(3D) with radius r and their coordinates are randomly generated by MATLAB. By varying the number of Ag particles N, the Ag volume fraction $x_{\text{Ag}}\%$ could be controlled. The thermal boundary conductance was introduced as a third phase by selecting the Thin Thermally Resistive Layer boundary condition in COMSOL. The layer thickness δ was set to be 1 nm: the experimentally

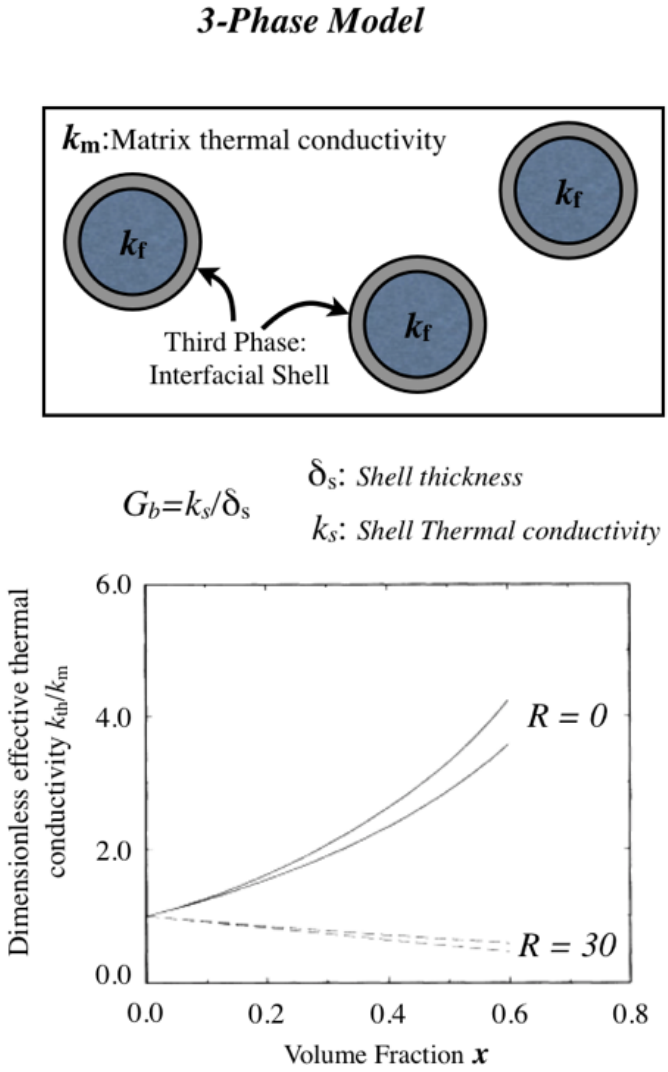

Figure 4.7: (Top) Illustration of Torquato model on conductivity of composites. A third-phase, interfacial shell is introduced, the shell's thermal conductivity is defined by TBC and the shell thickness, following the relation $k_s = G_b \delta_s$. (Bottom) Dimensionless effective thermal conductivity k_{th}/k_m versus the volume fraction of the filler. At high $R = 1/G_b$, thermal conductivity decreases with filler volume fraction. Bottom figure from *Torquato and Rintoul* (1995)

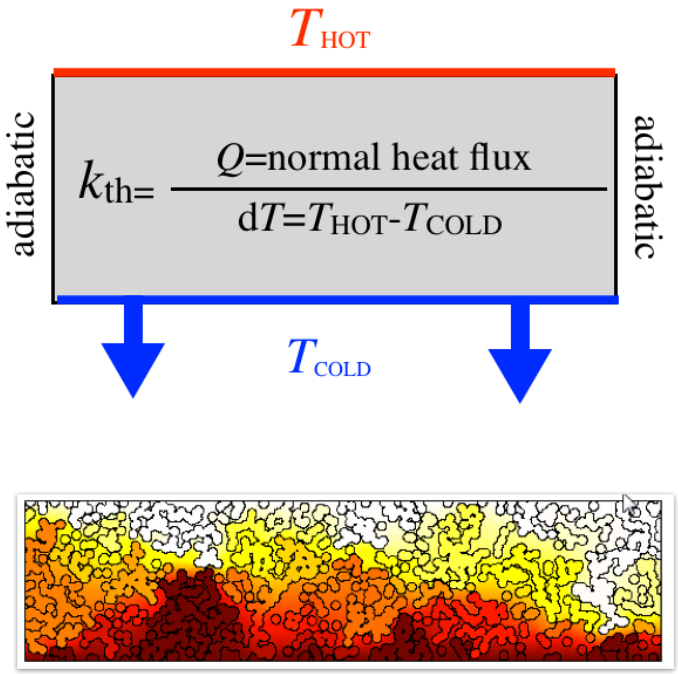

Figure 4.8: FEM of nanocomposites' thermal conductivity. (Top), General principle of thermal conductivity modeling: A temperature gradient of 0.2 K is set between the top and bottom boundaries; other sides are made to be adiabatic. Thermal conductivity equals the total normal heat flux(integrated heat flux from all nodes at the top boundary) over the temperature gradient. Figure from yansha.

measured RMS roughness of the CuPc/Ag interfaces in the composite; its thermal conductivity k^*_{th} was determined using equation

$$k^*_{\text{th}} = \delta \cdot G_b \tag{4.2}$$

where G_b is the thermal boundary conductance of CuPc/Ag interfaces, which was found to be 13 MW/m^{2}K. By applying a temperature difference ΔT between the top and bottom surfaces of the box and setting all other surfaces as adiabatic, the thermal conductivity of the composite can be obtained by the relation **Eq.** 2.1, where q is the heat flux integrated over all nodes at the top surface. ΔT is selected to be 0.2 K and the distance between the top and bottom surfaces is chosen as 100 nm, matching to the temperature change in 3ω measurements which ranges from 0.05 K to 0.25 K and the thickness of the multilayer structure tested that is 80 nm to 120 nm.

4.4.2 Pseudo-3D Simulation

The simulation results used to compare with experiment are "pseudo 3D", calculated from the 2D results following the equation:

$$k_{\text{th,3D}} = k_{\text{CuPc}} - \frac{A_{\text{s,3D}}}{A_{\text{s,2D}}}(k_{\text{CuPc}} - k_{\text{th,2D}}) \tag{4.3}$$

where A_{s} represents the surface area. With the constraints that the concentration $x_{\text{Ag}}\%$ is identical in both 2D and 3D cases

$$x_{\text{Ag}}\% = \frac{N_{\text{3D}} \cdot \frac{4}{3}\pi a^3}{V} = \frac{N_{\text{2D}} \cdot \pi a^2}{A} \tag{4.4}$$

the pre-factor in 4.3 can be expressed as

$$\frac{A_{\text{s,3D}}}{A_{\text{s,2D}}} = \frac{N_{\text{3D}}/V}{N_{\text{2D}}/A} \cdot \frac{4\pi a^2}{2\pi a} = 1.5 \tag{4.5}$$

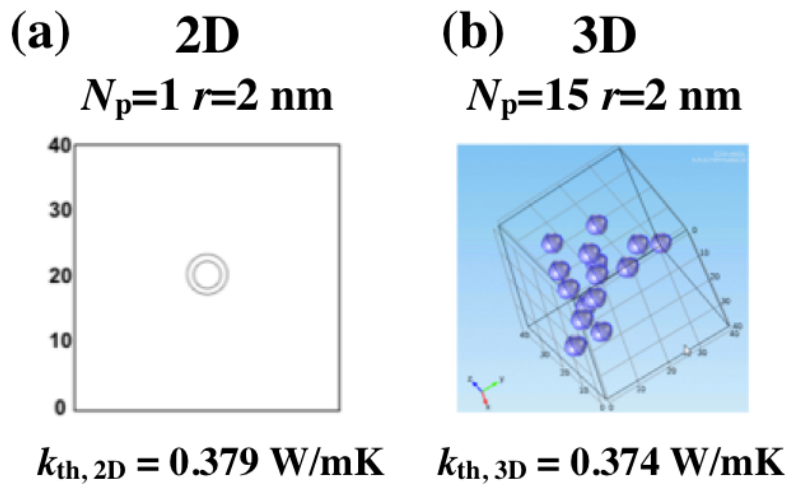

Figure 4.9: 2D and 3D FEM simulation at sam silver concentration in ultra dilute regime ($x_{\mathrm{Ag}} = 0.8\%$). Thermal conductivity value from FEM for 2D and 3D agree well with the "pseudo 3-D" extrapolation, **Eq.** 4.5. Figure from *Jin et al.* (2013).

The reason for doing "pseudo 3D" other than real 3D is the the complexity of geometry grows tremendously from 2D to 3D under same silver volume concentrations. The more than ten thousand of pieces are needed to be united and defined as resistive boundaries which increase the manual setting-time and calculation time.

The "pseudo 3D" k_{th} is within 10% margin of error compared to real 3D FEM simulation at low concentrations, proved by low concentration "real" 3D FEM simulations. FEM simulation set-up is illustrated in **Figure** 4.9. The 2D simulation output of COMSOL is shown in **Figure** 4.9 (a), with randomized particle coordinate within the 2D simulation box. In **Figure** 4.9 (b). The 2D and 3D simulation shares a same silver volume fraction at ultra dilute regime $x_{\mathrm{Ag}}\% = 0.8\%$, the thermal conductivity is simulated to be $k_{\mathrm{th,2D}} = 0.3789$ W/mK. Following **Eq.** 4.3, $k_{\mathrm{th,3D}} = 0.3734$ W/mK, the pre-factor $A_{\mathrm{3D}}/A_{\mathrm{s,2D}}$ is 1.43, within 5% error compared with our calculated value.

The degree of accuracy in the "pseudo" 3D calculations enabled us to use the approximation to compare with experimental data and conduct multi-parameter analysis in the following sections.

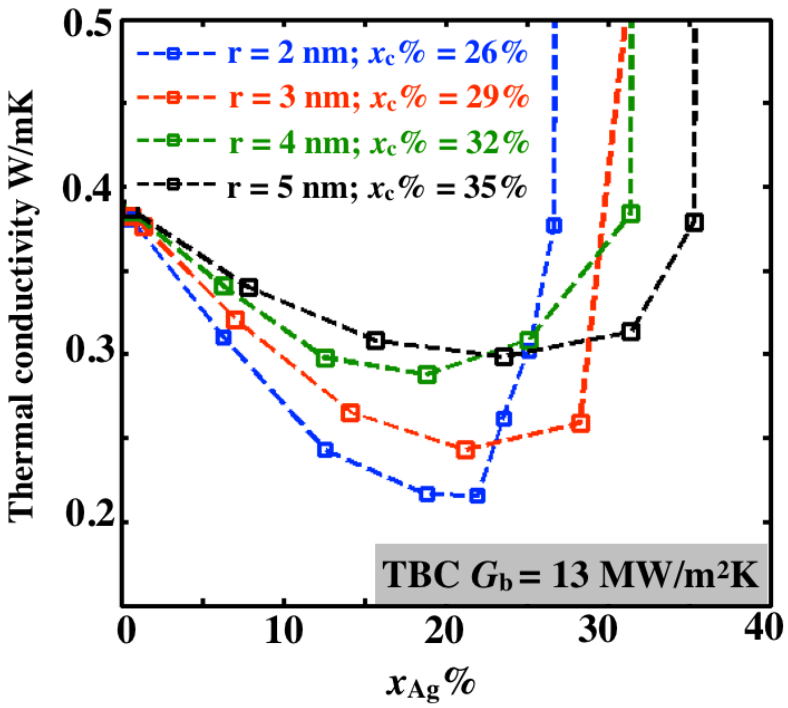

Figure 4.10: The particle size effect on k_{th} of CuPc/Ag nanocomposites. FEM results for composites with radius of 2 nm, 3nm, 4 nm and 5 nm. The interfacial area increases with the smaller particle sizes at the same $x_{\text{Ag}}\%$, thus the thermal conductivity drops with the decreasing particle size. The percolation threshold for the corresponding particle sizes are listed, which increases with the particle sizes. Figure from *Jin et al.* (2013)

4.4.3 Tunable parameter I: Particle Size

Curves of thermal conductivity of the CuPc-Ag nanocomposites with different particle radii were plotted against $x_{\text{Ag}}\%$. Percolation threshold increases with the silver particle radius as listed in **Figure** 4.10. Statistically it is easier for smaller particles to form percolation path at the same filler volume fraction. Before the percolation threshold, however, a reduction of k_{th} is observed at lower concentrations (**Figure** 4.10). This trend is attribute to the boundary effect: under the same silver concentrations, the interfacial area also changes with silver particle size. This reasoning is similar to our discussion for the difference between 2D and 3D.

This strong influence of particle size on nanocomposites' thermal conductivity re-

quest us to use the accurate particle radii comparing to the experiment. In terms of tuning thermoelectric properties, the particle radius is one of the tunable parameters. For particles smaller than 1 nm diameter, which is the phonon mean free path of CuPc matrix, quantum effects and ballistic transport might interfere with the continue decreasing trend of k_{th} with the particle radius. However, for CuPc-Ag nanocomposites, the particle radius larger than 4 nm diameter and our current results hold.

4.4.4 Tunable parameter II: Thermal Boundary Conductance

Another tunable parameter for the thermoelectric properties in nanocomposites are the thermal boundary conductance G_b. Thermal conductivity is calculated with different G_b at a fixed particle radius. The particle radius is set at 5 nm for the thermal conductivity plots **Figure** 4.11. k_{th} is found to be increasing monotonically with $x_{\text{Ag}}\%$ without the boundary effect, which is presented by the perfect(∞) interfacial conductance. As the interfacial conductance decreases, k_{th} starts to drop at first then rises up at higher concentrations, which matches the experimental trend of k_{th} discussed in **Section** 4.3.2, which proved adding the thermal boundary conductance is the reason for the drop of k_{th}.

In addition of supporting the boundary effect on thermal conductivity of composites, the simulation results also suggesting another interesting fact: the $x_{\text{Ag}}\%$ for the minimum k_{th} also changes with G_b. As shown in **Figure** 4.11 and replotted in the inset **Figure** 4.11, the lower the thermal boundary conductance, the higher the $x_{\text{Ag}}\%(\text{min})$. This piece of information on where k_{th} the minimizes is very important in optimizing thermoelectric efficiency.

4.4.5 Proof of Validity of the FEM simulation

Recall that the advantages of FEM simulation over the analytical Torquato model is that FEM can predict in the entire range of silver concentrations and the "pseudo

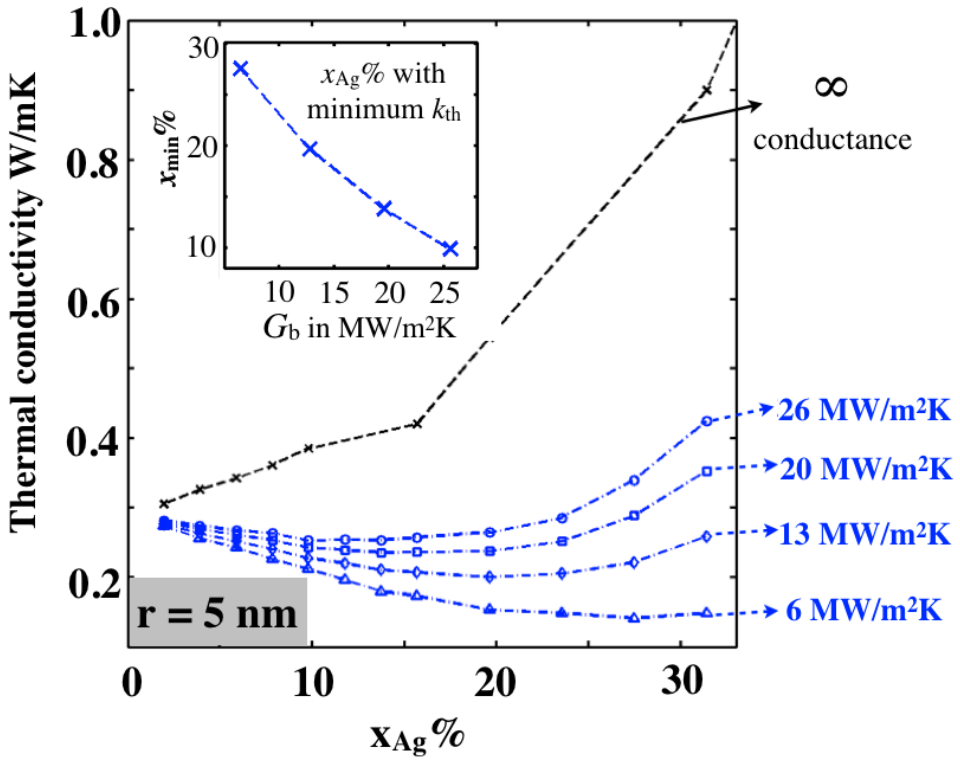

Figure 4.11: Boundary effect on k_{th} of CuPc/Ag nanocomposites. FEM results for composites with various values of thermal boundary conductance (G_b). Smaller G_b yields to smaller k_{th}. The $x_{\text{Ag}}\%$ that reaches the minimum thermal conductivity also changes G_b. The inset shows this critical concentration for each TBC values. Figure from *Jin et al.* (2013)

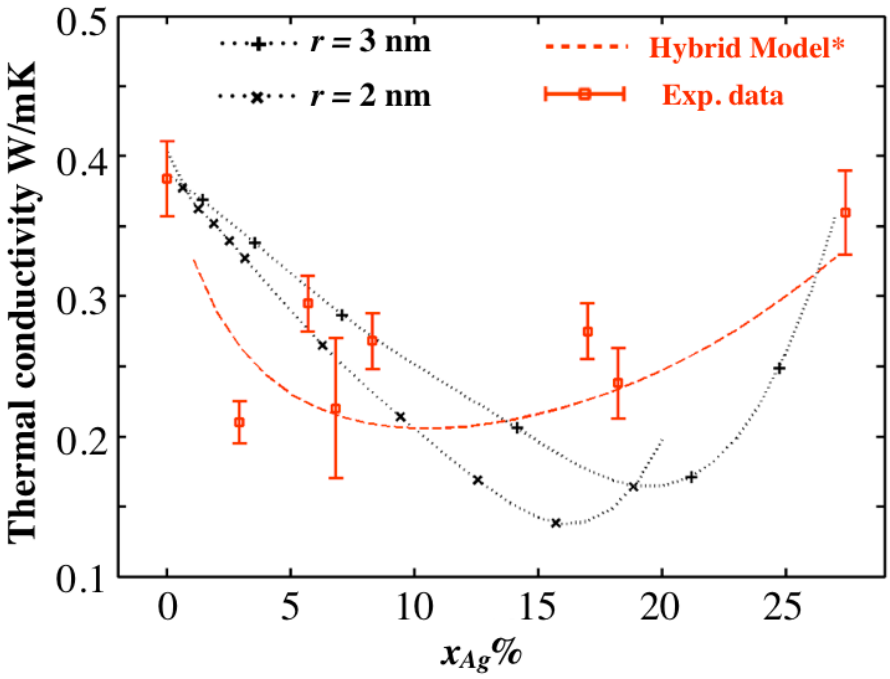

Figure 4.12: Thermal conductivity measurements on nanocomposites with various filler concentrations are plotted with error bars. Red dashed line is calculated by Hybrid model (Sam Nola). Black dotted lines are FEM results corresponded to 2 nm and 3 nm Ag particle radii, respectively. Figure adapted from *Jin et al.* (2013).

3D" results extracted from 2D simulation is enough accurate to compare to the measurements. The simulations adopted the measured particle radius 2 nm to 3 nm (in **Table** 4.1) and the measured TBC in **Table** 3.2 for CuPc/Ag nanocomposites in order to seek better agreement with the experiment.

Thermal conductivities calculated from FEM simulations with 2 nm and 3 nm radius are plotted in **Figure** 4.12 along with the experimental value. As can be seen, most of the measured data points lie within the range of the 2 nm and 3 nm simulation curves. Note the hybrid model presented in the **Figure** 4.12 was developed by Sam Nola, combining some of the existing models, the hybrid model is discussed in *Jin et al.* (2013).

The agreement between experiment and modeling data strongly proves the validity of the FEM simulations and further in this chapter, a novel way to optimize

thermoelectric efficiency for organic/inorganic hybrids is presented based on the FEM simulations.

4.4.6 TE Figure of Merit Enhancement

The thermoelectric Figure of merit (ZT) (**Eq.** 1.31) can represent the efficiency of TE devices, and lowering thermal conductivity, enhancing electrical conduction can optimize ZT.

Electrical conductivities are modeled in the same set of structures, while electrical and thermal conduction can be decoupled in composites, if electrical conduction is not hindered by the boundary phase, and particularly if σ_e increases with filler concentration, as shown in **Figure 4.13**. The Seebeck coefficient values are approximated from the simulated σ_e following the linear relationship between S and $\ln(\sigma_e)$(*Kim et al.* (2011); *Yu et al.* (2011)) in moderately doped organic semiconductor system, plotted in **Figure 4.13**.

$$S = -\frac{k_B}{q} \ln \sigma_e + C_1 \tag{4.6}$$

where C_1 is related to carrier mobility and density of states and we assume to be a constant in our study.

A multi-parameter contour plot of ZT versus particle radius, r, and filler concentration, $x_{\mathrm{f}}\%$ is shown in **Figure 4.14**, based on the well-characterized system of CuPc - silver nanocomposites (*Jin et al.* (2011, 2012)). TBC is a constant in the plot, which is 13 $\mathrm{MW/m^2K}$ – the G_b for CuPc-Ag interfaces. The contours are normalized to the ZT of CuPc, and a maximum ZT enhancement factor of 5 is achieved relative to bulk CuPc. Another finding that can guide the design of TE materials is the optimized filler concentration for filler particles of different sizes. The optimized filler concentration ranges from 20% to 30% as the filler particle size grows.

With the optimized percentages extrapolated from a set of contour plots with different G_b, the maximum enhancement is calculated using two parameters: Thermal

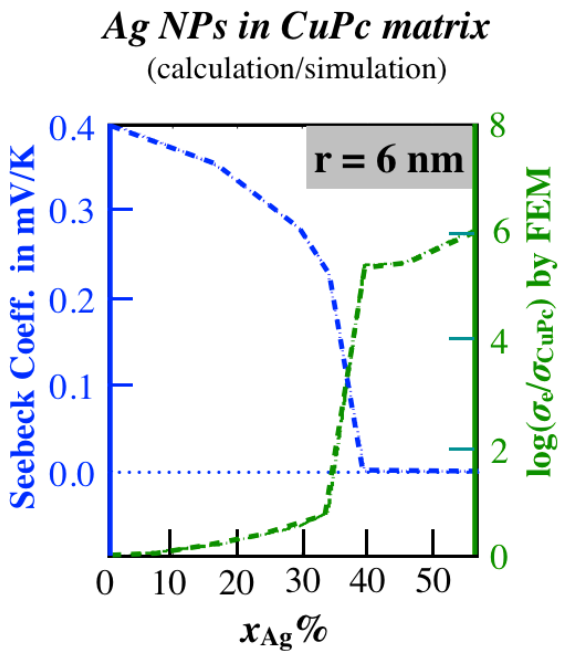

Figure 4.13: FEM calculated electrical conductivity and the Seebeck coefficient extracted from the linear relation between S and $\ln(\sigma_e)$*Jin et al.* (2013)

boundary conductance G_b (ranges from 10 to 30 MW/m^{2}K), and the radius of the filler particles r, (ranging from 2 to 6 nm), shown in **Figure 4.15**. Previous work showed that G_b at organic-metal interface originates from phonon-phonon scattering, due to the fact that electron-phonon contribution to the boundary resistance is negligible compared to phonon-phonon scattering (*Majumdar and Reddy* (2004)). In weakly-bonded organic-inorganic hybrids(*Jin et al.* (2012)), TBC is mainly affected by the interfacial bonding strength. There are also reports suggesting that the interfacial bonding strength could be adjusted by surface modifications, like changing the side group of a self-assembled monolayer coating (*Losego et al.* (2012)). Further decrease in filler particle radius might introduce complications, such as quantum confinement and ballistic transport. Even with these concerns, the simulation is reliable down to $r = 2$ nm, because the filler particle size is still larger than the phonon mean free path of most organic materials.(*Huang et al.* (2007); *Sun et al.* (2013)) The temperature gradient within the higher conducting filler particle is minor influence.

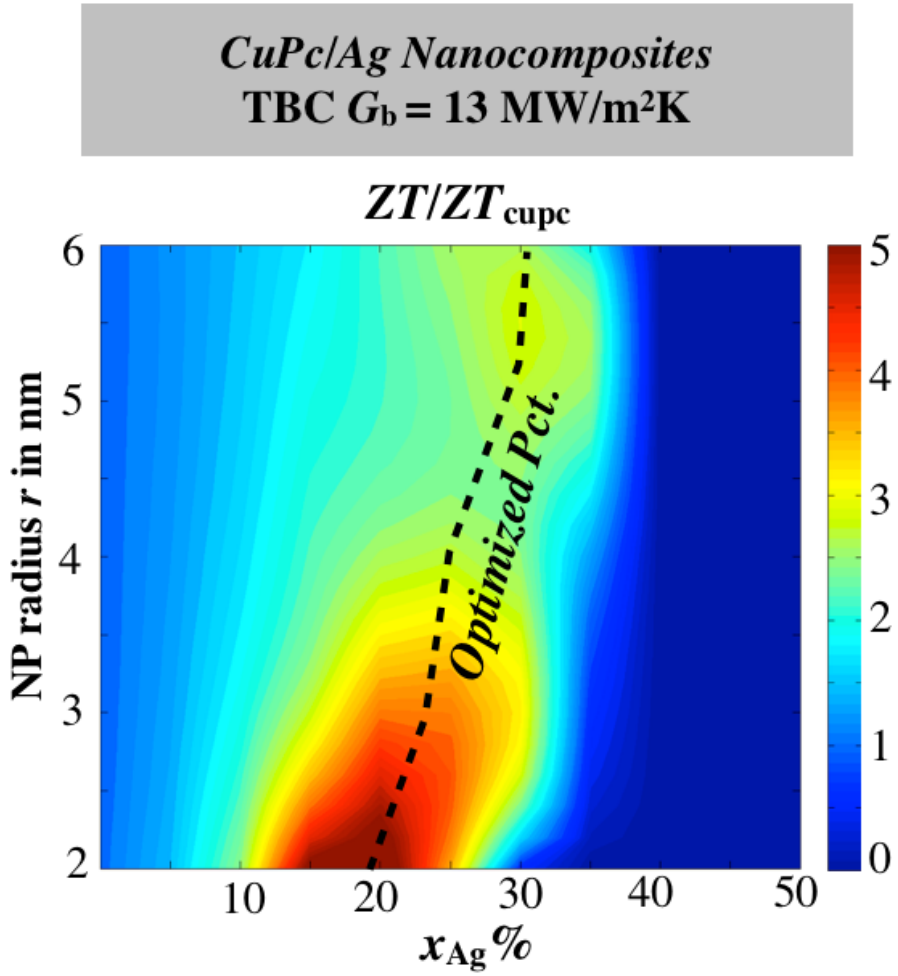

Figure 4.14: Multi-parameter optimization of ZT of CuPc-Ag nanocomposites (G_b = 13 MW/m^{2}K). The volume fraction of the filler ranges from 0 % to 50 % and particle radii from 2 to 6 nm. The optimum x_{Ag}% for different particle radii is indicated as the dashed black line. The enhancement of ZT is as large as 5 times. Figure from *Jin et al.* (2013).

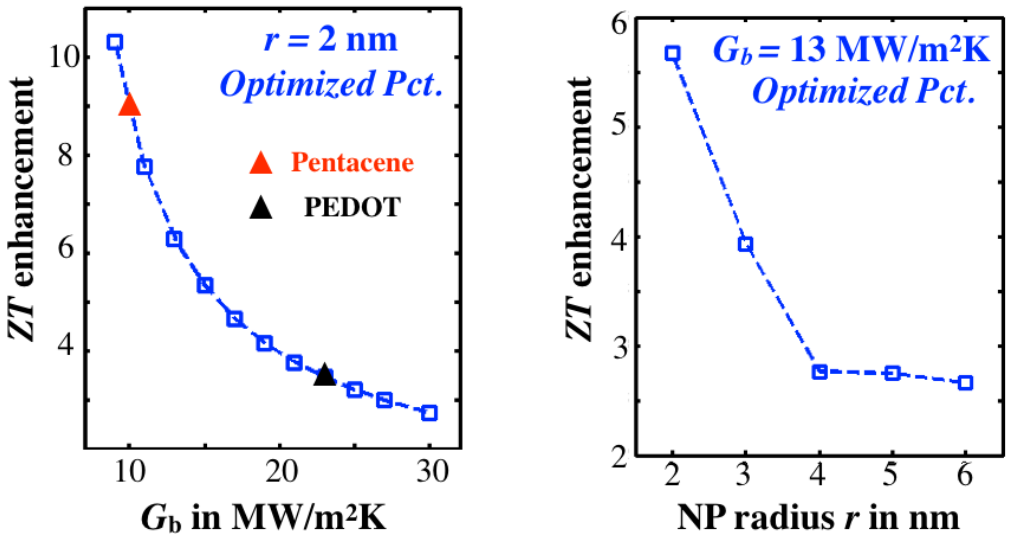

Figure 4.15: ZT enhancement at optimized filler percentage. (a) Maximum ZT enhancement with G_b varying from 10 to 30 MW/m^{2}K. Smaller G_b is desired, and conducting polymer potentially have a 3-time boost in ZT. (b) Maximum ZT enhancement with the particle radii varying from 2 nm to 6 nm. The radius range is above organic materials' phonon mean free path. Figure from *Jin et al.* (2013).

Figure 4.15 shows that smaller NPs and lower G_b improve thermoelectric performance for organic/inorganic hybrids: compared to the single-phase organic semiconductor, enhancement of ZT can be as high as 10-fold. However, because organic semiconductors suffer from intrinsically low electrical conductivity, it is necessary to combine the boundary effects with molecular design and chemical doping to further boost ZT. Additional experiments are needed for combining these optimizing mechanisms, but the perspective emerging from this study is promising. Based on the TBC reported for the polymers (*Losego et al.* (2012); *Li et al.* (2009); *Hsieh et al.* (2011); *Duong et al.* (2008)), the maximum enhancement expected from the factors discussed here is $3 \sim 4$ times (see **Figure 4.15** (a)) that of the recently reported $ZT = 0.25$,(*Bubnova et al.* (2011)) potentially pushing ZT of organic-inorganic nanocomposite to unity.

4.5 Potential Optimization of ZT for Organic Semiconductors

The FEM simulation suggested that smaller NPs and lower thermal boundary conductance G_b is needed to achieve better a thermoelectric performance for organic/inorganic hybrids. Enhancement compared to the pure organic semiconductor can reach as high as 10 times. However, organic semiconductor intrinsically suffers from low electrical conductivity, it is necessary to combine the molecule structure modifications and the boundary effects to achieve greater boost in ZT.

Discussed in *Bubnova et al.* (2011), the replacing of the PSS in poly(3,4-ethylenedioxythiophene) poly(styrenesulfonate) (PEDOT:PSS) by small anions, for example Tos, increases σ_e for several orders of magnitude but the Seebeck coefficient remains competitive. Additional experiments are needed for compiling this mechanism with boundary effects from the fillers, but the perspective is promising: for the conductive polymers like PEDOT, the lowest G_b reported are around 20 MW/m^{2}K. Thus, the maximum enhancement is 3$\times$ the current reported $ZT = 0.25$ which makes the ZT of organic close to unity.

4.6 Summary

In organic semiconductors the Wiedemann-Franz law is often violated, potentially enabling independent control over electrical and thermal conductivity, as observed here with the organic-metal nanocomposites. This effect is attributed to the interface between metal particles and organic matrix materials impeding thermal transport. Thermal conductivity (k_{th}) can be decoupled from electrical conductivity (σ_e) in the composite of an archetypal organic semiconductor (Copper Phthalocyanine, CuPc) and silver, with thermal boundary conductance as low as 13 MW/m^{2}K at the interface. We show that k_{th} decreases with volume fraction occupied by silver

nanoparticles ($x_{\mathrm{Ag}}\%$) in the dilute limit, reaching a minimum value concentration, $x_{\mathrm{Ag}}\%(\mathrm{min})= 18\%$, while σ_e exceeds that of the pure organic semiconductor. Further modeling indicates that ZT values of organic-inorganic nanocomposites can be potentially enhanced 10 fold around $x_{\mathrm{f}}\%(\mathrm{min})$, compared to ZT of the pure compounds. These findings suggest a novel pathway for the future design of organic thermoelectric materials.

Introducing conductive filler particles into an organic matrix can achieve the goal of $ZT > 1$ by virtue of boundary effects, which were quantitatively measured (*Jin et al.* (2012)). A novel design principle emerges for tuning the overall TE behavior of nanocomposites, demonstrated in simulations and validated by experiments for composites comprising copper phthalocyanine (CuPc) and silver (Ag) nanoparticles. The resistive nature of the thermal boundary between CuPc and Ag results in a k_{th} decrease by as much as 50%. Once the Seebeck coefficient is calculated from the simulated electrical conductivity, and ZT's dependence on thermal boundary conductance, effects of particle radii and filler volume concentrations can be examined. With the interfacial engineering and particle size control, ZT enhancement by more than a factor of 10 for organic TE materials can potentially be realized. Such a large boost in performance calls for a nanocomposite system with low thermal boundary conductance and small particle radii. With a combination of chemical doping, surface treatment and thermal boundary effects, $ZT > 1$ is achievable for organic semiconductors.

CHAPTER V

Origins of TBC: Interfacial Bonding

5.1 Introduction

This chapter and **Ch. VI** discuss the fundamental physics of thermal boundary conductance (TBC), focusing on interfaces involving disordered organics. Interfacial bonding strength is proposed and proved to be a crucial factor for TBC at van der Waals bonded interfaces in this chapter. For the specific material system, CuPc/Al, TBC is shown to be influenced by spatial non-uniformity and anharmonic phonon transmission which are both presented in **Ch. VI**.

TBC values between copper phthalocyanine (CuPc) and several metals (aluminum, gold, magnesium, silver) have been measured using the 3-ω method in **Ch. III**. In conventional theories, TBC is supposed to be related to the acoustic properties of the solid state materials. Acoustic Mismatch Model (AMM) and Diffuse Mismatch Model (DMM) have been proposed to model the phonon transmission (*Swartz and Pohl* (1989)). This section starts with the discussion of these two mismatch models, followed by the discrepancies between the experimental and their modeling results. Several possible factors aide from the mismatch that may influence the TBC are discussed, and the interfacial bonding strength is the one that will be extensively discussed in the following sections.

5.1.1 Mismatch Models for TBC

Mismatch models consider only the mismatch the intrinsic thermal properties of the two materials comprising the interface. TBC is written as, $G_b = q/\Delta T$ in **Eq 3.1**, and the heat flux q can be generally expressed by

$$q = \int_{T_1}^{T_2} D_p(\omega) f_p(\omega) v_p(\omega) \tau_p d\omega \tag{5.1}$$

where T_1 and T_2 are the temperature at each side of the interface, D_p is the phonon density of states, v_p is the phonon velocity: both D_p and v_p have been discussed in **Subsection 1.1.2**. f_p is Bose-Einstein distribution which is a function of T.

The most difficult task is the determination of τ_p in **Eq 5.1**, the transmission coefficient. AMM and DMM have different approaches in calculating this crucial coefficient.

Acoustic Mismatch Model (AMM): AMM assumes a perfect flatness of the interface where phonons scatter specularly. The model shares the fundamentals with the optics: the transmission coefficient has similar form with the Fresnel Law. Under the assumption of normal incidence, $\tau_{p,\mathrm{AMM}}$ yields,

$$\tau_{p,\mathrm{AMM}} = 4\frac{Z_1 Z_2}{(Z_1 + Z_2)^2} \tag{5.2}$$

Z in **Eq 5.2** is Acoustic Impedance, the product of material density ρ and sound velocity v_p (**Eq 1.9**), $Z = \rho v_p$. The subindexes represent the two material comprising the interface, respectively.

Diffuse Mismatch Model (DMM): DMM on the other hand, assumes the interface is rough compared to the dominant phonon wavelength. All phonons lost their memory after hitting the interface and scatter in all direction diffusively. The

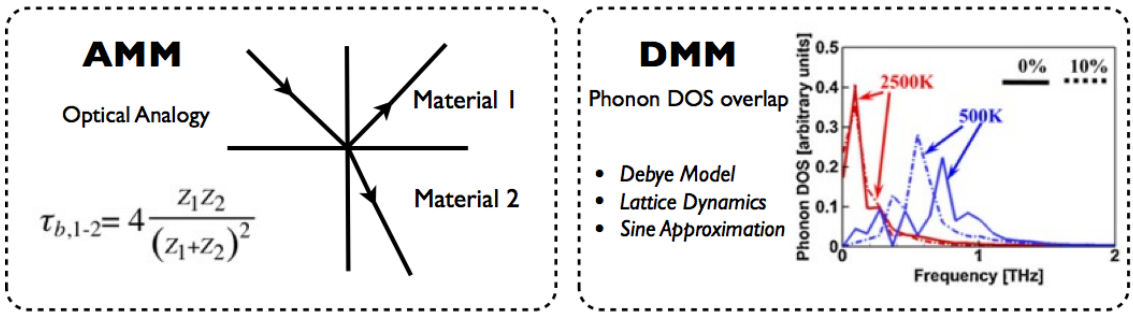

Figure 5.1: Acoustic Mismatch Model (Left) -The calculation of transmission coefficient in AMM is an analogy to optical transmission, the main assumption is coherent transport through the interface. Diffuse Mismatch Model (Right) - The transmission coefficient in DMM is related to the overlapping of materials' phonon DOS; Debye model, sine model and lattice dynamics simulation can be used to calculated phonon DOS. (Figure by Yansha Jin)

transmission coefficient in DMM is expressed as:

$$\tau_{p,\mathrm{DMM}} = \frac{\sum_{\mathrm{mode}} D_{p,2} f_{p,2} v_{p,2}}{\sum_{\mathrm{mode}} D_{p,1} f_{p,1} v_{p,1} + \sum_{\mathrm{mode}} D_{p,2} f_{p,2} v_{p,2}} \tag{5.3}$$

This transmission coefficient relates to the phonon DOS of both materials and the overlapping between the two. For simplicity, most of work use the Debye model (**Eq 1.12**) as phonon DOS.

The principles of AMM and DMM are shown in **Figure 5.1**, both have their limitations and advantages. However, for organic/metal multilayer as deposited under RT by VTE, diffuse scattering is a more reasonable assumption (*Hopkins* (2009)). The nature of the scattering, whether specular or diffuse, is decided by the thermal coherence length L_{coh} and the RMS roughness of the interfaces, δ_{rms}. An quantified parameter is defined to represent the nature of scattering, the degree of specularity, p_{sp}

$$p_{\mathrm{sp}} = \exp\left[-\frac{16\pi^2\delta_{\mathrm{rms}}^2}{L_{\mathrm{coh}}^2}\right] \tag{5.4}$$

In case of the CuPc/Ag multilayers measured in **Chap III**, the roughness of the

interfaces δ_{rms} is around 1∼2 nm. The coherent phonon length, $L_{\text{coh}} = hv_p/k_BT$, where v_p is the sound velocity of CuPc. Measurements in *Sun et al.* (2013) suggest v_p for CuPc is 3000 m/s. Thus, $L_{\text{coh}} \sim 5$ Å. Obviously, the coherent phonon length is nearly 5 times less than the RMS roughness, that leads to $p_{\text{sp}} \sim 0$. Degree of specularity close to zero suggests a diffuse scattering at CuPc/Ag interface.

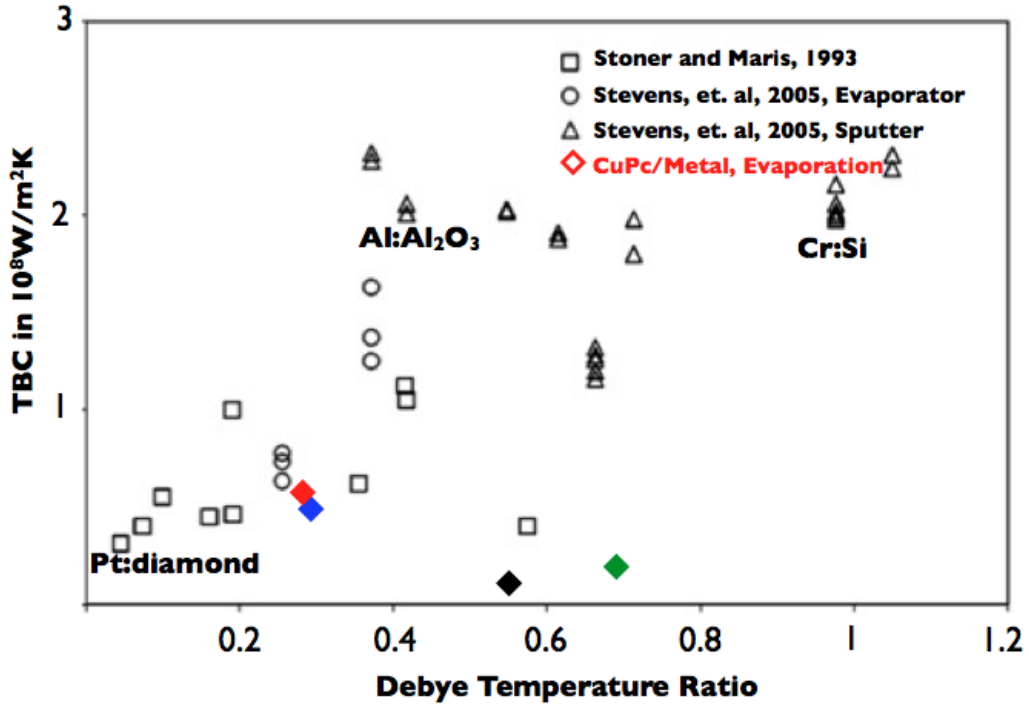

Figure 5.2: TBC vs Debye temperature ratio. Debye model is often used as an approximation for phonon DOS. If DMM is valid, TBC should correlate to the Debye temperature ratio. TBC values shown here roughly follow the monotonic increasing trend, but some data points including TBC of CuPc/metal interfaces do not follow this general trend. (Figure from *Stevens et al.* (2005) and adapted from *Jin et al.* (2012))

5.1.2 Failure of Mismatch Models

However, DMM also cannot accurately predict the TBC values of material systems such as CuPc-metal, and the discrepancies also exist in other material systems. In *Stevens et al.* (2005), a collective set of TBC values is shown in **Figure 5.2**, plotted versus the Debye temperature ratio. Generally, Debye model is a good estimation to

the phonon DOS, thus the Debye temperature ratio roughly correlates to the TBC values. Roughly, the TBC monotonically increases with this ratio. However, quite a few data points deviate from the monotonically trend, this discrepancy is more severe in for the CuPc-metal interfaces.

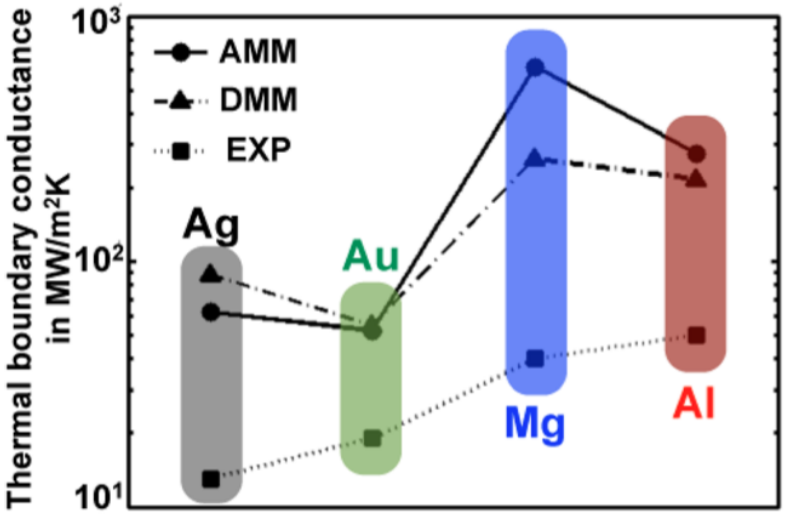

Figure 5.3: TBC of CuPc/metal interfaces calculated by AMM, DMM and measured by 3-ω. The values predicted by AMM and DMM are five times than the measured values. (Figure from *Jin et al.* (2012))

While both AMM and DMM predict that CuPc/gold interface has the lowest transmission probability and TBC among the four CuPc/metal interfaces measured here, see **Figure 3.5**, the experimental results indicate otherwise: TBC of CuPc/Ag is lowest ($1.3 \pm 0.3 \times 10^7 \mathrm{W/m^2K}$) and CuPc/Al has the largest interface thermal conductance ($5.0 \pm 1.5 \times 10^7 \mathrm{W/m^2K}$). (See **Table 3.2**). If one considers only the materials' intrinsic vibrational properties (AMM and DMM), the observed trends in TBC cannot be explained and the predicted values are approximately 5 to 50 times larger than that measured by experiment. (See **Figure 5.3**, *Jin et al.* (2012))

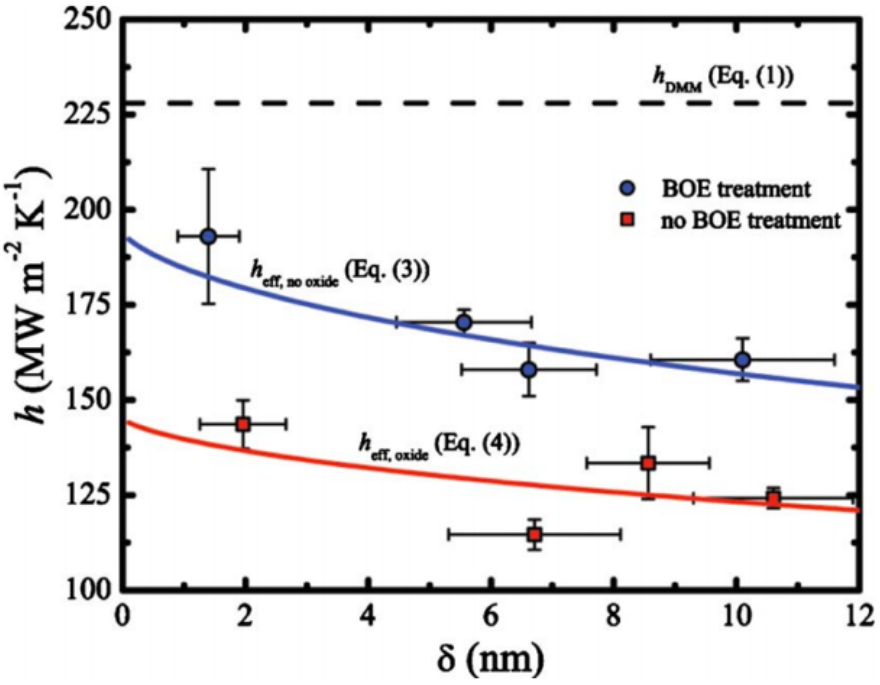

Figure 5.4: TBC changes with the oxidation level of the interfaces. Experimentally measured TBC values w/ and w/o BOE treatment are plotted with error bars. Dashed black line corresponds to DMM, and colored lines are the modeling results from *Hopkins et al.* (2010). (Figure from *Hopkins et al.* (2010))

5.1.3 Other Contributing Factors to TBC

Many theories have been proposed to explain the discrepancies between the various mismatch models and the experiments. The interfacial disorder and the size effect have been proved to be part of the reason. Oxide layer was introduced to change the chemistry and the morphology at the interface in *Hopkins et al.* (2010). G_b increases after the Buffered Oxide Etch (BOE) treatment (See **Figure 5.4**). The size effect is presented in *Li and Yang* (2012), shown in **Figure 5.5**, the phonon confinement results in new peaks/dips in the phonon transmission.

Among the possible factors that are contributing to the TBC, the interfacial bonding strength is the most important factor for systems involving organics, because the organic materials are weakly bonded by van der Waals interaction. Another reason

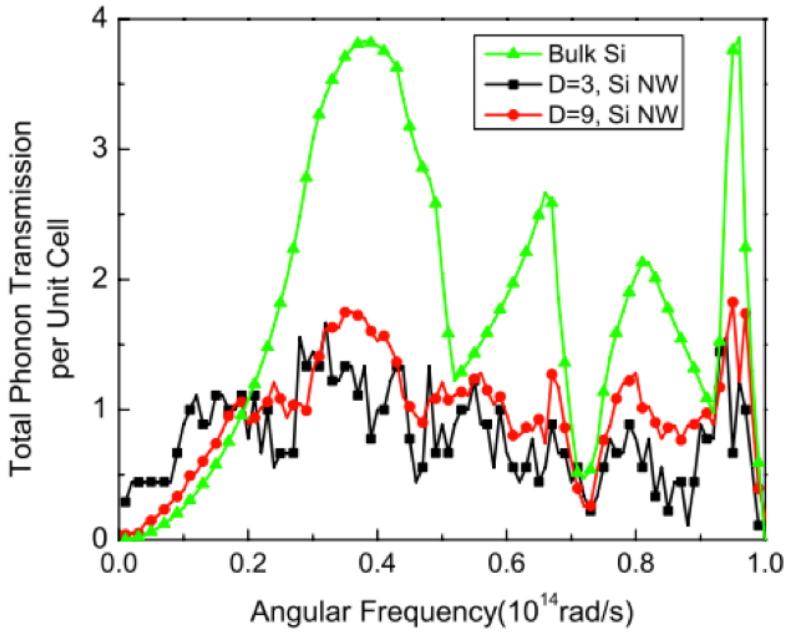

Figure 5.5: Phonon transmission peaks/dips change due to the size effect. Phonon transmission is calculated using the Green Function Method in Si with different transverse confined sizes. (Figure from *Li and Yang* (2012))

for the research attention to interfacial bonding is that its correlation to TBC only existed in theory before the year 2010. One example of the theoretic modeling is *Ong and Pop* (2010), see **Figure 5.6**: As interfacial bonding strengthened in molecular dynamics simulation, the temperature discontinuity ΔT became small indicating a larger TBC.

5.2 Correlation Between Interfacial Bonding vs TBC at Organic/Metal Interfaces

In this section, a definite relation between interfacial bonding strength, which is qualified by peel-off tests, and TBC at CuPc/metal interfaces experimentally.

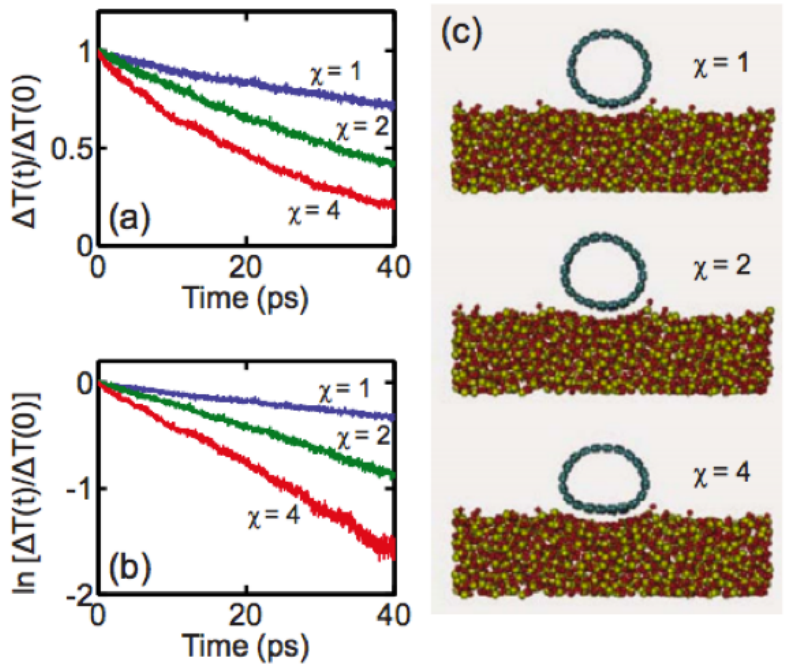

Figure 5.6: MDS of TBC's dependence on the interfacial bonding for CNT/Au interfaces. (a) The decay of the normalized CNT temperature varies with the CNT/Au substrate interaction strength χ. (b) Natural logarithm of (a). (c) Cross-sectional view of (10, 10) CNT for different χ values: CNT deforms more when χ becomes larger. (Figure from *Ong and Pop* (2010))

5.2.1 Peel-off Test

Briefly, several Indium Tin Oxide (ITO) substrates were vacuum-coated with 100 nm thick CuPc films simultaneously. The samples were then masked and different metals were vacuum evaporated through arrays of 1 mm apertures in the masks, capped by silver to prevent corrosion in the ambient and ensure identical adhesion to the scotch tape. After the test, the samples were imaged using optical microscopy and SEM. A similar approach to characterizing interfacial adhesion strength was introduced by *Losego et al.* (2012): by varying the laser fluency, the induced stress load is modified, and failure of the interface resulting in delamination was observed at different stress amplitudes for different material systems.

The schematic drawing of the peel-off test is present in **Figure 5.7** along with a

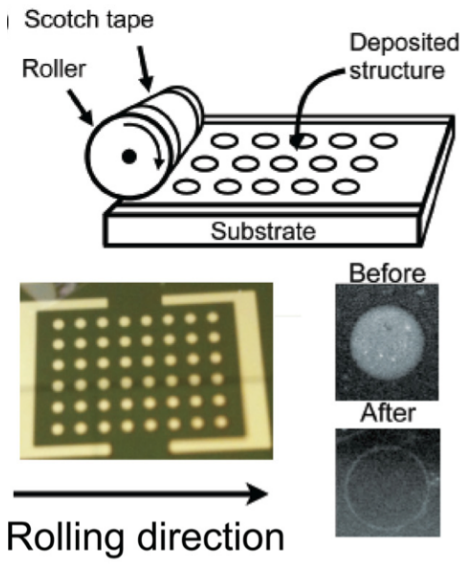

Figure 5.7: (Top) - Schematic representation of the peel-off test. (Bottom) - Optical micrographs of the deposited structure (rolling direction indicated) along with images of 1 mm -diameter dot before and after peel off. (Figure from *Jin et al.* (2012))

plane view of the films along with optical micrographs of the 1 mm diameter dot before and after the peel-off (CuPc-Ag interface). Peel-off percentage was defined as the statistical average over 10 or more dots as the ratio of the area of the layered structure (Ag/metal/CuPc/ITO) that breaks at the metal/CuPc interfaces to the total area covered by metal. The peel-off percentage can indirectly quantify the bonding strength by comparing the interfacial bonding of CuPc/metal with CuPc/ITO and bonding of CuPc to itself. Interface bonding of CuPc/ITO is observed via peel-off tests to be approximately of the same strength as CuPc interior bonding.

5.2.2 Experimental Confirmation

The peel-off test can semi-quantitatively describes the interfacial bonding strength, and a definite correlation between these bonding strength and TBC is shown: as we plot the TBC against the peel-off percentage, the trend clearly indicates that the weaker the interfacial bonding (which is represented by larger peel-off percentage),

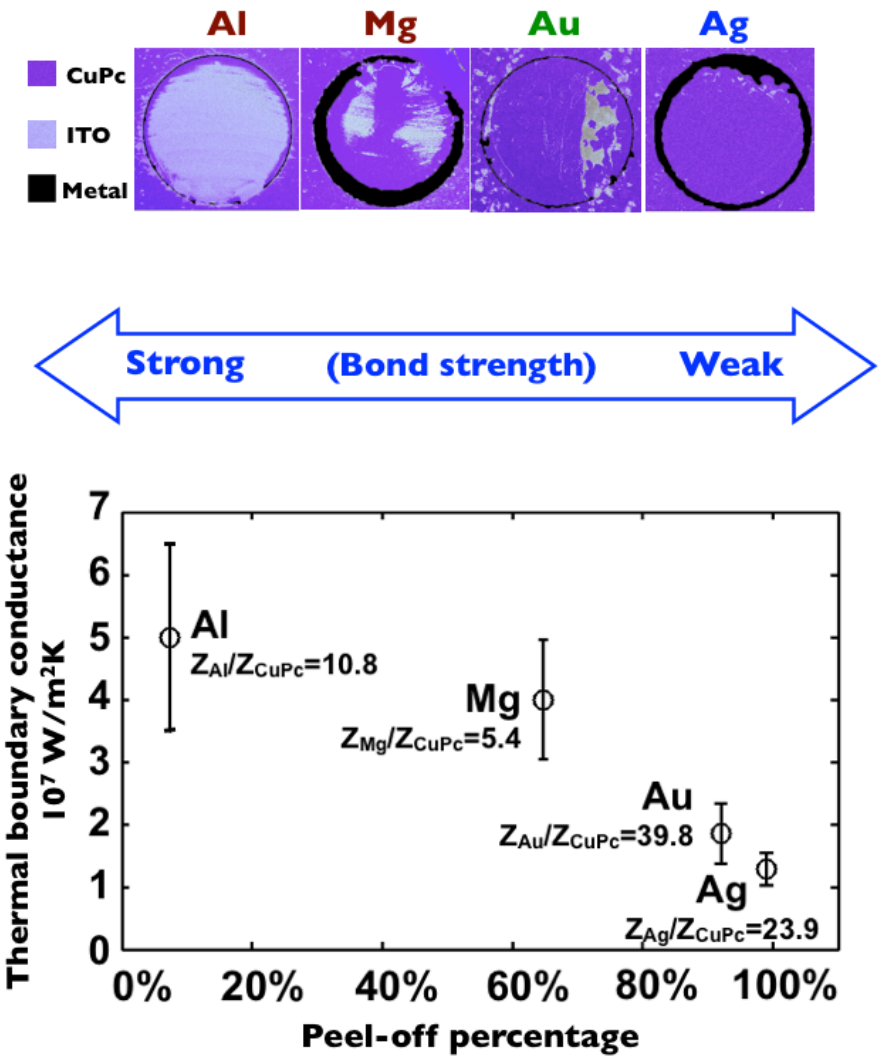

Figure 5.8: Experimental proof of the correlation between TBC and interfacial bonding strength. (Top) - Representative SEM images of the stacks after peel-off. Metal was deposited on CuPc film using masks with dots of 1 mm diameter arrays. (Bottom) - TBC of CuPc-metal interfaces versus peel-off percentage. Peel-off percentage is the ratio of the area of the layered structure (Ag/metal/CuPc/ITO) that breaks at the metal/CuPc interfaces to the total area covered by metals. (Figure from *Jin et al.* (2012))

the smaller the TBC of the corresponding CuPc/metal system. (See **Figure 5.8** - bottom) SEM images are arranged from left to right starting from the interface with the highest peel-off percentage to the lowest in **Figure 5.8** -top.

To further confirm the precise location in the stack where delamination occurs dur-

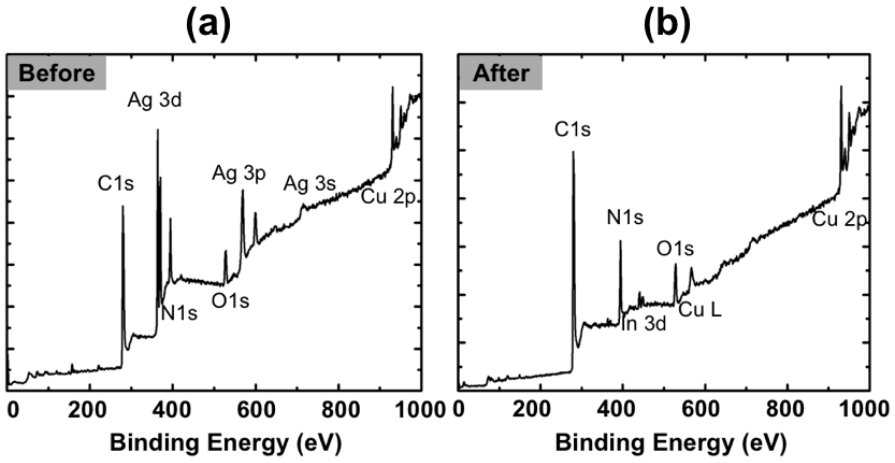

Figure 5.9: X-ray photoelectron spectroscopy evidences on peel-off tests. (a) Before the peel-off test. Ag, Cu, C, N,O peaks were observed, indicating that Ag and CuPc are at the surface of the film. (b) After the peel-off test. the C, N, Cu, O, Indium peaks suggest that Indium tin oxide and CuPc are on the top surface. (Figure by Yansha Jin)

ing peel-off, we have performed X-ray Photoelectron Spectroscopy (XPS) on CuPc/Au sample before and after peel-off as an additional test. The results have confirmed that the bright region is indeed the ITO substrate devoid of any organic or metal films (See **Figure 5.9**). Thus, the significant contribution of the interfacial bonding effect to TBC is experimentally confirmed for this type of van der Waals interfaces. Noted that the interfacial bonding effect overrides the trend of the materials thermo-property mismatch, represented by the Z ratios in **Figure 5.8**, which leads to the next question: How to evaluate the balance of the contributions from two major contributors to TBC at van der Waals bonded interfaces, the thermo-property mismatch and the interfacial bonding.

5.3 TBC Modeling with Bonding Modifications

Further understanding of the above question can be provided the TBC modeling and simulations. A short review of previous models/simulations that consider both material property and interfacial bonding are discussed in this section. Both

analytical modelings and computer simulations showed proofs of interfacial bonding involvements: *Prasher* (2009) proposed a model that incorporates the weak nature of van der Waals bonding into the traditional acoustic mismatch model, relating the bond strength to TBC. More recently, *Zhang et al.* (2011) presented the scattering boundary model in atomic junctions to investigate the significance of bonding. The model indicates that the cut-off frequency and the TBC are linearly dependent with the interface bonding strength in 1D chains. In terms of computer simulations, using lattice dynamics, *Stoner and Maris* (1993) and *Young and Maris* (1989) showed that the phonon transmission coefficient is strongly affected by the spring constant linking the two materials. Molecular dynamics simulation work from *Ong and Pop* (2010), mentioned earlier in **Section 5.1.3**, predicted a linear dependence of the TBC on the strength of the interface interaction for weakly bonded carbon nanotubes and SiO_2.

These works above are summarized in the following subsections.

5.3.1 Modified Acoustic Mismatch Model

Prasher (2009) presented a model that incorporates the weak van der Waals bonding into the traditional acoustic mismatch model, relating the interfacial bond strength to TBC. The model is based on the harmonic approximation that the two materials are connected by a spring. The transmission coefficient under this condition is written as

$$\tau_{p,\text{Prasher}} = \frac{4Z_1Z_2}{(Z_1+Z_2)^2 + \frac{\omega^2}{n^2K_{\text{sp}}^2}(Z_1Z_2)^2} \tag{5.5}$$

where n is the number density of the interfacial atoms and K_{sp} is the spring constant. The spring constant can be obtained by the second derivative of the interacting potential, $\phi(r)$. Take Lenard Jones (LJ) potential for example,

$$\phi(r) = -4\epsilon\left[\left(\frac{\sigma_{LJ}}{r}\right)^6 - \left(\frac{\sigma_{LJ}}{r}\right)^{12}\right] \tag{5.6}$$

where σ_{LJ} is the length scale parameter for LJ potential. The spring constant K_{sp} yields,

$$K_{\text{sp}} = \left(\frac{\partial^2 \phi}{\partial r^2}\right)_{r=r_0} = \frac{72\epsilon}{2^{1/3}\sigma_{LJ}^2} \tag{5.7}$$

I replot the transmission coefficient's dependence on the acoustic impedance ratio

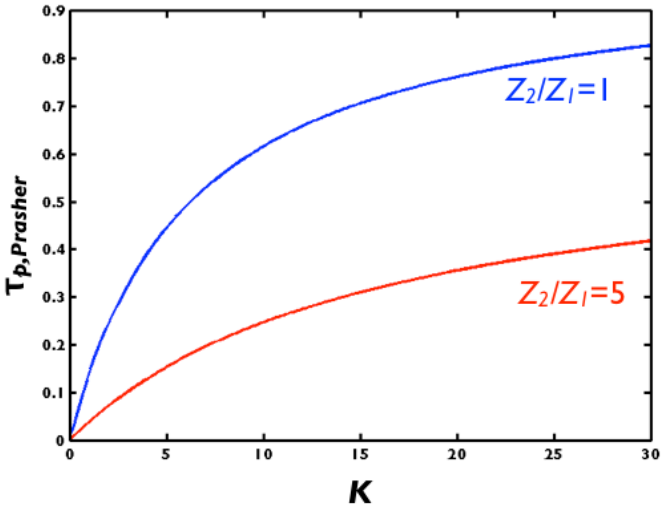

Figure 5.10: Transmission coefficient modeled following the work,*Prasher* (2009), with acoustic impedance ratio Z_2/Z_1 as 1 and 5. (Figure by Yansha Jin)

and the spring constant in **Figure 5.10**. Comparing the two curves under $Z_2/Z_1 = 1$ and $Z_1/Z_2 = 5$ conditions, while the range of K_{sp} is kept the same, $\tau_{p,\text{Prasher}}$ continues varying at high spring constant regime in the $Z_1/Z_2 = 5$ while $\tau_{p,\text{Prasher}}$ of the $Z_1/Z_2 = 1$ is already saturated.

Prasher's model is modified from acoustic mismatch model, thus not rigorous in describing rough interfaces. Another limitation for this model is the assumption of the harmonic spring connecting the two materials, which exclude the multiple phonon transmission. Multiple phonon (anharmonic) transmission is important at high temperature ($T \gg T_{\text{Debye}}$), and this effect will be discussed extensively in **Ch. VI**.

5.3.2 Scattering Boundary Model

Zhang et al. (2011) reported the Scattering Boundary Model with interfacial bonding modification based on an atomic junction. The schematic representation of a 1D atomic junction is shown in **Figure 5.11**. The mathematical derivation is similar with 1-D monatomic chain (**Eq 1.14**).

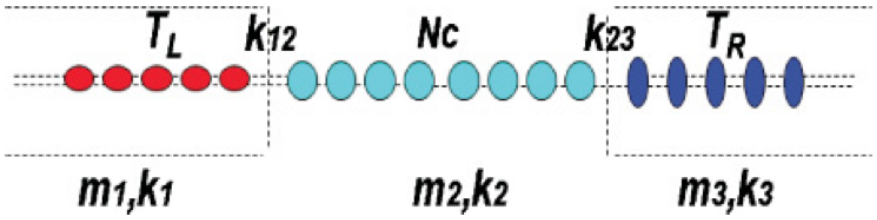

Figure 5.11: Schematic illustration of the two-junction atomic chain in the Scattering Boundary Model. The right and left regimes are semi-infinite representing the two materials. The middle part is the interfacial regime which is coupled by harmonic springs to each sides, with spring constants represented by k_{12} and k_{23}. The mass and spring constants are defined as indicated. (Figure from *Zhang et al.* (2011))

The main idea of the model is the introduction of a few atoms of intermediate chain, with its own mass and spring constants, creating a two-junction atomic chain. (See **Figure 5.11**). Solution of the equation of motion yields to the expression for transmission coefficient as follows,

$$\tau_{p,\mathrm{SB}} = \frac{(1-|r_{12}|^2)(1-|r_{23}|^2)}{|1-r_{23}r_{21}\lambda_2^2(N_c-1)|^2} \tag{5.8}$$

where r_{ij} is

$$r_{ij} = \frac{k_i(\lambda_i - 1/\lambda_i)(k_j - k_{ij} - k_j/\lambda_j)}{(k_i - k_{ij} - k_i/\lambda_j)(k_j - k_{ij} - k_j/\lambda_j) - k_{ij}^2} - 1 \tag{5.9}$$

where $\lambda_j = e^{iq_j a_j}$, q_j is the wave vector, a_j represents the interatomic spacing for the atom at j^{th} atomic site.

The major result for this model is that a maximum transmission happens at

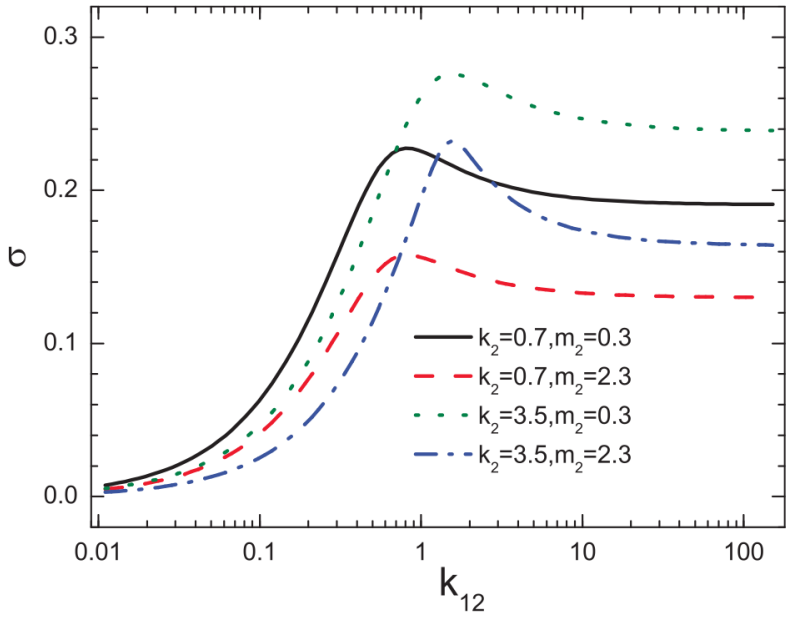

Figure 5.12: TBC dependence on interfacial spring constant (k_{12}) calculated by one-junction atomic junction, Scattering Boundary Model, with k_{12} as the point-junction spring constant. $k_1 = 1.0$ and $m_1 = 1.0$. (Figure from *Zhang et al.* (2011))

$k_{12} = \frac{2k_1k_2}{k_1+k_2}$ for a single junction. This value is the geometric average of the bulk spring constants of the two materials. As a result, an asymptote is observed in TBC at this interfacial spring constant value (See **Figure 5.12**).

Scattering Boundary Model is more fundamental in physics than the Prasher's model, but has difficulties defining the mass and spring constant in complicated 3-D complex with non-trivial molecular structure, such as CuPc and other organic molecules.

To sum up **Subsection 5.3.1** and **Subsection 5.3.2**, theories like *Prasher* (2009) ascribe the interfacial bonding dependence to the low-pass filter effect: the harmonic interfacial spring only supportes vibrational modes with frequencies smaller than the cut-off frequency ω_c, which is proportional to the interfacial bonding strength represented by the interfacial spring constant K_{sp}; When the bonding is strong enough (and ω_c large enough), nearly all the existing modes are supported and TBC is max-

imized at a saturation value, G_{b0}. Other works like*Zhang et al.* (2011) suggest the TBC is maximized at the harmonic average of the two spring constants of the leads, and decrease, asymptoting to a constant G_{b0}.

Due to the various of limitations of the analytical models, some computational efforts come in aiming for a more complete understanding on TBC. The following subsections present Lattice Dynamics Simulations (LDS) and Molecular Dynamics Simulations (MDS), while still focusing interfacial bonding strength and TBC relations.

5.3.3 Lattice Dynamics Simulations

Stoner and Maris (1993) and *Young and Maris* (1989) are among the earliest theoretical works relating the interfacial spring constant to phonon transmission. The frameworks of lattice dynamics has been described in **Subsection 1.1.2**. The physical picture is similar to Scattering Boundary Model, **Subsection 5.3.2**, with single junction connecting by a tunable harmonic spring.

Related results from these works are shown in **Figure 5.13**. The average phonon transmission coefficient is plotted against the transmission frequency; while the interfacial springs strength varies in this series of plots. For small K_{sp} (less than effective spring constants of the materials), the transmission coefficient decreases because the weak bonding strength cannot support transmission at higher frequencies. As K_{sp} increases, transmission at higher frequencies increases, suggesting the ability of the connecting spring's in supporting the phonon modes at these higher frequencies. These results share the similarity with the low-pass filter effect as *Prasher* (2009). At the same time, further increase of K_{sp} reduces the transmission. In *Young and Maris* (1989), this effect is well-explained by considering the extreme condition, $K_{\text{sp}} \to \infty$, which makes the interface a completely rigid entity with the interfacial particle mass the sum of the two comprising materials' atomic masses. This produces a heavier

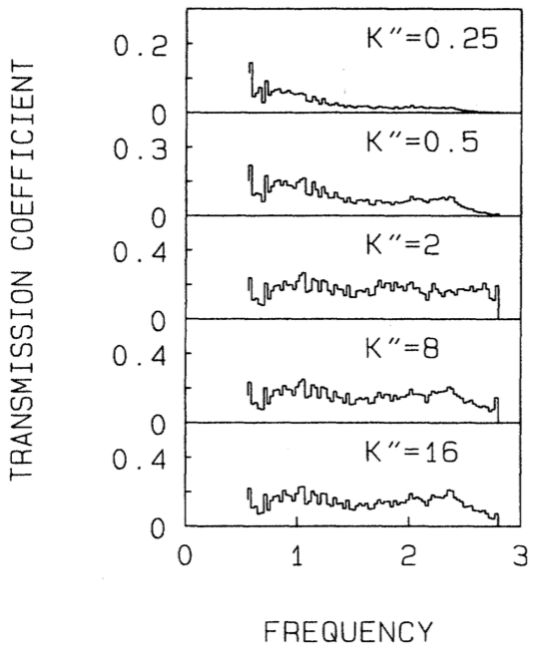

Figure 5.13: Average phonon transmission coefficient versus frequency with various of interface spring constants values. Material 1: k=1, m=1; Material 2: k=4, m=1. For weak interface springs, high frequency phonon modes are not supported. If the springs strengthen further, all phonon modes can be supported; Phonon transmission drops slightly after an asymptote point. (Figure from *Young and Maris* (1989))

interface junction, which explains the transmission reduction at high K_{sp}.

5.3.4 Molecular Dynamics Simulations

In recent years, Molecular Dynamics Simulations (MDS) has emerged as a powerful tool for calculating of thermal properties including those of organic materials (*Hu et al.* (2009), *Hu et al.* (2010), *Ong and Pop* (2010)). Besides Ong's work that mentioned in the **Subsection 5.1.3**, *Hu et al.* (2010) also discussed MDS results on Au/Si interface by inserting Self-Assembled Monolayers (SAM) in between, shown in **Figure 5.14**. The tuning of the interfacial bonding strength was achieved by varying the SAM-Si interaction in the MD simulations. Increasing the Si-SAM interaction to five times of the original value significantly decreased the temperature discontinuity

at the Si-SAM interface, which indicated a smaller TBC.

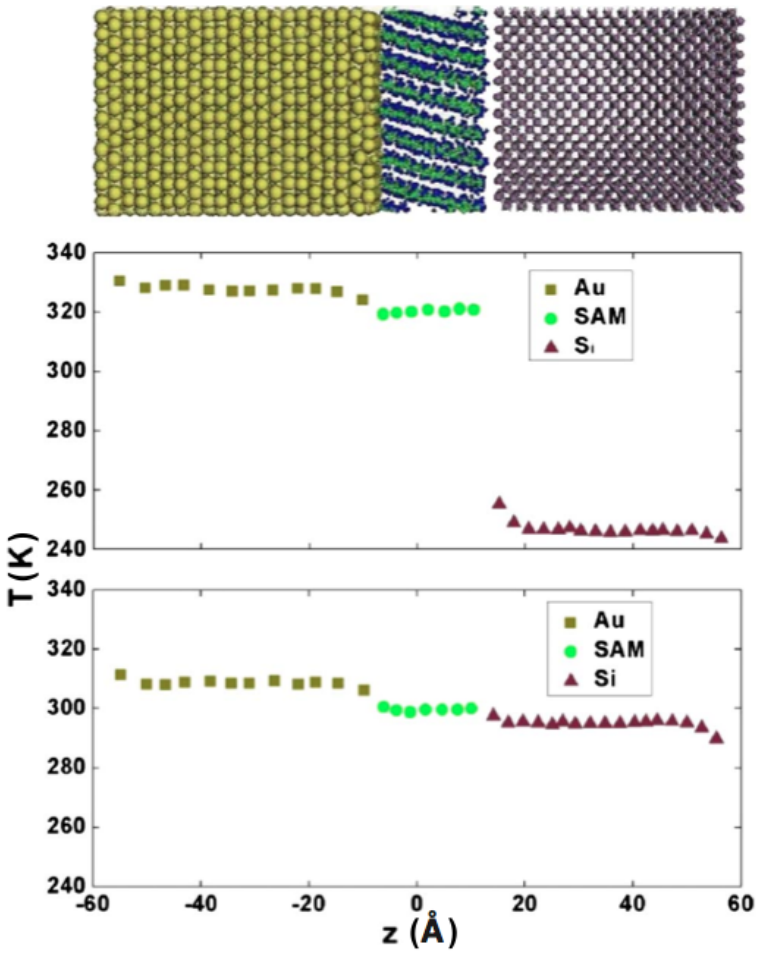

Figure 5.14: (Top) Side-view of the simulation collection, Au-SAM-Si. (Middle) Equilibrium temperature profile for a standard Au-SAM-Si junction. (Bottom) - Equilibrium temperature profile for the same junction, with five-time stronger Si-SAM interaction. (Figure from *Hu et al.* (2010))

MDS on systems involving complicated molecules like CuPc, however, has seldom been reported. While more extensive details regarding the MDS of the CuPc/metal systems will be provided in Chen Shao's publications and thesis (Kieffer group, University of Michigan, Ann Arbor, Materials Science and Engineering), the following section briefly describes how the interfacial bonding strength is tuned, along with its relationship to the Young's modulus relevant to the discussion.

5.4 Molecular Dynamics Simulations on CuPc-Metal Junctions

A Lennard-Jones 9-6 potential, U_{vdW} is employed to describe the interface and to represent the strength of interfacial interactions.

$$U_{\mathrm{vdW}} = \sum_{i,j} \chi \varepsilon_{ij} \left[2 \left(\frac{r_{ij}^{0}}{r_{ij}} \right)^{9} - 3 \left(\frac{r_{ij}^{0}}{r_{ij}} \right)^{6} \right] \tag{5.10}$$

where r_{ij} is the distance between atoms; ε_{ij} is defined as the square root of the product of the energy parameter of the materials at each side of the interface.

$$\varepsilon_{ij} = \sqrt{\varepsilon_i \varepsilon_j} \tag{5.11}$$

The geometric mean is a good approximation for the interface energy parameter when systems do not involve highly polar molecules.

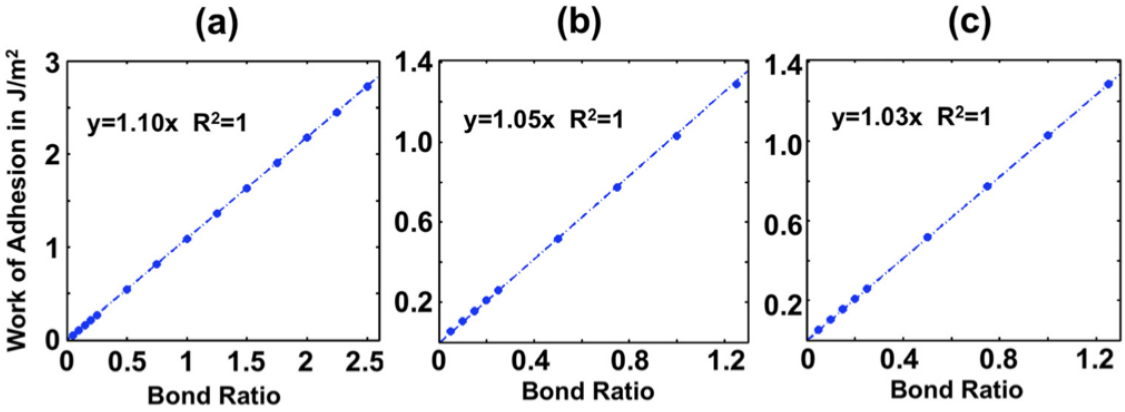

Figure 5.15: Work of adhesion scales linearly with the bond ratio (a) CuPc/Au, (b) CuPc/Ag and (c) CuPc/Al. (Figure from *Jin et al.* (2012))

The interfacial bonding strength could be further tuned by the bond ratio χ in **Eq 5.10**. To confirm this, the work of adhesion at the interface is calculated. The sandwiched CuPc/metal junction is first relaxed under room temperature with

periodic boundary condition in all dimensions. The total energy of the system is minimized under this condition as E_p. The periodicity is then interrupted at the CuPc/metal interface, leaving two free surfaces: one with CuPc and the other with metal atoms. The total energy of the system with free surfaces in minimized as E_s. The work of adhesion at the interface is then calculated as: $W = E_s - E_p$, and depends linearly on χ (See **Figure 5.15**). Thus the bonding strength of the two materials can be tuned via the bond ratio effectively.

Considering **Eq 5.11** and the linear relation between χ and the work of adhesion, the effective modulus at the interface could simply share the same relation with the microscopic energy parameter.

$$E_{ij} = \chi\sqrt{E_i E_j} \tag{5.12}$$

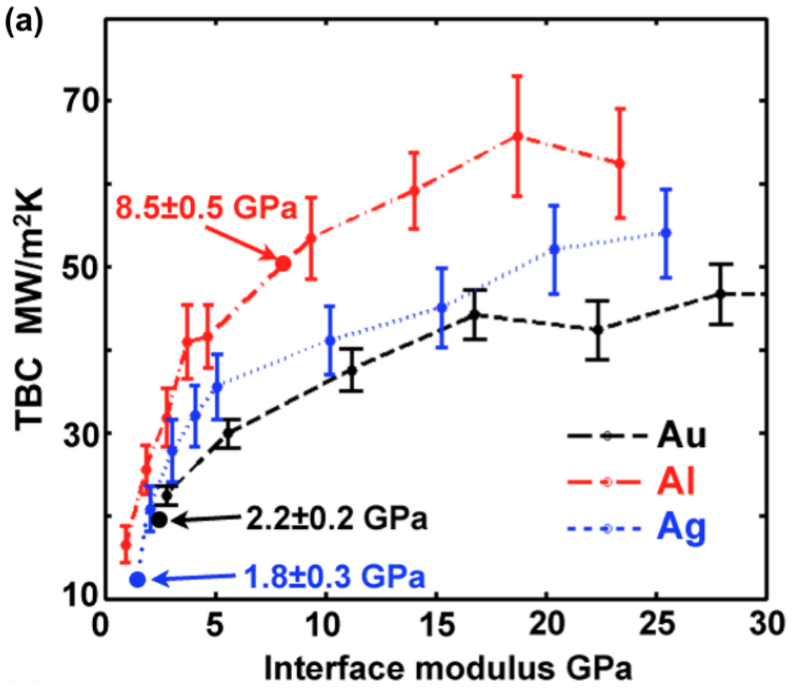

Figure 5.16: MD simulated TBC versus the effective modulus. The measured TBC is marked with circles corresponding to the systems' interface modulus. (Figure from *Jin et al.* (2012))

Figure 5.16 presents the MD simulated TBC versus the effective modulus for CuPc/Ag, CuPc/Au and CuPc/Al. Though the MD simulated results cannot explicitly exclude the asymptoting behavior nor the monotonic increase trend, it supports the low-pass filter theory and considers two and multiple phonon transmission processes.

The next section presents the comprehensive analysis of MD simulation on TBC, TBC measurement data and the peel-off test results, focusing on the consistency of these results.

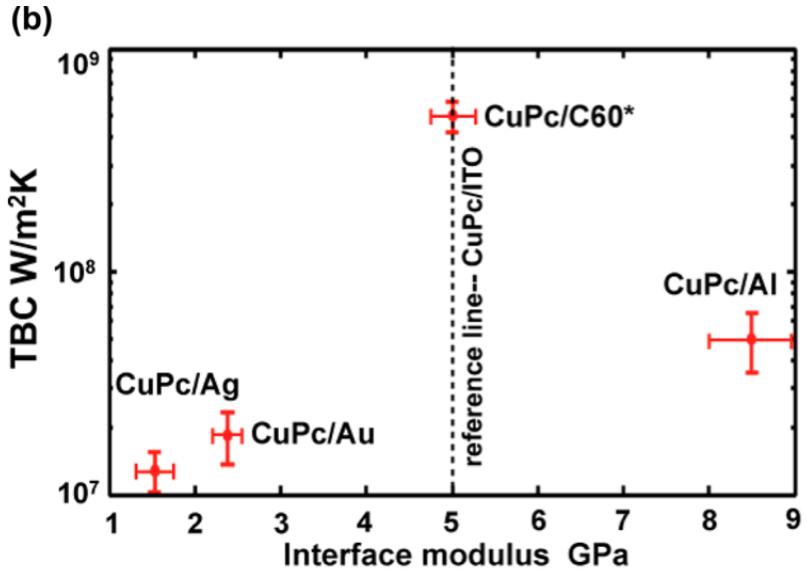

Figure 5.17: Experimentally measured TBC values of different materials system made by VTE plotted versus their effective interface modulus extracted from MDS. (Figure from *Jin et al.* (2012))

5.5 TBC at CuPc/Metal Interfaces: Results and Discussion

The MD-calculated work of adhesion is in agreement with the peel-off tests and the X-Ray standing wave experiments, so that the correspondence between TBC derived from MD simulations and experimentally measured TBC values ultimately allows the interfacial modulus to be extrapolated. The colored points in **Figure 5.16** represent

the experimentally measured values of TBC, while the interface moduli are given by the x-coordinates of these data points. The interfacial modulus is extracted and re-plotted in **Figure 5.17**; the values reported here for the vacuum evaporated CuPc-metal interfaces are: CuPc/silver? 1.8 ± 0.3 GPa; CuPc/gold, 2.2 ± 0.2 GPa and CuPc/aluminum, 8.5 ± 0.5 GPa. Using these values and comparing them with the reference line (CuPc/ITO interfacial modulus **Figure 5.17**, the consistency between this set of results and the peel-off test is observed. (See **Figure 5.8**): when the interface modulus value lies left to the reference line (CuPc-silver and CuPc-gold), over 90% of the film breaks at the CuPc/metal interface in the silver/metal/CuPc/ITO structure; interface bonding for CuPc/aluminum is stronger than that of CuPc/ITO and, indeed, less than 1% peel-off percentage is observed.

The trend in the interfacial bonding strength among these CuPc/metal systems (CuPc/Ag < CuPc/Au < CuPc/Al(Mg)) is consistent, with recent results from X-ray standing wave and spot-profile low energy electron diffraction experiments on sub-monolayer adsorption of CuPc on different metal substrates as described in the literature (*Kröger et al.* (2011); *Stadler et al.* (2009); *Kröger et al.* (2010)). Intermolecular interactions are purely van der Waals (vdW)-like for CuPc/gold interface, while repulsive forces are observed between CuPc molecules near the interface in the CuPc/silver system. X-ray standing wave analysis shows that the C-Ag and N-Ag distances are larger for CuPc/silver interfaces, which suggests that the substrate-mediated repulsive intermolecular interaction causes a weaker molecule-substrate adhesion. In the case of the CuPc-aluminum interface, charge transfer gives rise to an electrostatic moment in CuPc and strengthens the bonding between CuPc and the metal.

Up until this point, the agreements between MDS, peel-off test, TBC measurements and literature on nature of interfacial bondings at CuPc/metal interfaces are confirmed. But, the question still remains: how to evaluate the significance of the

interfacial bonding effect? In **Figure 5.16**, it is evident that for CuPc/Au and CuPc/Ag interfaces, the TBC experimental values lie in the range where the TBC is very sensitive to the effective interfacial modulus. But, the slopes of the TBC increase for these systems are not the same, and neither is the saturation value for TBC at sufficient high bonding strength. The next section represents the result regarding TBC at organic/organic systems, which will give more insight on the origins of TBC. The organic/organic interfaces do not a large mismatch but do exhibit a weak interfacial bonding strength compared to organic/metal interfaces.

5.6 TBC at Organic/Organic Interfaces

As observed in **Figure 5.16**, the TBC is mainly dependent on the interfacial bond strength and the saturation value of TBC, G_{b0}. The contribution of these two factors to TBC can be further understood by comparing the behavior of organic/metal to that of organic/organic interfaces. A data point is mapped in **Figure 5.17** representing the TBC (450 ± 130 MW/m^{2}K) and interfacial bonding strength of the CuPc/C_{60} interface. Despite the weak bonding ($\sim$5 GPa), its TBC value is an order of magnitude higher than that of the CuPc/metal system. As indicated in the inset of **Figure 5.18**, the overlap of phonon density of states (calculated using lattice dynamics, following the work of *Young and Maris* (1989)) for CuPc/C_{60} is larger than that of CuPc/gold, which leads to a higher saturation TBC (G_{b0}) for CuPc/C_{60} interfaces: since the CuPc/C_{60} interface, unlike the simulated structure in the Scattering Boundary Model (*Hu et al.* (2010)), is not trivial to be treated as an atomic junction due to the complex interfacial atomic structure. One can still use the modified AMM in *Prasher* (2009) to predict the relationship between the interfacial modulus and TBC for now, which also capture the general trend for TBC vs interfacial bonding. (**Figure 5.18**). Compared with CuPc/gold system, TBC only drops by 10%, while for CuPc/gold interface TBC drops more than 50% compared to G_{b0}. Hence, while weak bonding is the main

limiting factor for TBC for the VTE deposited CuPc/metal interfaces, for systems with a small mismatch like CuPc/C_{60}, interface bonding effects appear to be less significant.

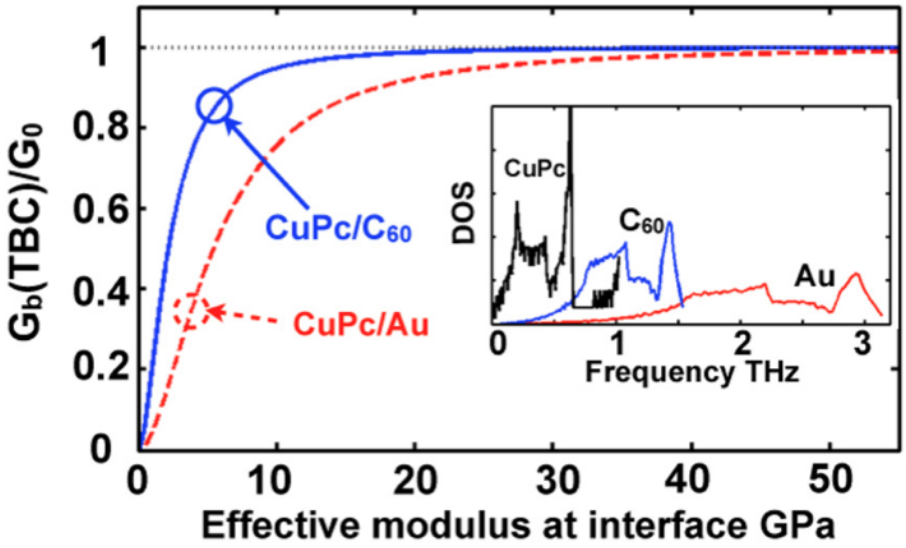

Figure 5.18: Plots of the normalized TBC versus varying modulus at the interface for CuPc/Au and CuPc/C_{60}. The arrows are pointed to the TBC of the corresponding bonding strength at the interface of each systems. The inset represents the DOS of metal, C_{60} and CuPc calculated using lattice dynamics (acoustic phonon only). (Figure from *Jin et al.* (2012))

5.7 Other Supporting Evidence

Besides CuPc/C_{60} and CuPc/metal interfaces, Thermal conductivities were measured for chloro-subphtalocyaninato boron(III) (SubPc)/metals, C_{60}/metals and SubPc/C_{60} multilayer structures. **Figure 5.19** and **Figure 5.20** present the results for these measurements. C_{60}/Ag shares similar slope with CuPc/Ag while the slope represents the TBC (**Eq 3.3**). For SubPc/metal interfaces, limited samples are tested without varying the layer thickness. Compare with the previous CuPc/metals results, these few data points match well with CuPc/metal, suggesting similar TBC. For organic/organic interfaces, the thermal conductivities of multilayers are close to

that of two materials in parallel. No significant boundary effect is observed for these organic/organic systems.

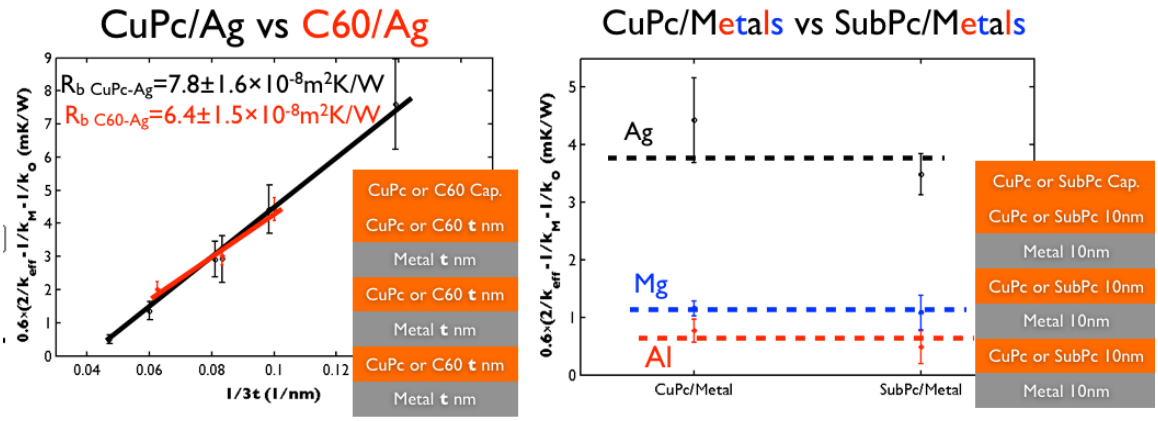

Figure 5.19: Thermal conductivity measurements for SubPc/metals, C_{60}/metals multilayer structures. (Figure by Yansha Jin)

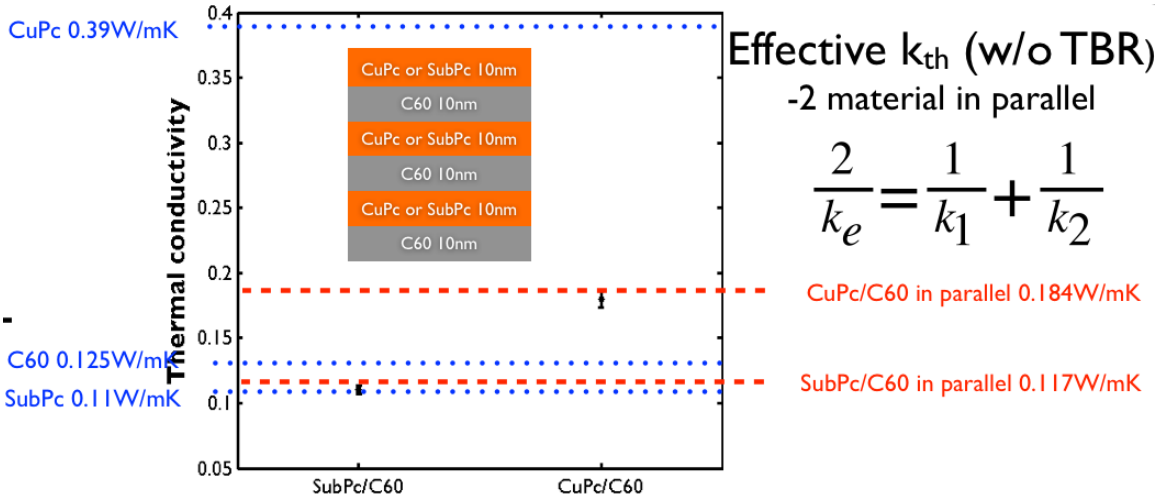

Figure 5.20: Thermal conductivity measurements for C_{60}/SubPc, CuPc multilayer structures. (Figure by Yansha Jin)

5.8 Summary

The thermal boundary conductance of CuPc/metal (Al, Ag, Au, Mg) system is found to be closely correlated to the bonding strength at the organic semiconductor-metal interface. Molecular dynamics calculations of TBC were performed on these systems with varying interface bonding strength. Combining MD simulations with the experimentally measured values of TBC, an effective interface modulus was extracted for each system, showing results consistent with adhesion tests. Finally, organic/organic interfaces were studied; regardless of the similar bonding strength between the organic/metal and organic/organic systems, the latter exhibits an order of magnitude higher TBC due to the larger overlap in the acoustic phonon spectrum between CuPc and C_{60}, suggesting that the TBC of the organic-organic interface is less sensitive to bonding. In conclusion, one need to have a comprehensive knowledge of the material acoustic properties (Phonon DOS, sound velocity) and the interfacial bonding strength to accurately evaluate the thermal boundary conductance of the corresponding material system. For van der Waals interfaces (effective bonding modulus: 1$\sim$10 GPa) that have a small DOS overlap, interfacial bonding is the major factor in boundary phonon transmission; while the systems have less mismatch, the TBC is still dominated by acoustic properties.

CHAPTER VI

Origins of TBC: Anharmonicity and Spatial Non-Uniformity

6.1 Introduction

In the previous chapter, different analytical models and computer simulation techniques were discussed in items of their ability in calculating the Thermal Boundary Conductance (TBC) of interfaces involving disordered organics. The limitations of these techniques are also presented, and it is believed that the Molecular Dynamics Simulations (MDS) is the most comprehensive and accurate way to analyze the TBC. However, despite the accuracy of the MDS, it can be time-consuming for systems involving complicated molecules such as CuPc. Developing a better analytical model that considers other important factors such as interfacial bonding, can help characterizing the interfacial thermal transport and assisting prescreening materials in device design, such as thermoelectric and optoelectronic devices.

In this chapter, the discussion starts with the comparison between the mismatch models (**Section 5.3.1**) and MDS (**Section 5.3.4**) on the CuPc/metal interfaces, aiming to extract the missing physics for the current analytical models.

Specifically, there are two central influence on TBC at organic/metal interfaces that cause the inaccuracy of the analytical models like the Modified AMM. One is

the anharmonic phonon transmission processes discussed in **Section 5.3**: the contribution from the anharmonic processes to TBC is extracted from MDS and will be presented in **Section 6.3**. Another important factor is the spatial non-uniform phonon transmission, which has been never proposed in any material systems before. The evidence for this spatial non-uniform transmission also examined by MDS by analyzing the displacements of the atoms near the interface, see **Section 6.4**.

6.2 Mismatch Models with Interfacial Bonding Modifications

It has been widely realized that the mismatch models are not adequate to describe the physical processes of the interfacial thermal transport. Especially for interfaces such as organic semiconductor and metal, whose bonding is weak and material mismatch is large, the interfacial bonding strength is the main influence in thermal transport across the interface. By modifying the expression of transmission coefficient, this bonding influence can introduced to both AMM and DMM. The former was discussed in Prasher's work, the interfacial bonding is represented by the harmonic spring, with spring constant K_{sp}. The transmission coefficient, $\tau_{\mathrm{AMM,K}}$ is expressed as, (re-wrote **Eq 5.2**)

$$\tau_{\mathrm{AMM,K}}(\omega) = \frac{4Z_{\mathrm{o}}Z_{\mathrm{m}}}{(Z_{\mathrm{o}}+Z_{\mathrm{m}})^2 + \frac{Z_{\mathrm{o}}^2 Z_{\mathrm{m}}^2 \omega^2}{N_{\mathrm{int}} K_{\mathrm{sp}}^2}} \tag{6.1}$$

the above transmission coefficient is frequency dependent, indicating the interfacial spring behaves differently according to the phonon frequency. Several works have described the physics as the low-pass filter, thus, we could also modify the transmission coefficient as follows,

$$\tau_{\mathrm{DMM,K}}(\omega) = \frac{\gamma^2}{\gamma^2 + (\omega - \omega_{\mathrm{int}})^2}\ \tau_{\mathrm{DMM}} \tag{6.2}$$

the pre-multiplier is in form of a damped oscillator, centered at $\omega_{\text{int}} = \frac{K_{\text{sp}}}{(M_o M_m)^{1/2}}$, where $\gamma/2$ is the damping constant. $\gamma^2 = 10^2 5$ is estimated based on the definition that at $\omega_{\text{int}} \pm \gamma/2$, amplitude is reduced to half the value of the peak.

Figure 6.1 presents the measured and modeled G_{b} of varies organic semiconductor and metal interfaces. The crystal structures of these organic semiconductor molecules are also shown in top panel of **Figure 6.1**. G_{b} values predicted by the above mismatch models are presented in the bottom plot. The interfacial spring constant is derived from the effective modulus at the interface obtained in our previous publication. Note that AMM and DMM without bonding modifications are far from satisfactory, while DMM has a closer prediction. This is because the interfacial roughness in the measured structure is around 2 nm, and the coherent phonon length, $L_{\text{coh}} = \hbar v / k_{\text{B}} T$ of CuPc, for example, is around 5 Å. As a result, the phonon scattering at the interface is pure diffuse in nature. The weak interfacial bonding between organic semiconductor and metal will lead to deduction in G_{b} and achieve much closer estimation of G_{b}, see **Figure 6.1**.

However, introducing K_{sp} appears to be an over correction. A comparison between these models and the Molecular Dynamic Simulations (MDS) on CuPc/Ag interface is shown in **Figure 6.2**; AMM+K_{sp} generally agrees with MDS than DMM+K_{sp}; This is due to the fact that in MDS simulation, the interface is perfectly flat, and the formalism confined the transmission as specular. The discrepancy at low interfacial bonding strength regime applies for both models, where the experimental data lies. This overcorrection is attribute to the lack of consideration of the anharmonic phonon transmission.

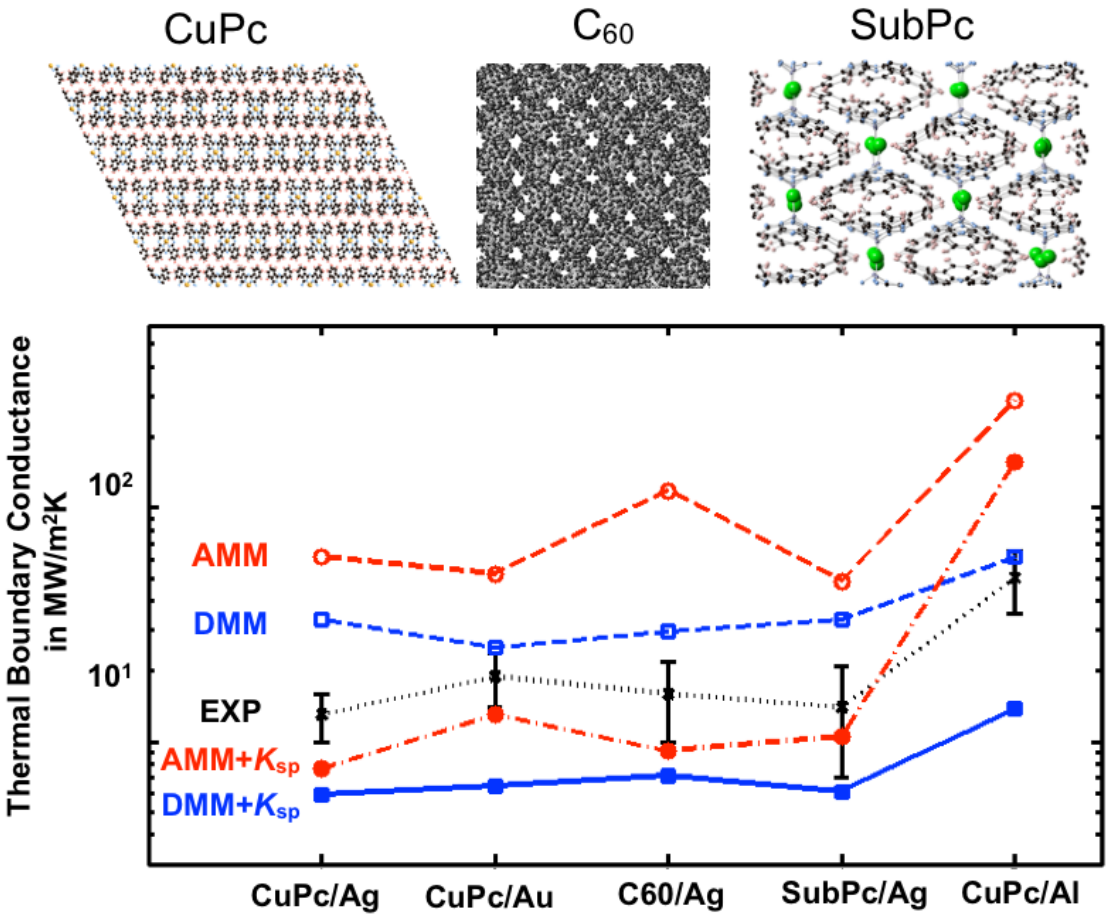

Figure 6.1: (Top) Drawings of the structure of three small-molecule organic semiconductors involved in this work. (Bottom) Thermal boundary conductance (G_{b}) values of the organic semiconductor and metal interfaces measured experimentally, modeled by AMM and DMM; along with the modeled values of modified AMM and DMM considering the interfacial bonding strength, whose effect is represented by the interfacial spring constant K_{sp}.

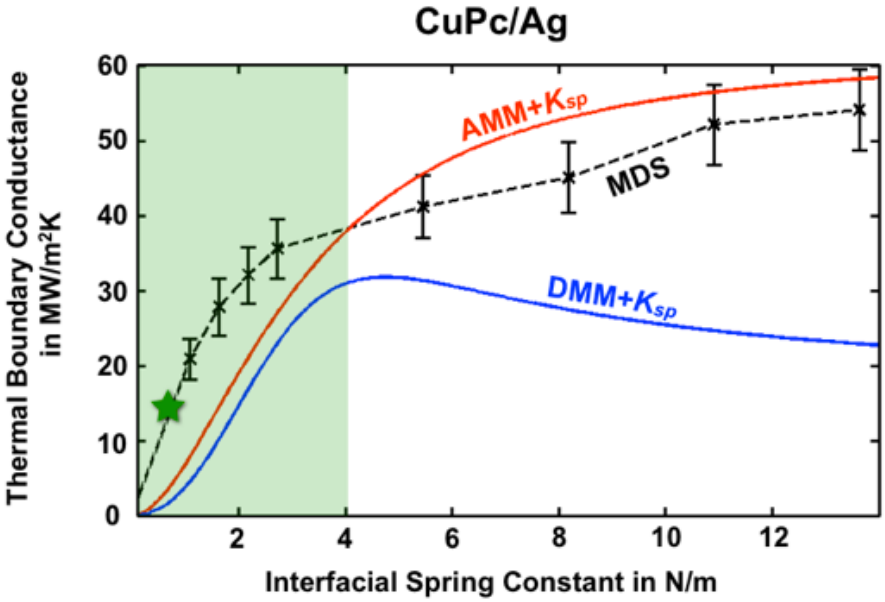

Figure 6.2: Thermal boundary conductance of CuPc/Ag versus interfacial spring constant, calculated by Molecular Dynamics Simulations (MDS), AMM and DMM with bonding modification. The discrepancy between MDS and AMM+K_{sp} and DMM+K_{sp} at lower bonding strength is due to the anharmonic phonon transmissions. The measured TBC (marked with the green star) lies within regime with large anharmonic contribution.

6.3 Anharmonic Contribution to Interfacial Thermal Transport

The anharmonic transmission have been discussed in several works and proved to be important in interfacial thermal transport. However, recall **Eq.** 6.1 and **Eq.** 6.2, both models assume a single harmonic spring constant connecting the two materials. The phonon frequency stay the same before and after the transmission. The anharmonic processes are overlooked. On the other hand, molecular dynamics simulation can provide a more comprehensive description of atomic interaction potential, including the anharmonic contribution. Moreover, MDS work on the material systems studied this work have been proved to be accurate in predicting G_b. Thus, here in this work, the anharmonic contribution is extracted from the simulation collection of molecular dynamics.

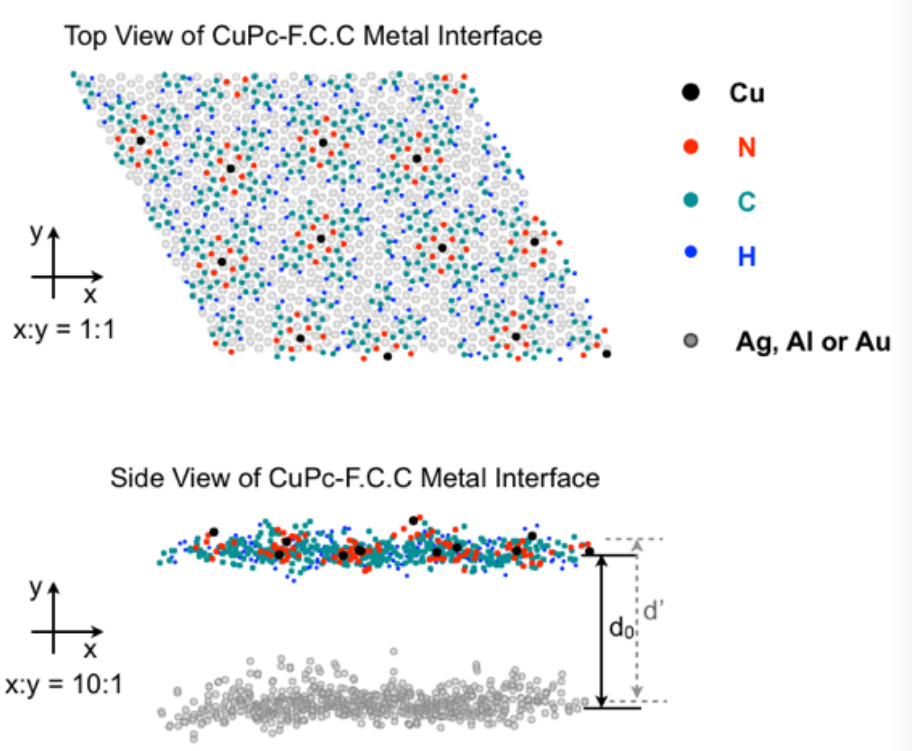

Figure 6.3: Top view (Top) and side view (Bottom) of the CuPc-metal interfaces in molecular dynamics simulation collection.

The CuPc/Metal (Ag, Al, Au) interface simulated by MDS is presented in **Fig** 6.3. The interfacial bonding potential is in form of the Lenard-Jones 9-6 potential (**Eq 5.10**).

Expanding this potential around the equilibrium position r_0, using the Taylor expansion formalism yields,

$$U_{\mathrm{vdW}} = U_0 + \frac{1}{2}K_{\mathrm{sp}}(\Delta r)^2 + \frac{1}{6}\kappa(\Delta r)^3 + \mathcal{O}(\Delta r)^3 \tag{6.3}$$

where

$$K_{\mathrm{sp}} = \left.\frac{d^2U_{\mathrm{vdw}}}{dr^2}\right|_{r=r_{ij}^0} \text{ and } \kappa = \left.\frac{d^3U_{\mathrm{vdw}}}{dr^3}\right|_{r=r_{ij}^0} \tag{6.4}$$

Δr is the displacement to equilibrium position, K_{sp} is the interfacial spring constant, κ is the thermal expansion coefficient of the interface. In **Eq 6.3**, the third term, $\frac{1}{6}\kappa(\Delta r)^3$, is the leading term that stands for the anharmonic phonon transmission - the three phonon processes. A three phonon process involves two phonons on one side of the interface which combine and emit one phonon at the other side of the interface. Previous work shows these inelastic processes provide an extra tunnel for thermal transport thus increase the TBC (*Hopkins et al.* (2011); *Stevens et al.* (2007); *Hopkins* (2009)). In this thesis, the contribution from the anharmonic processes is estimated using the ratio of anharmonic energy U_a to the total energy $U_{\mathrm{tot}} = U_{\mathrm{vdW}} - U_0$, with a re-defined energy zero point at U_0),

$$\frac{U_a}{U_{\mathrm{tot}}} = \frac{\frac{1}{6}\kappa(\Delta r)^3}{\frac{1}{6}\kappa(\Delta r)^3 + \frac{1}{2}K_{\mathrm{sp}}(\Delta r)^2} = \frac{\kappa\Delta r}{\kappa\Delta r + 3K_{\mathrm{sp}}} \tag{6.5}$$

Apply **Eq 6.5** to LJ 9-6 potential, the anharmonic energy ratio, $U_{\mathrm{a}}/U_{\mathrm{tot}}$, can be rewritten as,

$$\frac{U_a}{U_{\mathrm{tot}}} = \frac{972\sum i,j\chi\epsilon_{ij}(r_{ij}^0)^{-3}}{972\sum i,j\chi\epsilon_{ij}(r_{ij}^0)^{-3} + 162\sum i,j\chi\epsilon_{ij}(r_{ij}^0)^{-2}} \sim \frac{6\langle\Delta r\rangle}{6\langle\Delta r\rangle + d_0} \tag{6.6}$$

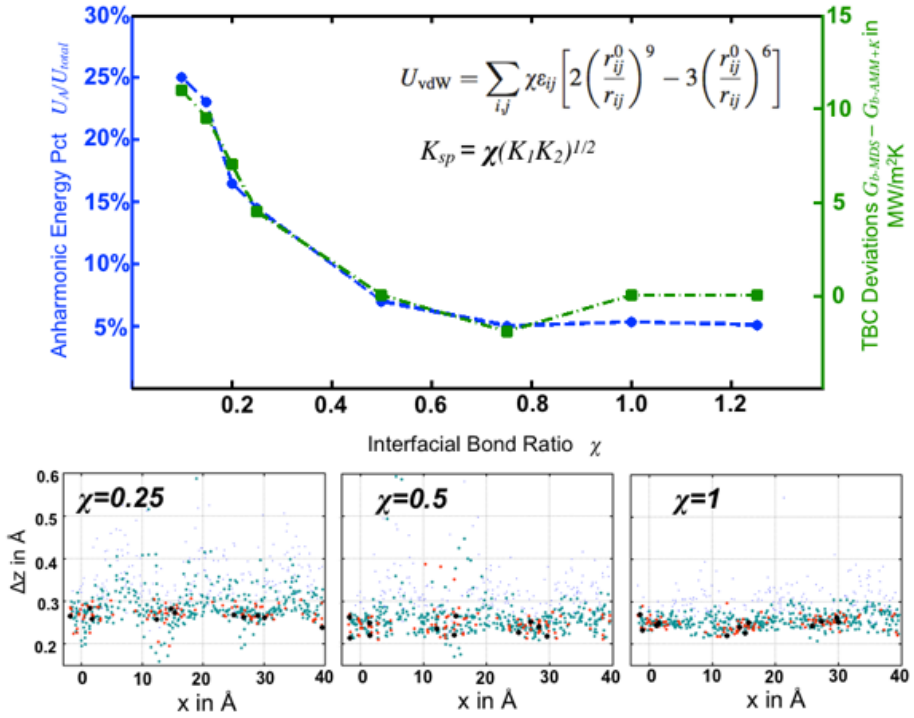

Figure 6.4: Anharmonic contribution percentage (Blue) in interfacial pair potential versus interfacial bond ratio (χ). The AMM+K_{sp} deviation from MDS versus the interfacial bond ratio (Green) scales with the anharmonic energy percentages. The higher the bond ratio, the less the atoms movement perpendicular to the interfaces (Δz), shown in the bottom image series.

Fig 6.4 presents the anharmonic energy percentage (**Eq** 6.6) versus the interfacial bonding ratio, χ. Note that the lower the interfacial bonding, the higher the percentage. This is due the high vibration amplitude, Δz, at low bonding strength, see bottom of **Fig** 6.4, while atoms at the interface move out of the anharmonic zone and anharmonic transmission processes have to be taken into consideration as a result. Previous work shows these anharmonic processes provide an extra tunnel for thermal transport thus increase the TBC (*Hopkins et al.* (2011); *Stevens et al.* (2007); *Hopkins* (2009)). The green curve in **Fig** 6.4 represents the amount that G_b-MDS is larger than G_b- AMM+K_{sp}. The differences scale proportionally with the anharmonic energy percentage, suggesting the anharmonic phonon transmission is a crucial factor that mismatch models have been neglecting.

6.4 Spatially Non-Uniform Phonon Transmission

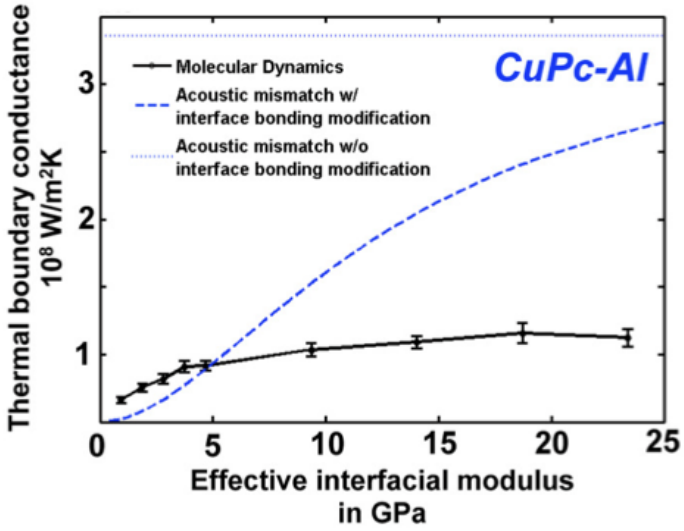

Figure 6.5: Plot of TBC versus effective modulus at the interface of CuPc-Al interfaces. AMM and MDS do not match each other like CuPc-Ag and CuPc-Au. (Figure from Yansha Jin)

However, in the case of CuPc-Al, the fitting between *Prasher* (2009) and MD simulation is not satisfactory. The saturated TBC value G_{b0} does not match with

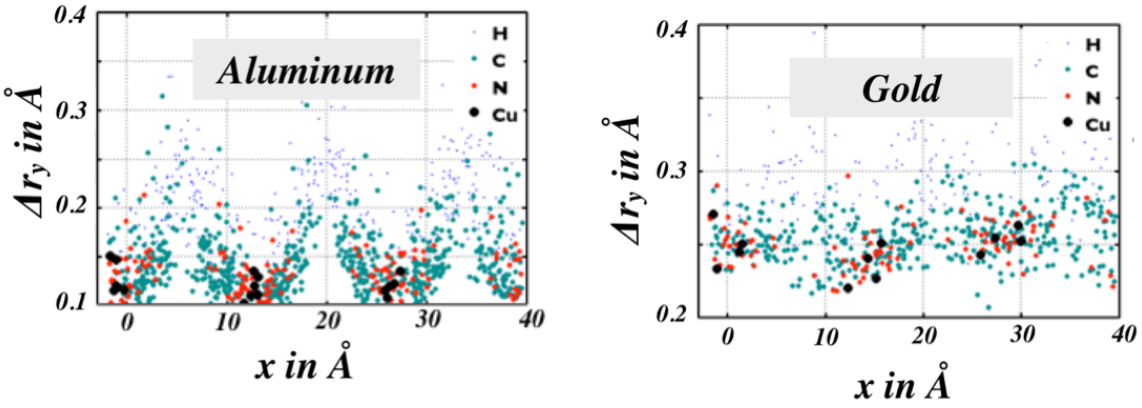

Figure 6.6: Spatial distribution of the average displacements of the 1st layer CuPc (a) at the CuPc-Al interface, (b) at CuPc-Au interface; For CuPc-Al interface, the atoms at the center of the CuPc molecule are more confined than other atoms at the side of the molecule, indicating a spatial non-uniformity. (Figure by Yansha Jin)

each other (See **Figure 6.5**). This could potentially be explained by the break-down of spatially uniform transmission assumption in all existing analytical models. When we compared the average displacement of CuPc-Al in **Figure 6.6 (a)** and CuPc-Au in **Figure 6.6 (b)** under same bond ratio 1.25, it is evident that the spatial distribution of vibration amplitude of atoms are uniform at CuPc-Au interface, while in case of CuPc-Al, though the average amplitude is smaller, the center of the molecule (features near the copper atoms) are more confined than other atoms in the same molecule. Assuming a spatial uniform transmission coefficient at the CuPc-Al interface is not valid according to this analysis. Unlike CuPc/Ag and CuPc/Au, the saturation TBC of CuPc/Al interfaces is only 1/4 of the predicted value of the modified acoustic mismatch model. After extracting the movements of each atom of the 1st layer CuPc near the interface in the MD simulation, we find that when heat is transported across the CuPc/Al interfaces, within the CuPc molecule, the center atom displacements are smaller than C and H atoms at the side which means the bonding strength to the Al atoms is different. This spatial non-uniformity effect is only significant for

CuPc/Al, but not for CuPc/Ag and CuPc/Au and could potentially explain the overestimation of TBC calculated by the mismatch models. After considering the spatial non-uniformity by taking into account the transmission of each atoms, the predicted TBC is more closely matched to the experimental value and the value obtained by MD simulation.

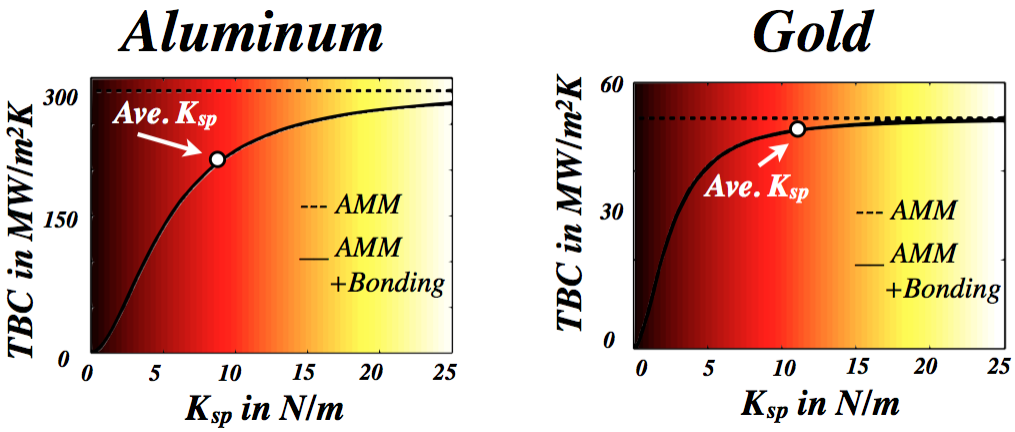

Figure 6.7: TBC has a non-linear dependence on the interfacial bonding strength. The average spring constants for CuPc/Al and CuPc/Ag are mapped in theses plot, respectively. Using this average spring constant lead to inaccurate prediction for TBC of CuPc-Al, since the TBC dependence is not linear and using arithmetic average of spring constant in the models, such as the Modified AMM can be problematic. (Figure by Yansha Jin)

To estimate the contribution of spatial non-uniformity in atomic vibrations to lowering TBC, we averaged individual K_{sp} values in randomly distributed sampling circles 1 nm in diameter (corresponding to the phonon mean free path of CuPc).

Figure 6.7 illustrate the reason why using the average K_{sp} spatially can be problematic. TBC's dependence on K_{sp} is not linear, simply averaging K_{sp} before calculating TBC does not return the accurate average TBC. Thus, we calculated TBC at each position using the sampled K_{sp} within the phonon mean free path of CuPc, then take the average. The illustration of this process is shown in **Figure 6.8**, and the result is shown in **Table 6.1**.

Our model shows better agreement with experimentally measured TBC values, as

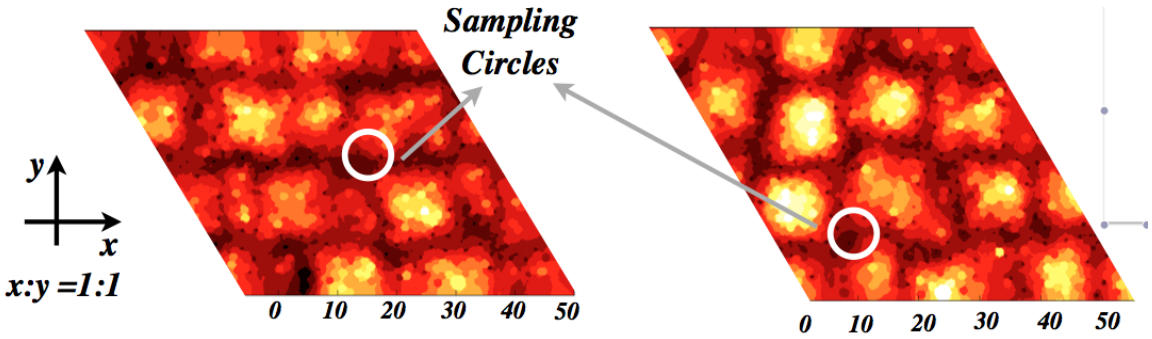

Figure 6.8: Illustration of TBC calculation considering the spatial non-uniform effect. TBC is calculated separately for each atom, then sampled in the circles with radii of CuPc's phonon mean free path. (Figure by Yansha Jin)

	CuPc/Aluminum	CuPc/Gold
MDS (in agreement w/ exp.)	70 ± 5 MW/m^{2}K	46 ± 6 MW/m^{2}K
Modified AMM	201 MW/m^{2}K	52 MW/m^{2}K
Model w/ bonding non-uniformity	94 MW/m^{2}K	44 MW/m^{2}K

Table 6.1: TBC for CuPc/Al and CuPc/Au calculated by MDS; Modified AMM; Analytical model considering bonding and spatial non-uniformity.

well as with MD simulated TBC values than other models, suggesting that phonon transmission is indeed strongly influenced by spatial non-uniformity of bonding and atomic vibrations at the interface.

CHAPTER VII

Summary and Future Directions

7.1 Doctoral Research Summary

My doctoral research work is one of the first reports on the measurements of the thermal boundary conductance values at organic/metal interfaces. (**Ch. III**) I fabricated multilayer films consisting of an archetypal organic semiconductor, CuPc and metals(Al, Ag) by vacuum thermal evaporation. The TBC values for such interfaces are shown to be as low as 13 MW/m^{2}K, (*Jin et al.* (2011)) strongly suggesting the notable interfacial contribution to the thermal transport in nano-structured materials. Quantifying this interfacial contribution is thus extremely essential for the advance of energy conversion applications and the thermal managements for organic electronic device. For example, the TBC values reported by my work are then considered to be a crucial factor in accurate temperature-dependent modeling on the performances of organic light-emitting diodes.(*Qi and Forrest* (2011); *Bergemann et al.* (2012))

As for the thermoelectric applications (**Ch. IV**), the thermally resistive nature of these interfaces can provide us a novel way for tuning the thermoelectric properties of composite materials.(*Jin et al.* (2013)) Our simulations and experiments show that in the CuPc/Ag composite, the percolation threshold for thermal transport $x_{\mathrm{c,th}}\%$ shifts to a higher concentration compared to that for electrical transport$x_{\mathrm{c,e}}\%$ due to the low thermal boundary conductance and the high electrical boundary conductance. A

maximum ratio of electrical conductivity σ_e over thermal conductivity k_{th} is observed near $x_{\text{th,min}}$, the volume fraction that reaches the lowest k_{th}. This maximum ratio is 3 times larger than that of pure CuPc, potentially increasing the thermoelectric figure of merit by more than a factor of 10 times for organic TE materials. This dramatically increased performance potential calls for a composite system with high thermal boundary resistance but low electrical contact resistance, which is more easily achievable, and can allow σ_e/k_{th} to be maximized in the regime where S, Seebeck coefficient is relatively stable.

I have also investigated the fundamental physics of the TBC at the interfaces involving small-molecule organics based on our observation of the low TBC at CuPc/metal interfaces.(**Ch. V**) I found that for highly mismatched interfaces like organics/metal, the TBC was closely correlated to the bonding strength at the interface. Evidence from Molecular Dynamics Simulations (MDS) also showed the significant impact of interfacial bonding on TBC. I also examined the TBC of the organic/organic interfaces and the measured TBC values of these interfaces suggested that regardless of the similar bonding strength between organic/metal and organic/organic systems. The latter exhibited an order of magnitude higher TBC due to the larger overlap in the acoustic phonon spectrum between the organics, indicating that low mismatched systems are not as sensitive to the interfacial bonding strength. The thermal property mismatch and interfacial bonding are now widely accepted as the two dominating factors that are attributed to the TBC, and our work is one of the first experimental demonstrations of the bonding effect.

Aside from the two aspects of thermal boundary transport discussed above, which can be applied to all general interfaces, we found another central influence on our specific small-molecule organics/metal system: spatially non-uniform transmission. (**Chap VI**) The physical models with interfacial bonding modifications can produce results similar to the MD simulations and the experiments. However, in some systems

like CuPc/Al, the predicted TBC deviates from the exact value, suffering a 3-time overestimation. This discrepancy is attributed to the spatially non-uniform phonon transmission verified by extracting the movements of the interfacial atoms in the MD simulations. By adding in this factor to the existing model, the accuracy of the phonon transmission modeling was drastically improved, with the margin of error was reduced to 25%. This work presented a more rigorous way in analyzing the thermal transport at van der Waals interfaces.

In conclusion, organic/metal interfaces are ubiquitous in organic electronics and thermoelectric devices and can have a strong influence on the overall behavior of those devices. Our work can provide some new approaches for optimizing the device performances that have been discussed as well as some fundamental insights into the microscopic mechanisms of phonon coupling across interfaces. The following section presents the outlook regarding follow-on.

7.2 Future Work Proposals

7.2.1 Interfacial Science in Organic Electronic Devices

Electronic devices based on organic semiconductor with metal nanoparticles (NP) incorporated have been demonstrated, such as memory elements, photodetectors (*Guo et al.* (2012)) and transistors (*Tseng and Tao* (2009)). The nanostructure are similar to the nanocomposites for thermoelectric applications discussed in **Chap IV**. Charges trap/de-trap rate in organic FET memory devices is crucial to the speed of the device. Exploring the charge trapping mechanism while tuning the phonon modes at the NPs/organic interfaces is a promising plan, considering the strong coupling between the phonon modes and charge carrier transport.

7.2.2 Thermal Stability of Organic Electronics in Bio-Medical Applications

Considerable amount of research on organic electronics are focus on bio-medical applications due to the mechanical flexibility and bio-compatibility of the organic materials. One of the major problem is the the thermal stability of the organic device (*Kuribara et al.* (2012)). Temperature of sterilization processes can be as high as 121 Celsius, and the thermal stability of organic material under this condition is crucial for the device operations. Thermal property measurements and system analysis of the device can be obtained using the methods in this thesis, (**Chap III** and **Chap I**) that can be valuable in understanding the thermal stability of organic electronic device for bio-medical applications.

7.2.3 Thermal Transport in Carbon Nanoelectronics

Carbon-nanoelectronic devices are becoming increasingly widespread. However, most of its thermal properties are derived from those of graphite, but the heat dissipation in these devices are primarily limited by the edges and the in-plane van der Waals bonds that are not considered as a bulk.(*Baloch et al.* (2010, 2012); *Pop et al.* (2012)) My study on thermal boundary conductance at van de Waals interfaces can bring new understanding in this area and potentially create a novel way in tuning the thermal properties of graphene/CNT devices with interface/surface treatments.

APPENDICES

APPENDIX A

Dimer of Two-Level Molecules

This Appendix is based on the book of *Agranovich and Bassani* (2003).

Let's start with the Hamiltonian for a single molecule. Assume a two-level molecule system: $|g\rangle$ – ground state; $|e\rangle$ – excited state.

$$\hat{H}_{\text{mol}} = \hbar\omega_g |g\rangle\langle g| + \hbar\omega_{ex} |e\rangle\langle e| \tag{A.1}$$

In the solid phase, there are more than one molecule so that the intermolecular interactions have to be considered. The simplest illustration of solid is a dimer system:

$$\hat{H}_{\text{dim}} = \hat{H}_{\text{mol},1} + \hat{H}_{\text{mol},2} + \hat{V}_{1,2} \tag{A.2}$$

$\hat{V}_{1,2}$ is supposed to contain all the Coulomb interactions among excitons and nuclei between molecule 1 and 2 rigorously, but the exciton-exciton interaction is often ignored for simplicity.

The dimer system has four energy states: $|g_1 g_2\rangle$, $|e_1 g_2\rangle$, $|g_1 e_2\rangle$ and $|e_1 e_2\rangle$. $|e_1 g_2\rangle$, $|g_1 e_2\rangle$ are degenerated and have notable interactions in between. All other cross-interactions are negligible compared to the $|e_1 g_2\rangle$, $|g_1 e_2\rangle$ interactions. The Hamilto-

nian can be re-written as:

$$\hat{H}_{\text{dim}} = 2E_g + \begin{array}{c} \\ \langle g_1 g_2| \\ \langle e_1 g_2| \\ \langle g_1 e_2| \\ \langle e_1 e_2| \end{array} \begin{array}{cccc} |g_1 g_2\rangle & |e_1 g_2\rangle & |g_1 e_2\rangle & |e_1 e_2\rangle \\ V_{gg,gg} & 0 & 0 & 0 \\ 0 & E_{ex} + V_{eg,eg} & J_{12} & 0 \\ 0 & J_{12} & E_{ex} + V_{ge,ge} & 0 \\ 0 & 0 & 0 & 2E_{ex} + V_{ee,ee} \end{array} \tag{A.3}$$

where $E_g = \hbar\omega_g$ and $E_{ex} = \hbar\omega_{ex}$. $V_{ab,cd} = \langle ab|\hat{V}_{1,2}|cd\rangle$ and $J_{12} = \langle g_1 e_2|\hat{V}_{1,2}|e_1 g_2\rangle$ is a special quantity representing the intermolecular overlap integral under certain assumptions.

The new eigenstates, $|\pm\rangle$, are the linear combinations of the degenerated states:

$$|\pm\rangle = (|e_1 g_2\rangle \pm |g_1 e_2\rangle)/\sqrt{2} \tag{A.4}$$

with new energy levels

$$E_\pm = \hbar\omega_{ex} + (V_{eg,eg} - V_{gg,gg}) \pm J_{1,2} \tag{A.5}$$

APPENDIX B

Polaron Transport Model

This model follows the work of *Ortmann et al.* (2009).

Though this model does not take lattice disorder into account, it describes the charge transport with both coherent and hopping contribution included. Starting with the polaron Hamiltonian in **Eq 1.18** and adopting the Green-Kubo formalism, the mobility yields,

$$\mu_{\mathrm{GK}} = \frac{1}{2eN_c k_B T} \int_{-\infty}^{\infty} dt \langle \mathbf{j}(t)\mathbf{j}(0)\rangle_H \tag{B.1}$$

And since the current density $\mathbf{j}$ and the polarization $\mathbf{P} = e\sum_M \mathbf{R}_M a_M^\dagger a_M$ relate by $\mathbf{j} = \frac{d\mathbf{P}}{dt}$, $\mathbf{j}$ can be written as,

$$\mathbf{j} = \frac{1}{i\hbar}[\mathbf{P}, H] = \frac{e}{i\hbar}\sum_{MN}(R_M - R_N)J_{MN}a_M^\dagger a_N \tag{B.2}$$

The approach in *Ortmann et al.* (2009) is the polaron transform in form of,

$$\tilde{H} = e^S H e^{S^\dagger}, \text{ where } S = \sum_{\mathbf{MQ}} g_{\mathbf{MM}}^{\mathbf{Q}} a_{\mathbf{M}}^\dagger a_{\mathbf{M}} (b_{\mathbf{Q}}^\dagger - b_{-\mathbf{Q}}) \tag{B.3}$$

Thus,

$$\tilde{H} = \sum_{\mathbf{MN}} a^{\dagger}_{\mathbf{M}} \hat{E}_{\mathbf{MN}} a_{\mathbf{N}} + \sum_{\mathbf{Q}} \hbar\omega_{\mathbf{Q}} \left(b^{\dagger}_{\mathbf{Q}} b_{\mathbf{Q}} + \frac{1}{2} \right) \tag{B.4}$$

where $\hat{E}_{\mathbf{MN}} = e^{C_{\mathbf{M}}} \varepsilon_{\mathbf{MN}} e^{-C_{\mathbf{N}}}$ and $C_{\mathbf{M}} = \sum_{\mathbf{Q}} g^{\mathbf{Q}}_{\mathbf{MM}} (b^{\dagger}_{\mathbf{Q}} - b_{-\mathbf{Q}})$ Use the thermal average of the transfer integral

$$\tilde{\varepsilon}_{\mathbf{MN}} = \varepsilon_{\mathbf{MN}} \exp\left[- \sum_{\mathbf{Q}} \left(\frac{1}{2} + N_{\mathbf{Q}} \right) |g^{\mathbf{Q}}_{\mathbf{MM}} - g^{\mathbf{Q}}_{\mathbf{NN}}|^2 \right] \tag{B.5}$$

The Hamiltonian yields,

$$\tilde{H} = \sum_{\mathbf{MN}} a^{\dagger}_{\mathbf{M}} \tilde{\varepsilon}_{\mathbf{MN}} a_{\mathbf{N}} + \sum_{\mathbf{Q}} \hbar\omega_{\mathbf{Q}} \left(b^{\dagger}_{\mathbf{Q}} b_{\mathbf{Q}} + \frac{1}{2} \right) \tag{B.6}$$

Define the thermal average $\langle\ \rangle_H$ as

$$\langle\ \mathbf{j}(t)\mathbf{j}(0)\ \rangle_H = \frac{\mathrm{Tr}(e^{-(H/k_BT)}\mathbf{j}(t)\mathbf{j}(0))}{\mathrm{Tr}(e^{-(H/k_BT)})} \tag{B.7}$$

with **Eq** B.**2** and **Eq** B.**7**, the mobility (**Eq** B.**1**) splits into two terms,

$$\begin{aligned}
\mu &= \mu_{\mathrm{coh}} + \mu_{\mathrm{inc}} && \text{(B.8)} \\
\mu_{\mathrm{coh}} &= \frac{\sqrt{\pi} e \tau_e}{2 N_c k_B T} \int_{\mathbf{k}} n_{\mathbf{k}} (1 - n_{\mathbf{k}}) (v^*)^2 d\mathbf{k} && \text{(B.9)} \\
\mu_{\mathrm{inc}} &= \frac{e}{2 N_c k_B T \hbar} \sum_{\mathbf{R}} (\mathbf{R}\tilde{J}_{\mathbf{R}})^2 \frac{1}{N_\Omega} && \text{(B.10)} \\
&\times \int_{\mathbf{k_1 k_2}} n_{\mathbf{k_2}} (1 - n_{\mathbf{k_2}}) d\mathbf{k_1 k_2} \int_{\infty}^{\infty} dt e^{(it/\hbar)[\tilde{J}(\mathbf{k_1}) - \tilde{J}(\mathbf{k_2})]} \\
&\times \exp\{2 \sum_{\mathbf{Q}} [N_{\mathbf{Q}} e^{i\omega_{\mathbf{Q}} t} + (1 + N_{\mathbf{Q}})) g_{\mathbf{Q}}] - 1\} e^{-(t/\tau_e)^2}
\end{aligned}$$

APPENDIX C

Anharmonic Phonon Transmission Model

The mode follows *Hopkins* (2009) and adapted by Yansha Jin.

The calculation of phonon transmission at the interfaces is based on the detailed balance relation.

For harmonic phonon transport across the interface. The detail balance is written as

$$\sum_{j} \int_{\omega_{c,1,j}} \hbar\omega v_{1,j} g_{1,j} f_0 \tau_{1,2}(\omega, T) d\omega = \sum_{j} \int_{\omega_{c,2,j}} \hbar\omega v_{2,j} g_{2,j} f_0((1 - \tau_{1,2}(\omega, T)) d\omega \quad \text{(C.1)}$$

where g represents the phonon DOS, which is a function of ω; $f_)$ is the Bose-Einstein distribution, a function of ω and T.

For 3-phonon process, which is illustrated in **Figure** C**.1**, the frequency domain under the cut-off frequency $\omega_{c,2}$ is divided into 3 regimes. Phonons in the blue regime of material 1 can undergo both 2 phonon and 3 phonon processes: creating phonon with the same frequency and double the frequency (green) in material 2; And the green phonon in material 2 can transmitted back to Material 1 by the harmonic process. However, 3-phonon processes for the phonons in the green regime of material 1 creates phonon in the red regime which is not supported by material 1, thus the

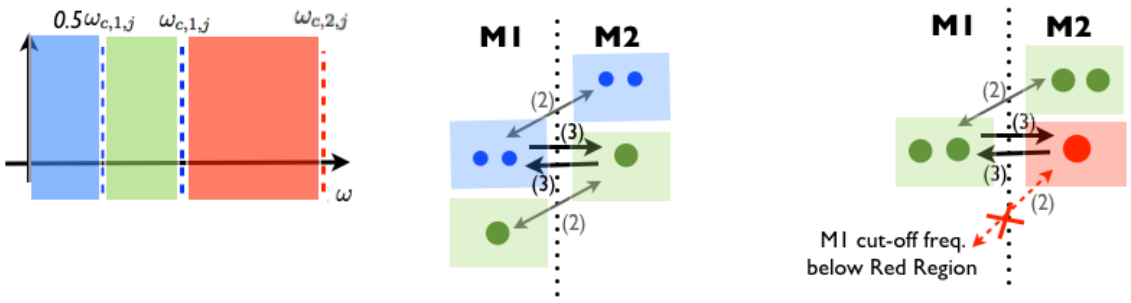

Figure C.1: Schematic drawing of detailed balance of 3-phonon process. (Figure from Yansha Jin)

reverse transmission is forbidden. The detailed balance of the 3-phonon processes is written as,

$$2(\hbar\omega)v_{1,j}g_{1,j}f_0(1-\tau_{12}^{(2)})\tau_{12}^{(3)} = h(2\omega)v_{2.j}g_{2,j}f_0\tau_{12}^{(2)}(1-\tau_{12}^{(3)}) \tag{C.2}$$

when $0 < \omega < \omega_{c,1,j}/2$;

$$2(\hbar\omega)v_{1,j}g_{1,j}f_0(1-\tau_{12}^{(2)})\tau_{12}^{(3)} = h(2\omega)v_{2.j}g_{2,j}f_0(1-\tau_{12}^{(3)}) \tag{C.3}$$

when $\omega_{c,1,j}/2 < \omega < \omega_{c,1,j}$;

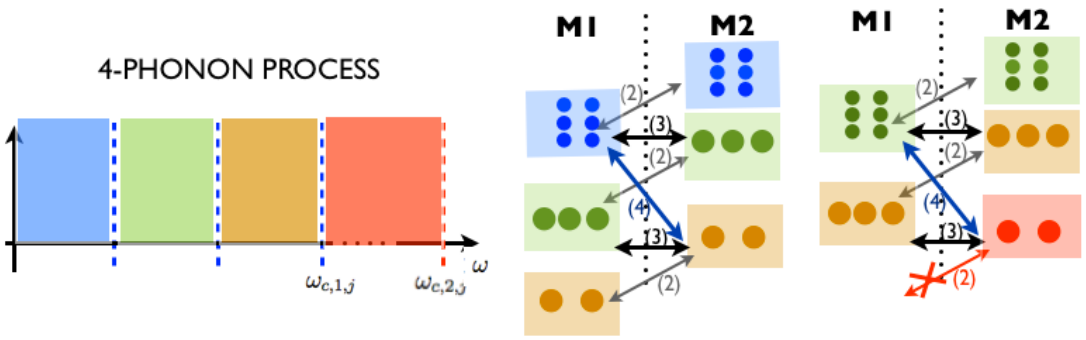

Figure C.2: Schematic drawing of detailed balance of 4-phonon process. (Figure from Yansha Jin)

The schematic drawing of 4-phonon process is shown in **Figure** C**.2**, and the generalized n phonon process is shown in *Hopkins* (2009).

BIBLIOGRAPHY

BIBLIOGRAPHY

Adamovich, V. I., M. S. Weaver, R. C. Kwong, and J. J. Brown (2005), High Temperature Operation and Stability of Phosphorescent OLEDs, *Current Applied Physics*, *5*, 15.

Agranovich, V., and G. Bassani (2003), *Electronic Excitations in Organic Based Nanostructures*, 1st ed., 5-20 pp., Elsevier Academic Press.

Agrawal, K., M. E. Sykes, and M. Shtein (2013), Influence of Exciton Lifetime on Charge Carrier Dynamics in an Organic Heterstructure, *Applied Physics Letters*, *102*, 113,304.

Aïch, R. B., N. Blouin, A. Nouchard, and M. Leclerc (2009), Electrical and Thermoelectric Properties of poly(2,7-carbazole) Derivatives., *Chemical Materials*, *24*, 751.

Antohe, S., N. Tomozeiu, and S. Gogonea (1991), Properties of the Organic-on-Inorganic Semiconductor Barrier Contact Diodes In/PTCDI/p-Si and Ag/CuPc/p-Si, *Physica Status Solidi (a)*, *125*, 397–408.

Ashcroft, N. W., and N. D. Mermin (1976), *Solid State Physics*, 1st ed., 1-212 pp., Harcourt College Publishers.

Baldo, M. (2001), *The Electronic and Optical Properties of Amorphous Organic Semicondutors*, Princeton University (Disseration).

Baloch, K. H., N. Voskanian, and J. Cumings (2010), Controlling the Thermal Contact Resistance of a Carbon Nanotube Heat Spreader, *Applied Physics Letters*, *97*, 063,105.

Baloch, K. H., N. Voskanian, M. Bronsgeest, and J. Cumings (2012), Remote Joule Heating By a Carbon Nanotube, *Nature Nanotechnology*, *7*, 316.

Bassler, H. (1993), Charge Transport in Disordered Organic Photocunductors Simulation Study, *Physica Status Solidi (b)*, *1*, 15.

Bergemann, K. J., R. Krasny, and S. R. Forrest (2012), Thermal Properties of Organic Light-Emitting Diodes, *Organic Electronics*, *12*, 1565.

Borca-Tasciuc, T., A. R. Kumar, and G. Chen (2001), Data Reduction in 3ω Method for Thin-Film Thermal Conductivity Determination, *Review of Scientific Instruments*, *72*, 2139.

Bubnova, O., Z. U. Khan, A. Malti, S. Braun, M. Fahlman, M. Berggren, and X. Crispin (2011), Optimization of the Thermoelectric Figure of Merit in the Conducting Polymer Poly(3,4-ethylenedioxythiophene), *Nature Materials*, *10*, 429.

Cahill, D. G. (1990), Thermal Conductivity Measurement From 30 to 750 K: The 3ω Method, *Review of Scientific Instruments*, *61*, 802.

Cahill, D. G. (2004), Analysis of Heat Flow in Layered Structures for Time-Domain Thermoreflectance, *Review of Scientific Instruments*, *75*, 5119.

Chung, S., J.-H. Lee, J. Jeong, J.-J. Kim, and H. Yongtaek (2009), Substrate Thermal Conductivity Effect on Heat Dissipation and Lifetime Improvement of Organic Light-Emitting Diodes, *Applied Physics Letters*, *94*, 253,302.

Coropceanu, V., J. Cornil, D. da Silva Filho, Y. Oliver, R. Silbey, and J. Bredas (2007), Charge Transport in Organic Semiconductor, *Chemical Review*, *107*, 926.

Costescu, R. M., D. G. Cahill, F. H. Fabreguette, Z. A. Sechrist, and S. M. George (2004), Ultra-Low Thermal Conductivity in W/Al_2O_3 Nanolaminates, *Science*, *303*, 989.

Cutler, M., J. F. Leavy, and R. I. Fltzpartick (1964), Electronic Transport in Semimetallic Cerium Sulfide., *Physical Review*, *133*, 1143.

Daly, B. C., H. J. Maris, W. K. Ford, G. A. Antonelli, L. Wong, and E. Andideh (2002), Optical Pump-Probe Measurements of Sound Velocity and Thermal Conductivity of Hydrogenated Amorphous Carbon Films, *Journal of Applied Physics*, *92*, 6005.

Duong, H. M., D. V. Papavassiliou, K. J. Mullen, and S. Maruyama (2008), Computational Modeling of the Thermal Conductivity of Single-Walled Carbon NanotubePolymer Composites, *Nanotechnology*, *19*, 065,702.

Efremov, A. A., N. I. Bochkareva, R. I. Gorbunov, D. A. Lavrinovich, Y. T. Rebane, T. D. V., and S. Y. G. (2006), Effect of the Houle Heating on the Quantum Efficiency and Choice of Thermal Condition for High-Power Blue InGaN/GaN LEDs, *Physics of Semiconductor Devices*, *40*, 621.

Fox, M. (2001), *Optical Properties of Solids*, 1st ed., 76-222 pp., Oxford University.

Guo, F., B. Yang, Y. Yuan, Z. Xiao, Q. Dong, Y. Bi, and J. Huang (2012), A Nanocomposite Ultraviolet Photodetector Based on Interfacial Trap-Controlled Charge Injection, *Nature Technology*, *7*, 798.

Hopkins, P. E. (2009), Thermoelectricity in Semiconductor Nanostructures, *Journal of Applied Physics*, *106*, 013,528.

Hopkins, P. E., L. M. Phinney, J. R. Serrano, and T. E. Beechem (2010), Effects of Surface Roughness and Oxide Layer on the Thermal Boundary Conductance at Aluminum/Silicon Interfaces, *Physical Review B*, *82*, 085,307.

Hopkins, P. E., J. C. Duda, and P. M. Norris (2011), Anharmonic Phonon Interactions at Interfaces and Contributions to Thermal Boundary Conductance, *Journal of Heat Transfer*, *133*, 062,401.

Hsieh, W.-P., M. D. Losego, P. V. Braun, S. Shenogin, P. Keblinski, and D. G. Cahill (2011), Testing the Minimum Thermal Conductivity Model for Amorphous Polymers using High Pressure, *Physical Review B*, *83*, 174,205.

Hu, L., L. Zhang, M. Hu, J.-S. Wang, B. Li, and P. Keblinski (2010), Phonon Interference at Self-Assembled Monolayer interfaces: Molecular Dynamics Simulations, *Physical Review B*, *81*, 235,427.

Hu, M., P. Kelinski, and P. K. Schelling (2009), Kapitza Conductance of Silicon-Amorphous Polyethylene Interfaces by Molecular Dynamics Simulations, *Physical Review B*, *79*, 104,305.

Huang, B. L., Z. Zi, A. Millward, A. McGaughey, C. Uher, M. Kaviany, and O. Yaghi (2007), Thermal Conductivity of a Metal-Organic Framework (MOF-5): Part II. Measurement, *International Journal of Heat and Mass Transfer*, *50*, 405.

Huang, K. (1997), *Solid State Physics (Chinese)*, 1st ed., 76-283 pp., Beijing University.

Jin, Y., A. Yadav, H. Sun, K. Sun, K. P. Pipe, and M. Shtein (2011), Thermal Boundary Resistance of Copper Phthalocyanine-Metal Interface, *Applied Physics Letters*, *98*, 093,305.

Jin, Y., C. Shao, J. Kieffer, K. P. Pipe, and M. Shtein (2012), Origins of Thermal Boundary Conductance of Interfaces involving Organic Semiconductors, *Journal of Applied Physics*, *112*, 093,503.

Jin, Y., S. Nola, K. P. Pipe, and M. Shtein (2013), Improving Thermoelectric Efficiency in Organic-Metal Nanocomposites via Extra-Low Thermal Boundary Conductance, *Journal of Applied Physics*, *1*, 000,000.

Kahn, A., N. Koch, and W. Gao (2003), Electronic Structure and Electrical Properties of Interfaces between Metals and pi-Conjugated Molecular Films, *Journal of Polymer Science*, *41*, 2529–2548.

Kapitza, P. (1941), Kapitza Resistance, *Journal of Physics, USSR*, *4*.

Kim, D., Y. Kim, K. Choi, J. C. Grunlan, and C. Yu (2010), Improved Thermoelectric Behavior of Nanotube-Filled Polymer Composites with Poly(3,4-ethylenedioxythiophene) Poly(styrenesulfonate), *ACS Nano*, *4*, 513.

Kim, E.-K., S.-I. Kwun, S.-M. Lee, H. Seo, and J.-G. Yoon (2000), Thermal Boundary Resistance at $Ge_2Sb_2Te_5$/ZnS:SiO_2 Interface, *Applied Physics Letters*, *76*, 3864.

Kim, G., K. P. Pipe, and M. Shtein (2011), Thermoelectric and Bulk Mobility Measurements in Pentacene Thin Films, *Applied Physics Letters*, *98*, 093,303.

Kim, N., B. Domercq, S. Yoo, A. Christensen, B. Kippelen, and S. Graham (2005), Thermal Transport Properties of Thin Films of Small Molecule Organic Semiconductors, *Applied Physics Letters*, *87*, 241,908.

Koh, Y. K., S. L. Singer, W. Kim, J. M. O. Zide, H. Lu, D. G. Cahill, A. Majumdar, and A. C. Gossard (2009), Comparison of the 3-ω Method and Time-Domain Thermoreflectance for Measurements of the Cross-Plane Thermal Conductivity of Epitaxial Semiconductors, *Journal of Applied Physics*, *105*, 054,303.

Kröger, I., B. Stadtmüller, F. Reinert, and C. Kumpf (2011), Normal-Incidence X-ray Standing-Wave Study of Copper Phthalocyanine Submonolayers on Cu(111) and Au(111), *Physical Review B*, *83*, 195,414.

Kröger, I., et al. (2010), Submonolayer Growth of Copper-Phthalocyanine on Ag(111), *New J. Phys.*, *12*, 083,038.

Kuribara, K., et al. (2012), Organic Transistors with High Thermal Stability for Medical Applications, *Nature Communications*, *3*, 723.

Kwok, H. L. (2012), Thermoelectric Power and ZT in Conducting Organic Semiconductor, *Journal of Electronic Materials*, *41*, 476.

Leclerc, M., and N. Ahmed (2011), Green Energy From a Blue Polymer, *Nature Materials*, *10*, 409.

Lee, S.-M., and D. G. Cahill (1997), Heat Transport in Thin Dielectric Films, *Journal of Applied Physics*, *81*, 2590.

Li, Q., C. Liu, and S. Fan (2009), Thermal Boundary Resistances of Carbon Nanotubes in Contact with Metals and Polymers, *Nano Letters*, *9*, 3805.

Li, X., and R. Yang (2012), Size-Dependent Phonon Transmission Across Dissimilar Material Interfaces, *Physical Review B*, *24*, 155,302.

Losego, M. D., M. E. Grady, N. R. Sottos, N. R. Cahill, and P. V. Braun (2012), Molecular Dynamics Simulation of Thermal Boundary Conductance between Carbon Nanotubes and SiO_2, *Nature Materials*, *11*, 502.

Majumdar, A. (2004), Thermoelectricity in Semiconductor Nanostructures, *Nature*, *303*, 777.

Majumdar, A., and P. Reddy (2004), Role of electronphonon coupling in thermal conductance of metalnonmetal interfaces, *Appl. Phys. Lett.*, *84*, 4786.

Minnich, A. J., M. S. Dresselhaus, R. Z. F., and C. G. (2009), Bulk nanostructured thermoelectric materials: current research and future prospects, *Energy Environ. Sci.*, *2*, 466.

Ong, Z.-Y., and E. Pop (2010), Molecular Dynamics Simulation of Thermal Boundary Conductance between Carbon Nanotubes and SiO_2, *Physical Review B*, *81*, 155,408.

Ortmann, F., F. Bechstedt, and K. Hannewald (2009), Theory of Charge Transport in Organic Crystals: Beyond Holsteins Small-polaron Model, *Physical Review B*, *79*, 235,206.

Park, J. W., D. C. Shin, and S. H. Park (2011), Large-Area OLED Lightings and their Applications, *Semiconductor Science and Technology*, *26*, 034,002.

Peng, C., L. Cheng, and M. Mansuripur (1997), Experimental and Theoretical Investigations of Laser-induced Crystallization and Amorphization in Phase-Change Optical Recording Media, *Journal of Applied Physics*, *82*, 4183.

Pollack, G. L. (1969), Kapitza Resistance, *Review of Modern Physics*, *41*, 48.

Pop, E., V. Varshney, and A. K. Roy (2012), Thermal Properties of graphene: Fundamentals and applications, *MRS Bulletin*, *37*, 1273.

Prasher, R. (2009), Acoustic Mismatch Model for Thermal Contact Resistance of van der Waals Contacts, *Applied Physics Letters*, *94*, 041,905.

Qi, X., and S. R. Forrest (2011), Thermal Analysis of High Intensity Organic Light-Emitting Diodes Based on a Transmission Matrix Approach, *Journal of Applied Physics*, *110*, 124,516.

Ranninger, J. (2006), Introduction to Polaron Physics: Basic Concepts and Models, *arXiv:cond-mat*, *1*, 0606,665.

Schmidt, A. J., M. Chiesa, X. Chen, and G. Chen (2008), An Optical Pump-Probe Technique for Measuring the Thermal Conductivity of Liquids, *Review of Scientific Instruments*, *79*, 064,902.

See, K. C., J. P. Feser, C. E. Chen, A. Majumdar, J. J. Urban, and R. A. Segalman (2010), Water-Processable Polymer-Nanocrystal Hybrids for Thermoelectrics, *Nano Letters*, *10*, 4664.

Shao, C., X. Ma, C. Zheng, Y. Jin, K. P. Pipe, M. Shtein, and J. Kieffer (2013), Force Field Development and Thermal Conductivity Calculation for Copper Phthalocyanine Molecule, *JPPC*, *1*, 000,000.

Snyder, G. J., and E. S. Toberer (2008), Complex thermoelectric materials, *Nature Materials*, *7*, 105.

Stadler, C., S. Hansen, I. Kröger, C. Kumpf, and E. Umbach (2009), Tuning Intermolecular Interaction in Long-range-ordered Submonolayer Organic Films, *Nature Physics*, *5*, 153.

Stevens, R. J., A. N. Smith, and P. M. Norris (2005), Measurement of Thermal Boundary Conductance of a Series of Metal-Dielectric Interfaces by the Transient Thermoreflectance Technique, *Journal of Heat Transfer*, *127*, 315.

Stevens, R. J., L. V. Zhigilei, and P. M. Norris (2007), Effects of Temperature and Disorder on Thermal Boundary Conductance at Solid-Solid Interfaces: Nonequilibrium Molecular Dynamics Simulations, *International Journal of Heat Transfer*, *50*, 3977.

Stoner, R. J., and H. J. Maris (1993), Kapitza Conductance and Heat Flow Between Solids at Temperatures from 50 to 300K, *Physical Review B*, *48*, 16,373.

Sun, H. (2013), *Acoustic phonon transport at nanostructured interface*, University of Michigan (Disseration).

Sun, H., V. A. Stoica, M. Shtein, R. Clarke, and K. P. Pipe (2013), Coherent Control of GHz Resonant Modes by an Integrated Acoustic Etalon, *Physics Review Letters*, *110*, 086,109.

Swartz, E. T., and R. Pohl (1989), Thermal Boundary Resistance, *Review of Modern Physics*, *61*, 605.

Tong, T., and A. Majumdar (2006), Reexamining the 3-omega Technique for Thin Film Thermal Characterization, *Review of Scientific Instruments*, *77*, 104,902.

Torquato, S., and M. D. Rintoul (1995), Effect of the Interface on the Properties of Composite Media, *Physical Review Letters*, *75*(22), 4067–4070.

Tseng, C.-W., and Y.-T. Tao (2009), Electric Bistability in Pentacene Film-Based Transistor Embedding Gold Nanoparticles, *Journal of the American Chemical Society*, *131*, 12,441.

Venkatasubramanian, R., E. Silvola, T. Colpitts, and B. O'Quinn (2001), Thin-Film Thermoelectric Devices with High Room-Temperature Figures of Merit, *Nature*, *413*, 597.

Veres, J., S. D. Ogier, S. W. Leeming, D. C. Cupertino, and S. Mohialdin Khaffaf (2003), Low-k Insulators as the Choice of Dielectric in Organic Filed-Effect Transistor, *Advanced Functional Materials*, *13*, 199.

Wang, D., L. Tang, M. Lomg, and Z. Shuai (2009), First-principles Investigation of Organic Semiconductors for Thermoelectric Applications, *Journal of Chemical Physics*, *131*, 224,704.

Warta, W., and N. Karl (1985), Hot Holes in Naphthalene: High, Electric-Field-Dependent Mobilities, *Physical Review B*, *32*, 1172.

Yadav, A. (2010), *Thermal Physics in Electronic and Optoelectronic Materials and Devices*, University of Michigan (Disseration).

Young, D. A., and H. J. Maris (1989), Lattice Dynamical Calculation of the Kapitza Resistance between fcc Lattice, *Physical Review B*, *40*, 3685.

Yu, C., K. Choi, L. Yin, and G. J. C. (2011), Light-Weight Flexible Carbon Nanotube Based Organic Composites with Large Thermoelectric Power Factors, *ACS Nano*, *5*, 7885.

Zhang, B., J. Sun, H. E. Katz, F. Fang, and R. L. Opila (2010), Promising Thermoelectric Properties of Commercial PEDOT:PSS Materials and Their Bi_2Te_3 Powder Composites, *ACS Applied Materials and Interfaces*, *11*, 3170.

Zhang, L., P. Keblinski, J.-S. Wang, and B. Li (2011), Interfacial thermal transport in atomic junction, *Physical Review B*, *83*, 064,303.

Zhao, Y., H. A. Kwang, S. Chen, B. O'Connor, K. P. Pipe, and M. Shtein (2007), Localized Current Injection and Submicron Organic Light-Emitting Device on a Pyramidal Atomic Force Microscopy Tip, *Nano Letters*, *7*, 3645.